From 0D to 2D: Synthesis and bio-application of anisotropic magnetic iron oxide nanomaterials

Chang, Fuqiang; Davies, Gemma-Louise

DOI:
10.1016/j.pmatsci.2024.101267

Document Version
Publisher's PDF, also known as Version of record

Citation for published version (Harvard):
Chang, F & Davies, G-L 2024, 'From 0D to 2D: Synthesis and bio-application of anisotropic magnetic iron oxide nanomaterials', *Progress in Materials Science*, vol. 144, 101267. https://doi.org/10.1016/j.pmatsci.2024.101267

Progress in Materials Science 144 (2024) 101267

Contents lists available at ScienceDirect

Progress in Materials Science

journal homepage: www.elsevier.com/locate/pmatsci

From 0D to 2D: Synthesis and bio-application of anisotropic magnetic iron oxide nanomaterials

Fuqiang Chang [a,b], Gemma-Louise Davies [a,b,*]

[a] UCL Department of Chemistry, University College London, 20 Gordon Street, London WC1H 0AJ, UK
[b] School of Chemistry, University of Birmingham, Edgbaston, Birmingham, B15 2TT, UK

A B S T R A C T

Magnetic iron oxide nanoparticles (MIPs) have garnered significant scientific interest due to their magnetic properties and unique features, including low toxicity, colloidal stability, and surface engineering capability. Recent advances in nanoparticle synthesis have enabled the development of MIPs with precise control over their physicochemical properties, making them suitable for medical applications. Anisotropic MIPs have demonstrated shape-dependent performance in various bio-applications, leading to increased research moving from traditional zero-dimensional (0D) morphology towards one-dimensional (1D) and two-dimensional (2D) topology. While these anisotropic materials offer enhanced properties for specific applications, a critical and systematic comparison of their anisotropy effects is lacking in the literature. This review seeks to fill this current gap in the literature and provides a comprehensive summary of the last two decades of research on magnetic iron oxide materials with different shapes in biomedical applications. The paper will discuss the theoretical mechanisms of shape-dependent effects, primary synthetic approaches of 0D, 1D, and 2D MIP materials, biomedical applications, and biological behaviors. In addition, the review identifies critical challenges and open questions that need to be addressed. The proposed research directions outlined in this review have the potential to revitalize the use of "old" MIPs towards future physicochemical and biomedical applications.

Magnetic iron oxide nanoparticles (MIPs), anisotropic, shape-dependent, zero-dimensional (0D), one-dimensional (1D), and two-dimensional (2D), MRI, hyperthermia, bioapplication.

1. Introduction

Anisotropy is a fundamental characteristic of the universe, and it also underlies the existence and functioning of complex systems, ranging from the intricate mechanisms of cell division to the formation of the solar system. At much smaller length scales the rule still holds and the past few years have seen many revolutionary techniques in materials science, especially in the preparation and design of anisotropic particles at the nanoscale which feature shape-dependent physical and chemical properties. Precise regulation of nanoparticle morphology has a profound impact on their characteristics, making it highly desirable for a wide range of physicochemical and biomedical applications. For example, for a range of materials, it has been demonstrated that rod-shaped nanoparticles demonstrate superior cell internalization and improved drug delivery efficiency compared to spherical nanoparticles,[1] while disc-shaped or platelet-shaped nanoparticles exhibit enhanced organ accumulation while experiencing reduced liver sequestration, in contrast to spherical or cylindrical counterparts.[2] Anisotropic nanoparticles display unique behaviors *in vivo* when compared to their isotropic counterparts, and it is increasingly being acknowledged that particle shape and nanoscale structure are key design parameters in the realization of the next generation of nanomedicines.[3,4]

In the past two decades, significant advancements have been made in the development of innovative methods for preparing anisotropic nanoparticles using a wide range of materials, including polymeric materials and inorganic carbon, silica and metal (oxide)

* Corresponding author.
E-mail address: g.davies.7@bham.ac.uk (G.-L. Davies).

https://doi.org/10.1016/j.pmatsci.2024.101267
Received 19 May 2023; Received in revised form 23 February 2024; Accepted 25 February 2024
Available online 29 February 2024

etc. Among these materials, magnetic materials have emerged as a particularly captivating and highly regarded development within the field of nanomaterials research. They have garnered significant attention for their potential applications in the field of bio-applications, such as drug delivery, magnetic separation, biosensing, bioimaging and biocatalysis. Magnetic iron oxide nanoparticles (MIPs) have attracted significant scientific interest due to their size-dependent magnetic properties and a range of other intrinsic characteristics. The size-dependent magnetic behavior of MIPs, coupled with their low toxicity, colloidal stability, and surface engineering capabilities, make them a compelling area of study. These features make them highly promising for a wide array of scientific and technological applications.

Most early magnetic nanoparticle studies focused on spherical particles due to the optimization of the ratio between volume and surface area, as well as their ease of fabrication, relatively low cost, and simplicity. Considerable efforts have been devoted to comprehending the interplay between the size and chemical composition of spherical nanoparticles and their magnetic properties, and hence the biological effects. Conversely, there is a notable lack of research exploring the systematic influence of nanoparticle shape on their magnetic properties, especially when considering nanoparticles with equal volume or closely related size parameters. However, recent research indicates that the geometry of MIPs is, in fact, an critical factor in determining not only their biomedical performance such as in magnetic resonance imaging and hyperthermia, but it also has a significant influence in the *in vivo* behavior in a more complex manner.[1,5] In particular, biomaterial nanosystems have evolved from traditional zero-dimensional (0D) morphology toward one-dimensional (1D) and (two-dimensional) 2D topology very recently due to their unique physicochemical/biological characteristics, which make them cutting-edge tools for a host of biomedical applications.

This review seeks to focus on the synthesis, surface modification, as well as theranostic applications of anisotropic nanoplatforms from 0D to 2D. To highlight the effects of material geometry and material size in each dimension on their bioapplications, herein, classification is based on the geometry of a range of magnetic materials and their sizes in each dimension. Pokropivny and Skorokhod classified nanostructured materials into elementary units based on structure *i.e.*, zero-dimensional (0D), one-dimensional (1D), two-dimensional (2D) and three-dimensional (3D) structures.[6] The definition of 0D MIPs are granular particles where all dimensions are in the nanoscale and their length in three dimensions are comparable, such as spheres, cubes, octopods and snowman shaped anisotropic patchy colloids. 1D MIPs are defined as linear biomaterials with high length-to-diameter ratio, such as nanobelts, nanorods and microfibers. 2D MIPs are planar biomaterials with high diameter-to-thickness ratio, such as nanoprisms, nanoplates and nanosheets. This review describes recent advances in our understanding of the interplay between anisotropy and bioapplications of magnetic materials. Our aim is to summarize the past two decades of studies on magnetic materials with different shapes from 0D to 2D in biomedical applications, including (1) theoretical mechanisms of shape-dependent effects, (2) primary synthetic approaches of 0D, 1D and 2D materials, (3) surface engineering, (4) biomedical applications, and (5) shape induced biological behaviors. Several principles are raised to help design future nanoparticles (NPs). Moreover, some critical challenges and open questions that need to be addressed are proposed.

2. Basic physical properties of magnetic nanoparticles

Iron oxides exist in various polymorphic forms in nature, with magnetite (Fe_3O_4) and maghemite (γ-Fe_2O_3) being the two most

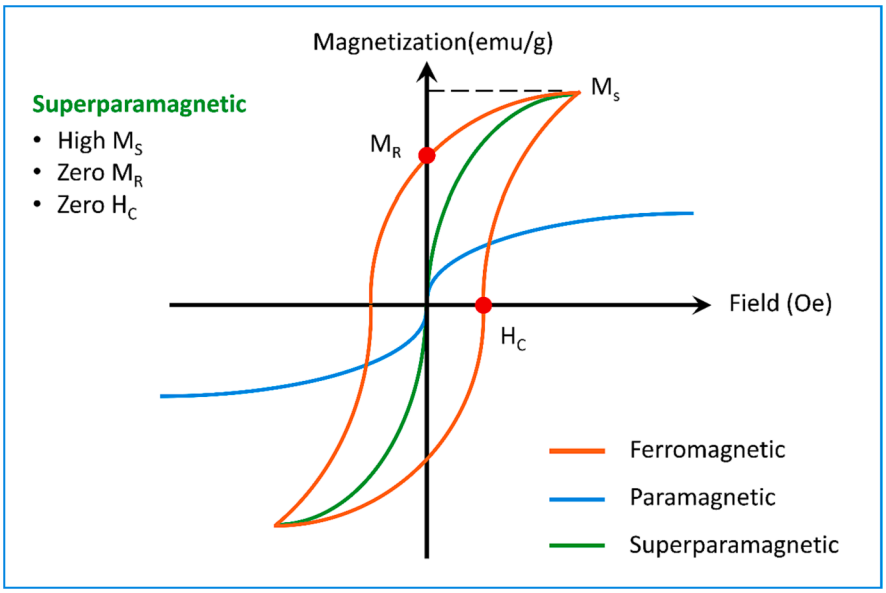

Fig. 1. Hysteresis Loop: Magnetization response to applied magnetic field for ferromagnetic (orange), paramagnetic (blue), and superparamagnetic (green) nanoparticles. The figure includes saturation magnetization (M_S), remanence (M_R), and coercive field (H_c). (For interpretation of the references to color in this figure legend, the reader is referred to the web version of this article.)

extensively investigated materials due to their unique physicochemical properties. The characterization of magnetic materials often involves studying their response to an applied magnetic field (H), which can be depicted using magnetic hysteresis loops (M−H curves). Fig. 1 illustrates examples of these curves, including the superparamagnetic (SPM) curve (in green), paramagnetic (in blue) and the ferromagnetic (FM) hysteresis loop (in orange). These curves represent the relationship between the magnetization value (in emu/g) and the applied magnetic field (in Oe). When subjected to an external magnetic field, a magnetic material undergoes magnetization and eventually reaches a maximum value known as the "saturation magnetization" (M_S), which represents the highest achievable magnetization for that material.[7] In addition to M_S, the FM hysteresis curve also exhibits the values of coercivity (H_C) and remnant magnetization (M_R). Coercivity indicates the difficulty of demagnetizing the material, while remnant magnetization represents the amount of magnetization retained in the absence of an applied magnetic field.[7].

The behavior of a collection of magnetic nanoparticles, whether superparamagnetic or ferro/ferrimagnetic, depends on the temperature at which the measurement is conducted.[8] This distinction arises due to the energy barrier associated with the rotation of dipole moments within the crystal, which must be significantly lower than thermal energy for superparamagnetism to occur. Thus, the transition temperature from ferro/ferrimagnetic behavior to superparamagnetic behavior is a critical parameter for magnetic nanoparticles.[9].

Macroscopic Fe_3O_4 and γ-Fe_2O_3 particles can be divided into magnetic domains that orient themselves in such a manner as to reduce the total magnetostatic energy. The competition between the magnetostatic energy and the domain wall energy limits the break-up of the system into single domain particles. For MIPs with diameters in the range of $10\ \text{nm} < d < 60\ \text{nm}$, the magnetization of a single magnetic domain (SD) can assume two distinct "easy" crystallographic directions, which are separated by an anisotropic energy barrier.[10–12] However, when the particle size is small, thermal effects become prominent. Above a critical temperature known as the blocking temperature (T_B), the magnetization direction of the particles becomes thermally disordered. Below T_B, the particles exhibit a phenomenon called "superparamagnetism," where they display single-domain behavior. In this state, the system's retentivity and coercivity decrease to zero, indicating that the magnetization within the particles can randomly change direction under the influence of temperature. The Néel relaxation time represents the average time interval between two magnetization flips in the absence of an applied magnetic field. When the measurement time for nanoparticle magnetization is significantly longer than the Néel relaxation time, no observable magnetization is detected. However, in the presence of a magnetic field, there is a statistical alignment of the magnetic moments, leading to a significantly higher magnetic susceptibility compared to paramagnetic nanoparticles. This unique property, marked by the lack of remanent magnetization in single domain nanoparticles after the removal of the external field, enables their colloidal stability and avoid magnetically triggered agglomeration, which is critical for biomedical applications.

Notably, the units for magnetic properties described in this review (and in the wider literature) are often used interchangeably, and can be converted between CGS unit and SI unit as follows:

$$\text{Unit of magnetic field strength } (H),\ 1\ Oe \rightarrow {}^{10^3}\!/_{4\pi}\ A\Big/m$$

$$\text{Unit of magnetic moment (m)},\ 1\ emu \rightarrow 10^{-3}\ Am^2$$

$$\text{Unit of Mass magnetization } (\sigma),\ \ 1\ emu\big/g \rightarrow 1\ Am^2\big/Kg$$

Where A is Amp, m is metre, g is gram.

3. Fundamentals of shape-dependent properties and mechanisms

The morphology of magnetic nanoparticles plays a significant role in influencing various interconnected physical, chemical, and physiological factors, ultimately impacting their performance in biomedical and biological applications. To accurately predict the properties of these nanoparticles and explore their potential applications, it is essential to develop a systematic understanding of the mechanisms underlying shape-dependent effects.

The properties of magnetic materials are typically governed by their electronic and crystal structures. Anisotropy, in contrast to isotropy which implies uniform properties in all directions, means directional dependent properties. Therefore, the introduction of anisotropy to nanoparticles can lead to interesting properties, owing to an interplay between magnetocrystalline anisotropy, shape anisotropy, and crystal surface facets.[13] Ferromagnetism arises from the intricate interplay of electronic spin–spin, spin–orbit, and coherent exchange interactions among free electrons, leading to the alignment of their magnetic moments along specific directions within the structure of a material. However, when the size of a magnetic material is reduced to the nanometer scale, where electron interactions are confined, its ferromagnetic behavior becomes dependent on its dimensions. Consequently, the magnetic properties, including coercivity and magnetization values, can be intentionally modified by controlling the size, shape, and surface characteristics of the material.[14–16] For example, spherical polycrystalline materials consist of many single crystals that possess easy axes in all directions, allowing for homogeneous magnetization. In contrast, non-spherical polycrystalline materials and elongated particles such as 1D nanorods, nanotubes, and nanowires exhibit a preference for magnetization along their long axis. Similarly, 2D plate-like particles demonstrate a tendency to magnetize perpendicular to their basal plane. Consequently, these non-spherical and elongated particles exhibit an anisotropic response to magnetic fields, which is distinct from the isotropic behavior observed in spherical polycrystalline materials.[15,17,18] In addition, superparamagnetism is governed by the interplay of magnetic anisotropy, which aligns the magnetization vector, and thermal fluctuations, which introduce temporal variations.[19] The blocking temperature is

determined by the anisotropy constant (energy barrier) of the material as well as the volume of the particles.[20,21] For instance, spherical particles have a blocking temperature (T_B) of 142 K, whereas cubic nanocrystals exhibit a significantly higher T_B of 190 K.[22]

The non-spherical shape of a ferromagnetic nanoparticle gives rise to an additional contribution to the anisotropy energy. This energy is associated with the interaction between the alignment of magnetic moments in preferred directions and the axes determined by the particle's shape.[23] For example, it has been found that spherical iron oxide nanoparticles consist of multiple facets, which result in increased surface spin disorder and lower M_s values. On the other hand, octahedral, cubic, wire, and rod-shaped nanoparticles have fewer facets, reduced spin disorder, and consequently exhibit higher M_s values.[24] Specifically, compared to spherical nanoparticles (8 % disordered surface spins), cubic nanoparticles with a lower percentage of disordered surface spins (4 %) have a smaller surface anisotropy, leading to a higher M_s.[14,16] To improve the performance of MIPs for biomedical applications, it is imperative to exert precise control over their magnetic properties, particularly the M_s and effective magnetic anisotropy (K_{eff}).[25]

The morphology of magnetic iron oxide NPs plays a crucial role in magnetic resonance imaging (MRI), and it influences their contrast ability in two key ways. Firstly, from a geometric perspective, the morphology of the nanoparticles determines their surface-area to volume ratio and the effective radius. These factors are important in determining the interactions of nanoparticles with their surrounding environment, particularly in terms of their ability to interact with water protons. Secondly, the morphology of nanoparticles induces local field inhomogeneity of the magnetic core and gradient of the stray field when an external magnetic field is applied, leading to significant effects on the magnetic relaxation, dephasing, and diffusion processes of nearby water protons, ultimately influencing the transverse relaxation rate and ultimately affecting the contrast signals detected in MRI.[26] MIPs with a high degree of shape anisotropy exhibit a strong and spatially non-uniform stray field, significantly impacting water proton diffusion and dephasing. Besides, anisotropic nanoparticles with a large hydrodynamic radius are favourable to prolong rotational correlation time (τ_R).[27,28] Therefore, it is crucial to take into account the morphology when designing more effective and efficient nanoparticle-based MRI contrast agents for sensitive and accurate diagnosis or therapy in clinical applications.

The anisotropic shape of nanoparticles is a key factor in enhancing hyperthermia for cancer therapy. This is exemplified by the case of Fe_3O_4 nanocubes, which exhibit a higher magnetic anisotropy density compared to their nanosphere counterparts. As a result, the nanocubes generate increased magnetic hysteresis loss and improved heat production when exposed to an alternating magnetic field.[21,29,30] Hence, this improvement leads to a remarkable enhancement in hyperthermia performance for cancer therapy, as supported by experimental observations conducted by Cheon *et al.*[14] Similarly, in hyperthermia, both octahedral and elongated shaped MIP have received great attention due to their larger specific absorption rate (SAR) values compared to other shapes given by their high aspect ratio together with the increasing area of the hysteresis loops which lead to a large magneto-mechanical torque.[31,32] Chain like structures or nanowires (NWs) exhibit higher efficiency in magnetic hyperthermia application, owing to the fact 1D magnetic NWs possess larger frictional reactive areas than 0D NPs.[33–35]

In the realm of magnetic hyperthermia, the desired elevation of temperature is achieved through the interaction of magnetic nanoparticles with a high-frequency external alternating magnetic field. An alternative recent focus has been directed towards exploring the interplay between magnetic nanoparticles and a low-frequency external alternating magnetic field. This interaction exploits the oscillating movement of nanoparticles in response to an applied alternating field to generate and control mechanical movements or deformations.[36] This phenomenon, referred to as 'magneto-mechanical actuation' (MMA), exhibits significant potential across various engineering applications.[37] It induces (composite) material responses, encompassing alterations in shape, expansion, contraction, or rotation, making it applicable in essential devices such as actuators and sensors requiring controlled mechanical movements.[38,39] Additionally, magneto-mechanical strategies have been showcased not only in conjunction with classical molecular pathway modulation using molecular medicine and/or targeted therapy,[40,41] but have also presented novel therapeutic avenues in the domain of cancer treatment.[42] The mechanism underlying MMA in cancer treatment involves exposing magnetic particles to a uniform magnetic field B. Under such conditions, the average magnetic moment M of the particles experiences a magnetic torque $M \times B$, aligning with the field direction when the particle's magnetic anisotropy reaches a sufficient level. In fluidic solutions, the magneto-mechanical effect reorients particles through the utilization of spatially uniform, rotating, or variable magnetic fields. For effective torque, highly anisotropic particles, such as magnetic disks[43] or (assembled)[44] nanorods[45] with substantial magnetic shape anisotropy, are often preferred.

Morphology also plays an important role in photothermal therapy due to their different optical performances. For example, optical absorbance maxima for dispersions of gold nanorods and gold nanospheres in tetrahydrofuran occurred at 521 and 799 nm, respectively.[46] To maximize the efficiency of photothermal conversion, it is essential to carefully assess the wavelength of the incident light.[47] 2D materials, for example MnO_2 nanosheets also showed high near-infrared absorption and photothermal conversion efficiency enabling 2D nanosheets to be significantly utilized in photothermal therapy (PTT).[48] However, there is still a lack of comprehensive research on the photothermal effect of MIPs with controlled shapes, and the current research available are inconclusive, indicating a need for further investigation.

Particle morphology significantly influences a variety of biological and biophysical processes, encompassing biodistribution, cellular internalization, circulation, trafficking, and cytotoxicity.[49,50] When we look at the natural world, a diverse array of shapes abound and endure: bacteria are often found in spherical (coccus), rod-like (bacillus, tobacco mosaic virus), crescent (vibrio), and twisted (spirilla) forms.[51] Bacterial morphology is known as a means to directly and significantly gain evolutionary advantages through specific mechanisms, including their interaction with surfaces, passive diffusion, and active motility.[52,53] Hence, the shape of MIPs will play a pivotal role as a critical design parameter in intelligently controlling their interactions with various target tissues, including the liver, kidney, lung, and spleen. This aspect is likely to be crucial for the development of future biomedical applications involving these systems.[54]

Changes in the geometry of NPs can have a significant impact on the pharmacokinetics and biodistribution of the agents, consequently altering their toxicological profile.[55] For example, when particles are in contact with the surface of a cell, the radius of curvature plays a critical role in determining the amount and rate of phagocytosis of particles.[3,56] Hence anisotropic nanoparticles with high aspect ratio, are more likely to be taken up by cells due to the increased contact area with the cell surface. Moreover, the increased surface area of anisotropic nanoparticles offers greater potential for targeting ligands to interact with cell surface receptors, leading to enhanced cellular targeting through increased valency.[57] Additionally, the extent of particle uptake and the specific *in vitro* model utilized heavily influence *in vitro* toxicity, with these effects being highly dependent on the shape of the particles. Nanoparticles with high aspect ratios have demonstrated the capability to induce pro-inflammatory or cytotoxic effects.[58]

Anisotropic nanoparticles also exhibit distinct *in vivo* behaviour, for example, their non-spherical shape allows them to align with the blood flow, resulting in prolonged circulation time. As a consequence, these nanoparticles show improved targeting of tumours *in vivo* compared to their spherical counterpart.[59] Cylindrical micelles and rods have the advantage of maintaining extended blood-circulation times even up to one week after injection while minimizing interactions with macrophages.[60,61] Additionally, 1D and 2D possess ultrahigh surface-to-volume ratios, making them versatile nanoplatforms capable of loading substantial amounts of functional molecules, biomolecules, and drugs. This property enables their application in the construction of bioprobes or drug delivery systems, offering enhanced efficiency.[62–65]

4. Synthesis

The synthesis of precisely shaped nanostructures is crucial because different preparation methods have significant effects on the

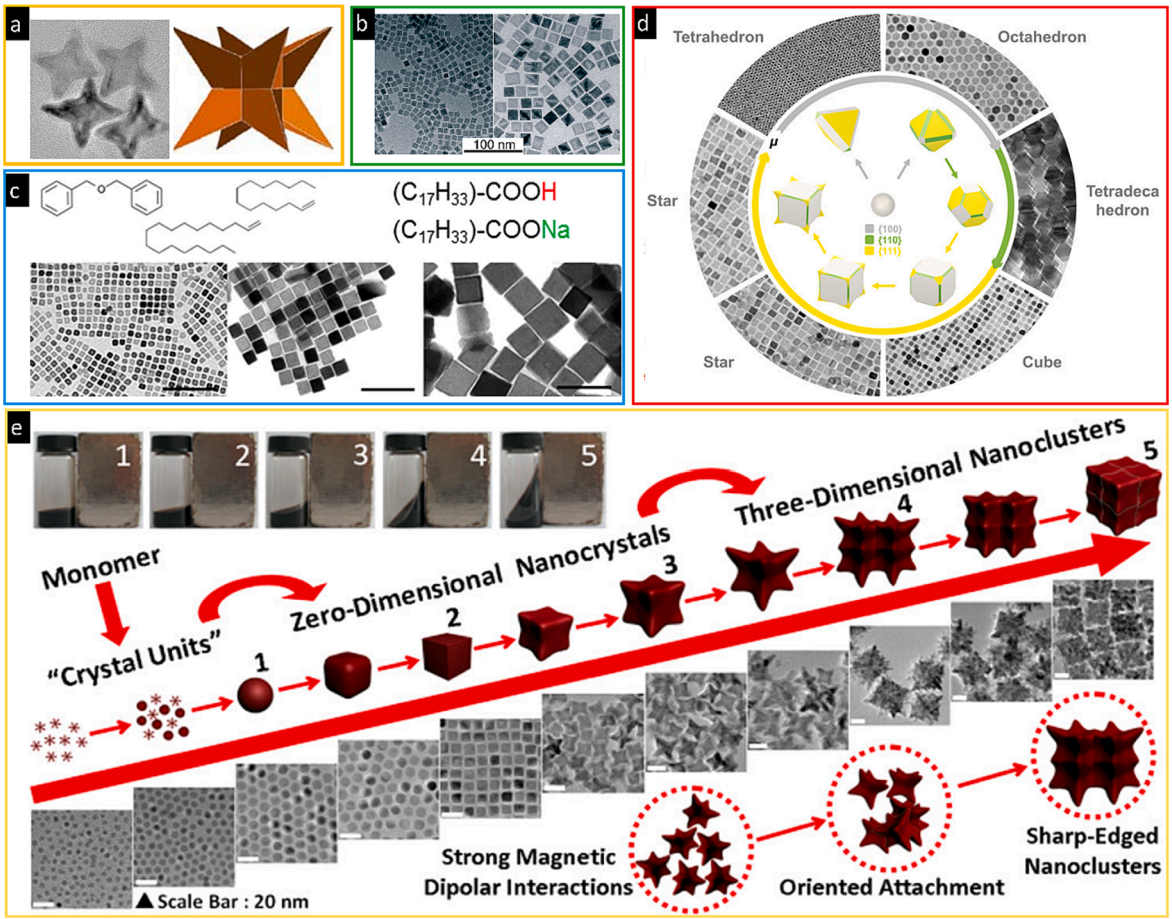

Fig. 2. (a) TEM image of octapod-shaped iron oxide consisted of uniform four-armed star-like particles synthesized using $FeCl_3$ as iron precursor and its corresponding geometric model, adapted with permission from ref.[94], copyright 2013 Nature Publishing Group; (b) TEM images of monodisperse cubic iron oxide prepared using sodium oleate as stabilizer, adapted with permission from ref.[95], copyright 2007 American Chemical Society; (c, d) synthesis of uniform Fe_3O_4 nanocrystals by optimizing the solvents and surfactants, adapted with permission from ref. [100,101], copyright 2019, 2017 American Chemical Society (All the scale bars in panel c correspond to 100 nm); (e) controlled synthesis of nanocrystals by tunning the reaction temperature and heating rate, adapted with permission from ref.[102], copyright 2013 American Chemical Society.

morphology of the anisotropic particles, and hence their shape-dependent properties. Magnetic nanoparticles with various dimensional structures can be produced under various reaction conditions *via* two main routes, *i.e.,* 'top-down' and 'bottom-up'. Top-down approaches involve the fragmentation of larger materials into nanoparticles using ball milling,[66] exfoliation,[67] and electrospinning.[68,69] In contrast, bottom-up approaches start from small molecules and rely on chemical reactions, including co-precipitation,[70,71] thermal decomposition, sol–gel method, microemulsion method, hydrothermal synthesis, and microwave-assisted synthesis.[72–74]

Each method has its own advantages in preparing various dimensional particles, so the choice of the synthetic route depends on the desired functionalities of the nanoparticles. For example, thermal decomposition stands out as an efficient approach for synthesizing high-quality, uniform, and crystalline 0D MIPs.[75] In contrast, magnetic field-induced assembly of iron oxide nanoparticles shows great potential for preparing 1D materials.[76] Additionally, hydrothermal methods have demonstrated promise in producing MIPs with 2D geometry.[77] While various synthesis methods have been developed for the production of MIPs, here our primary focus is on the synthesis routes of uniform MIPs with 0D, 1D and 2D structures, with a selective emphasis on the most pertinent methods.

4.1. Primary synthetic methods of 0D MIPs

4.1.1. Thermal decomposition synthesis

The thermal decomposition process is commonly regarded as a typical approach for the production of highly crystalline monodisperse nanocrystals (NC) with nanometer sizes compared to other methods. This approach involves the conversion of different types of organometallic compounds in organic solvents with high boiling points, which are supplemented with stabilizing surfactants.[78–80] By carefully manipulating reaction parameters, including precursor composition, ligands, solvent, reaction temperature, and duration, a wide range of MIPs with varying sizes and morphologies can be achieved.[81] Different iron precursors, such as iron pentacarbonyl ($Fe(CO)_5$),[82], $Fe(acac)_3$, $FeCl_3$,[83] iron oleate[84], iron acetylacetonate,[85], and FeO(OH) are frequently employed in the synthesis of MIPs. Stabilizing agents like oleylamine (OAm),[86] oleic acid (OA)[87] and 1-octadecene[88] are commonly added to the reaction to control the nucleation and growth rates of iron oxide nanocrystals, thus facilitating the formation of 0D MIPs. Irrespective of the precursors, during the thermal decomposition reaction iron oleate (FeOA) is produced as intermediate, and subsequently undergoes decomposition forming iron oxide nanoparticles. However, due to the limited and overlapping temperature window between the formation of iron oleate, and the subsequent generation of intermediates (pyrolysis products), even minor alterations may lead to significant changes in size, size distribution, and morphology.[89,90]

Both iron precursor sources ($FeCl_3$, $Fe(acac)_3$, FeO(OH), and $Fe(CO)_5$)) and oleate source (oleate acid, oleylamine, sodium oleate, oleyl alcohol) have a drastic impact on the formation and purification of iron oleate, and hence the nucleation and growth of iron oxide nanoparticles.[79,83,91–93] For example, Krishnan *et al.* prepared iron oxide (Fe_3O_4) nanoparticles with size control between approximately 2 nm and 30 nm using three different precursors. They found that all three procedures share iron(III) oleate as reaction intermediate and the ratio of Fe to OA is of utmost importance for the nucleation and growth of iron oxide NC.[79] By taking Fe(II)CO_3 and Fe(III)CO_3 as iron resources, Weller *et al.* demonstrated that there are numerous FeOA complexes of different compositions identified in the intermediate oleate composition ($(Fe^{III})_m(Fe^{II})_n(O^{-II})_x(OA^-)_y$).[84] By varying the reaction conditions, a diverse array of monodisperse iron oxide nanoparticles with defined sizes and shapes was achieved. Interestingly, star-shaped nanocrystals were obtained during the nucleation stage, which subsequently underwent a metamorphic process, ultimately transforming into cubic-shaped particles. Notably, the utilization of $FeCl_3$ as an iron precursor led to the development of octopod-shaped MIPs by virtue of the residual chloride ions, which play a crucial role in inducing this unique particle morphology (Fig. 2a).[94]

On the other hand, stabilizers and solvent composition have been demonstrated to play an important role in regulating the shape of particles. For example, when sodium oleate is used as stabilizer, cubic nanoparticles with narrow size distribution, shape edges and flat facets can be achieved (Fig. 2b).[95,96] By changing the stabilizer composite, uniform shape- and size-controlled monodisperse particles can be achieved.[97] By altering the ratio of oleic acid, 1,2-hexadecanediol, and oleylamine, iron oxide nanoparticles with various shapes such as cubes, octopods, spheres, octahedrons, triangles/hexagons, and rods/beams were controllably prepared.[98,99] Varying solvent is another approach to tune the particle properties. For example, by incorporating 1-tetradecene as an additional solvent alongside 1-octadecene and dibenzyl ether in a solvent mixture, Muro-Cruces *et al.* prepared high quality nanocubes with sharp edges across a wide size range of 9–80 nm (Fig. 2c).[100] The use of mixed solvents contributed to the establishment of stable conditions, enabling the preservation of the cubic shape across a wide range of sizes.

By carefully controlling the solvent environment, Swihart *et al.* achieved the synthesis of uniform magnetic Fe_3O_4 nanocrystals with sizes ranging from 4 to 55 nm, exhibiting exceptional monodispersity in both shape and size (Fig. 2d).[101] They proposed that the choice of solvent, specifically benzyl ether, can influence the behavior of the iron precursor and consequently impact the morphology of the magnetic nanocrystals. To overcome this challenge, they replaced benzyl ether with a more stable solvent mixture comprising benzaldehyde and benzyl benzoate, leading to the development of a series of effective and reproducible high-temperature decomposition formulas. Additionally, they demonstrated that the polarity of the solvent controlled the particle size, while the presence of short ligands shifted the morphology of the nanocrystals from octahedral to cubic. By employing this strategy, they successfully prepared uniform MIPs in various shapes, including tetrahedra, octahedra, tetradecahedra, cubes, and stars.

The physical parameters of reaction conditions, for example temperature or heating rate, play a significant role in directing the particle geometry. Gu *et al.* demonstrated that the formation of Mn and Zn-doped iron oxide nanocrystals depended on the reaction temperature and aging time (Fig. 2e). The crystal nucleation and growth process were evaluated using the variation of monomer concentration in the classical La Mer model.[102] At temperatures below 260 °C, no product was observed, while irregular "crystal nuclei" with sizes of 2–3 nm were formed at 260 °C. Increasing the temperature to 300 °C resulted in the formation of numerous

uniform nanocrystals after 20–40 min.

Similarly, Singh *et al.* showed that the size of MIPs can be tuned by the heating rate.[103] At low heating rates (*e.g.*, 5 °C/min), MIPs with cubic morphology and sizes ranging from 13 nm to 58 nm were prepared, with the size increasing as the reaction progressed. On the other hand, at a rapid heating rate (*e.g.*, 10 °C/min), the formation process exhibited a different behavior. Initially, small octahedral nanoparticles formed after 2 min of reaction, which then transformed into truncated octahedra after an additional 4 min. The truncated octahedra further evolved into a mixture of truncated octahedra and cuboctahedra shapes, eventually resulting in cubic morphology with a size of 30 nm after 20 min of reaction time. Furthermore, Begin-Colin *et al.* demonstrated the adjustability of Wüstite-Spinel core–shell cubic-shaped nanocrystals by simply changing the heating rate from 1 °C/min to 5 °C/min. This adjustment resulted in the size of the nanocrystals changing from 16 nm to 13 nm.[104]

4.1.2. Seeded growth for the production of asymmetric pseudo-0D MIPs

The seeded growth (also known as seed-mediated growth) method is a distinctive approach in the synthesis of inorganic nanoparticles that involves a heterogeneous nucleation process.[105] Unlike general wet chemical synthesis methods, where nucleation and growth occur simultaneously, the seeded growth method separates these steps. Pre-formed nanoparticles, known as seeds, are introduced into a solution with a subcritical concentration, preventing new nucleation events.[106] By utilizing preformed nanoparticles as seeds, seeded growth methods enable precise control over the shape, aspect ratio, and properties of nanocrystals through the growth of additional domains in subsequent reactions.[107–110] Moreover, seed-mediated growth is not only a powerful and versatile means to grow nanoparticles in a programmable manner, but also represents a convenient and reliable approach towards the preparation of anisotropic hybrid nanocrystals.[111] These hybrid nanocrystals integrate two or more different types of nanocrystals into a single particle, enabling unique applications in biomedical imaging.[112–114]. Notably, nanoparticles produced using this approach are not always referred to as 0D in the literature, since they are not truly 0D according to the purest definition, however their structure can be considered pseudo-0D, due to their properties aligning with the 0D nature of the individual components.

Using amorphous Fe@Fe_3O_4 nanoparticles as seeds and silver oleate (AgOA) as the noble metal precursor, Hou *et al.* successfully synthesized monodisperse Janus- and satellite-like plasmonic-magnetic Ag-Fe@Fe_3O_4 heterostructures (Fig. 3a).[115] The heterogeneous nucleation process initiated with the attachment of AgOA molecules to the oleylamine-coated Fe@Fe_3O_4 NPs *via* van der Waals forces in a low-polar solvent. Subsequent nucleation and growth of Ag resulted in the formation of Janus-like Ag-Fe@Fe_3O_4 heterostructures.

Building upon a similar concept, Yin *et al.* have proposed a versatile seed-mediated approach for synthesizing asymmetric 0D nanoparticles of M−Fe_3O_4 (M = Au, Ag and Pd) 0D asymmetric nanoparticles directly in both aqueous and non-aqueous media (Fig. 3b).[116,117] This approach utilizes the reductive properties of Fe_3O_4 to initiate the reduction of metal cations and the deposition of a metal seed onto the Fe_3O_4 nanoparticle surface, followed by controlled growth of the metal seed through a seed-mediated process. The size ratio between the Fe_3O_4 seed lobe and the metal nanoparticle can be adjusted, resulting in tuneable heterodimers. These heterodimers exhibit excellent water dispersibility, biocompatibility, and serve as dual-mode contrast agents for MRI and computed tomography (CT) imaging. Furthermore, seeded growth offers an inherent advantage in the engineering of metal nanoparticles, as they can undergo a second step involving seeded growth or galvanic replacement. This enables the production of more complex heterodimer structures, such as $AgPt_{alloy}$–Fe_3O_4, $Au_{core}@Pd_{shell}$–Fe_3O_4, and Au_{shell}–Fe_3O_4, which exhibit multifunctional imaging capabilities including optical coherence tomography (OCT) and photoacoustic (PA) behavior.

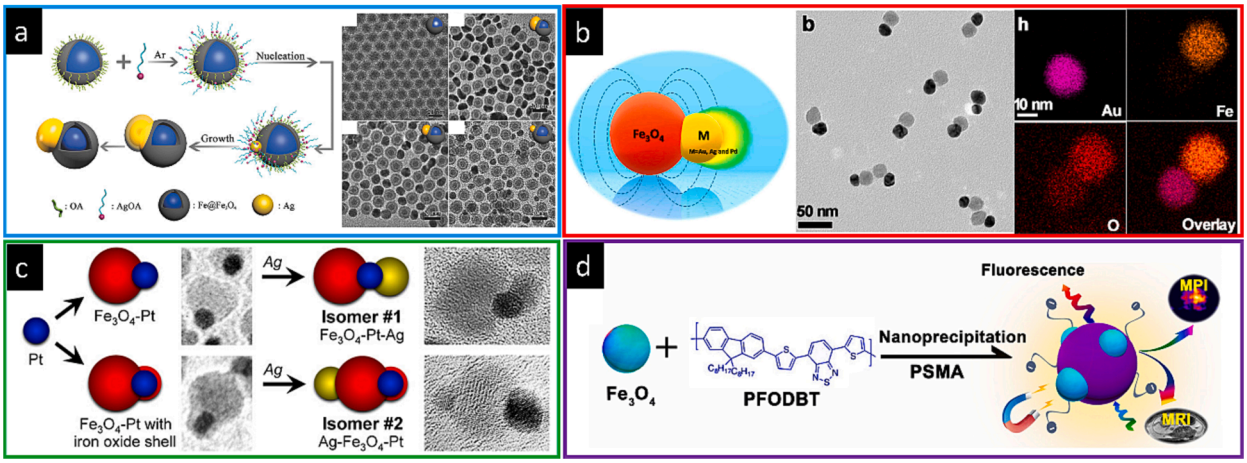

Fig. 3. (a) Schematic illustration of the nucleation and growth mechanism of the Ag–Fe@Fe_3O_4 heterostructures (left panel), and TEM images of Fe@Fe_3O_4 particles and Ag–Fe@Fe_3O_4 with different size ratio (right panel). All the scale bars correspond to 20 nm. adapted with permission from ref.[115], copyright 2018 Wiley Online Library; (b) synthesis of M−Fe_3O_4 (M = Au, Ag and Pd) heterodimers, and (c) Ag–Pt–Fe_3O_4 heterotrimer isomer (Pt seeds are 4 nm in diameter); (d) synthesis of Janus iron oxides-semiconducting polymer nanoparticle. (b-d) adapted with permission from ref.[116,108,118], copyright 2019, 2014 and 2018 American Chemical Society.

Taking the concept a step further, Schaak *et al.* employed multistep seeded-growth reaction sequences to synthesize Ag–Pt–Fe_3O_4 and Au–Pt–Fe_3O_4 heterotrimer hybrid nanomaterials.[107] Firstly, Ag or Au nanoparticles were synthesized and used as seeds to prepare Pt–Fe_3O_4 heterodimers. In the second step, Pt–Fe_3O_4 heterodimers served as seeds to induce the growth of a silver domain on the opposite patch of Pt, resulting in the formation of Ag–Pt–Fe_3O_4 sandwich structures (Fig. 3c). Similarly, this strategy was adapted for the synthesis of iron oxide-poly(styrene-co-maleic anhydride) Janus nanoparticles (Fig. 3d) [118].

4.2. Primary synthetic methods of 1D MIPs

4.2.1. Thermal decomposition

Despite the inherent cubic spinel structure of γ-Fe_2O_3 or Fe_3O_4, the thermal decomposition approach poses challenges in the preparation of one-dimensional anisotropic nanocrystals. However, there have been reports on the successful synthesis of 1D MIPs.[119,120] The structure of the precursor complex is a critical parameter in the synthesis of materials with diverse dimensions. For instance, Turner *et al.* successfully generated thin whisker-shaped iron oxide nanoparticles by selectively decomposing an iron oleate complex.[121] Through their investigation of the iron oleate complex, they discovered that it exhibits a quasi-octahedral core structure with a FeO_6 configuration, characterized by a non-equivalent arrangement of three ligands: two symmetric bonds and one asymmetric bond. They proposed that the interaction involving the third ligand plays a crucial role in guiding the formation of the one-dimensional nanostructure. This nanostructure consists of an inorganic backbone formed by the Fe-O portion of the complex, surrounded by the oleate ligands.

Ying *et al.* utilized a similar approach to prepare magnetic nanorods with adjustable aspect ratios.[122] Through the thermal decomposition of iron oleate in benzyl ether with sodium oleate, they fabricated single-crystalline γ-Fe_2O_3 1D nanorods. By controlling the reaction temperature, they successfully tuned the size of the nanorods, ranging from 2 nm width and 30 nm length at 200 °C to 10 × 50 nm at 290 °C. In a recent study, Sahu *et al.* successfully synthesized monodisperse one-dimensional magnetite nanorods by incorporating sodium oleate during the pyrolysis of the iron oleate precursor. Importantly, the presence of ethanol and water during the preparation of iron oleate resulted in a modified complex structure, thereby impacting the nucleation and growth conditions during the subsequent thermal decomposition.[123]

4.2.2. Soft templating

The soft template method is also applied in the synthesis of MIPs nanostructures of dimensions above 0D. Soft templates include small molecules,[124] polymers[125,126] *etc*. that can act as structure-directing agents in the formation of MIPs. Compared to the hard template method, soft template approach often lacks control over size and uniformity.[127]

In the presence of poly(ethylene glycol) (PEG) as a soft template, Zhen *et al.* successfully prepared 1D Fe_3O_4 nanowires through a simple hydrothermal route (Fig. 4a).[128] PEG, with its long-chain structure and selective absorption on preferred facets, served as a crucial component for constructing the desired nanostructures. The concentration of PEG in the PEG/H_2O solution system played a vital role in controlling the morphology of Fe_3O_4 nanostructures. Notably, in the absence of PEG-400, only 0D Fe_3O_4 nanoparticles were obtained, while increasing PEG concentration favoured the formation of 1D Fe_3O_4 nanowires. The maximum yield of Fe_3O_4 nanowires was achieved at a volume ratio of 1:3 between PEG and H_2O. Moreover, the diameter and length of the 1D Fe_3O_4 nanowires increased proportionally with higher PEG molecular weight.

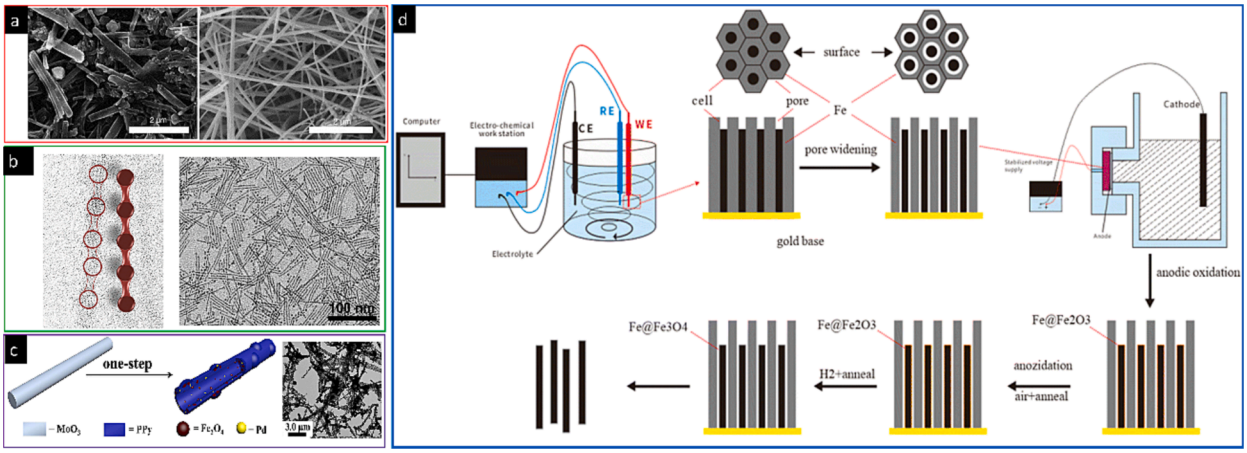

Fig. 4. (a) SEM images of Fe_3O_4 nanorods and nanowires synthesized with the assistance of (a) polyethylene glycol (PEG)-1000 and (b) PEG-20,000 (all the scale bars correspond to 2 μm), adapted with permission from ref.[128], copyright 2006 Elsevier; (b) Synthesis of iron oxide nanorods using volatile compounds as soft templates, adapted with permission from ref.[129], copyright 2015 American Chemical Society; (c) synthesis of hollow mesoporous magnetic nanotubes using MoO_3 nanorods as hard template, adapted with permission from ref.[131], copyright 2019 Wiley Online Library; (d) Flowchart for preparation of core–shell Fe@Fe_3O_4 nanowires on an anodic aluminium oxide (AAO) template, adapted with permission from ref.[134], Springer Nature.

In the study conducted by Weller *et al.*, iron oxide nanorods were prepared *via* a one-step thermal decomposition approach using a combination of oleic acid and oleyl alcohol as a soft template, along with the presence of volatile compounds such as water and ethanol.[129] The absence of these volatile compounds resulted in the absence of nanorod formation, highlighting their crucial role in the synthesis process. The resulting nanorods feature an average length of 24 nm and a diameter of 2.5 nm (Fig. 4b).

4.2.3. Hard templating

In hard template synthesis, specific-shaped templates are initially fabricated and then coated with desired materials. The core materials are subsequently removed to create hollow structures. Surface modification is often utilized to enhance coating efficiency by modifying surface functionality such as charge and polarity. The coated template is then selectively removed through methods like chemical etching, thermal treatment, calcination, or solvent dissolution. Hard templates provide precise control over size and dispersity of the final nanomaterials, but their synthesis can be time-consuming and costly.[130]

Generally, the hard template needs a separate treatment for its removal, however, in a novel and simplified approach developed by Wu *et al.*, Pd-decorated magnetic hollow 1D nanotubes was synthesized while the template was simultaneously eliminated in a single step (Fig. 4c).[131] By utilizing MoO_3 nanorods as initial hard templates, the addition of pyrrole monomer, $FeCl_3{\cdot}6H_2O$, $PdCl_2$ and $NH_3{\cdot}H_2O$ initiated the oxidative polymerization of pyrrole, leading to the formation of a polypyrrole shell that covered the surface of the MoO_3 nanorods. Simultaneously, Fe^{3+} was reduced to Fe^{2+} by pyrrole, and through a well-known coprecipitation method using $NH_3{\cdot}H_2O$, the Fe^{2+} and Fe^{3+} ions rapidly transformed into Fe_3O_4 nanoparticles. Notably, the MoO_3 template gradually dissolved into soluble MoO_4^{2-} ions upon exposure to $NH_3{\cdot}H_2O$.

Instead of the template-coating hard template approach described above, another widely adapted method to prepare 1D MIPs involves employing a template-filling strategy.[132] Anodic aluminum oxide (AAO) and polycarbonate membranes serve as common hard templates for the synthesis of 1D nanomaterials. For instance, to generate a magnetic 1D hybrid, a combination of a magnetic precursor and organic materials is introduced into the pores of the template, followed by subsequent processing steps. Prina-Mello *et al.* produced hybrid MIP-silica NWs through vacuum assisted infiltration of magnetite NPs and a tetraethoxysilane mixture into an AAO template. Sonication treatment released the NWs which possessed 8 μm length and 176 nm diameter.[133] Wu *et al.* successfully fabricated Fe nanowires on a 30 nm diameter AAO template through direct current deposition. Subsequently, the Fe NWs underwent electrochemical anodization and annealing in air to produce highly uniform Fe@ Fe_3O_4 core–shell nanowires with dimensions of 5.2 μm length and a diameter of 30 nm (Fig. 4d).[134]

4.2.4. Self-assembly or field-induced assembly

In this synthetic approach, 1D arrays are prepared through the controllable conjugation of pre-synthesized magnetic nanoparticles.[135] The assembly of nanoparticles can proceed simultaneously in a one-pot manner, where the nanoparticles are formed and *in situ* assembled. Alternatively, the conjugation can be driven by the magnetic dipole–dipole interaction between adjacent nanoparticles,

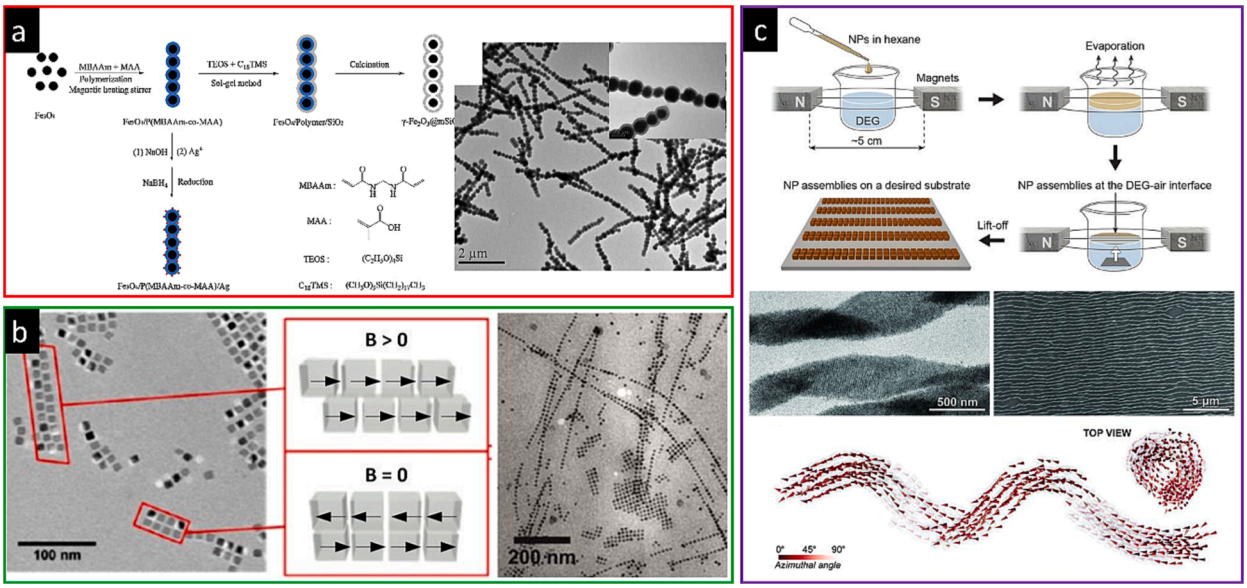

Fig. 5. (a) Synthesis procedure and TEM image of 1D magnetic Fe_3O_4/P(N,N'-methylenebisacrylamide-co-methacrylic acid) nanochains, adapted with permission from ref.[139], copyright 2015 Elsevier.; (b) cryo-TEM image of 1D and 2D structures of cubic nanoparticles, and a sketch of the corresponding dipole orientations, adapted with permission from ref.[142], copy right 2015 National Academy of Sciences; (c) schematic representation of the experimental setup for the self-assembly of magnetite nanocubes into helical superstructures (upper panel), and electron microscope images and snapshots from Monte Carlo simulations of single-stranded helices (bottom panel), adapted with permission from ref.[143], copyright 2014, American Association for the Advancement of Science.

and the assembly process can be facilitated by an external magnetic field.[136,137] The magnetic field can be precisely programmed in terms of strength and spatial distribution, making it a powerful tool for the fine control of particle assembly.[138] Once the targeted 1D structure formed, additional coating could be employed to prevent the particle disassembly.

A classic example illustrating this is the work of Yang *et al.*, who prepared 1D magnetic Fe_3O_4/P(*N,N′*-methylenebisacrylamide-*co*-methacrylic acid) nanochains by polymerization coating in the presence of Fe_3O_4 NPs under magnetic stirring (Fig. 5a).[139] The magnetic stirrer not only prevented particle sedimentation but also played a crucial role in inducing the assembly of Fe_3O_4 nanoparticles into 1D nanochains. These nanochains exhibit a 1D core–shell chain-like structure, with sizes ranging from 2 to 4 μm and a thin polymer shell that can be adjusted in terms of thickness.

Assembly of MIPs into a 1D structure is not restricted to the single-phase medium, as it can also take place at the oil–water interface. For example, Xu *et al.* demonstrated an efficient method for preparing one-dimensional magnetic Fe@Fe_2O_3 nanochains at the interface of water and cyclohexane.[140] By reducing Fe^{3+} to zero-valent Fe in the presence of $NaBH_4$, Fe nuclei grew into nanoparticles that assembled into nanochains through magnetic dipole–dipole interaction and anisotropic magnetic forces. Interestingly, the surface oxidation of Fe nanoparticles occurred *in situ* during synthesis and post-treatment, resulting in stable Fe@Fe_2O_3 core–shell nanochains without the need for inert gas protection. Alternatively, Davies *et al.* employed an aqueous/dichloromethane biphasic system to fabricate 1D 'nano-necklace' arrays composed of 0D MIPs.[141] The process involved several key steps. Firstly, the MIPs dispersed in the upper aqueous phase were aligned into flexible 1D arrays under external magnetic field. Subsequently, the assembled structure was transferred into the organic phase, which contained reactive metalloorganic precursors. The presence of water absorbed on the surface of the MIPs subsequently triggered the hydrolysis of metallorganic precursors forming an oxide layer. The newly coated layer not only prevented the disassembly of 1D but also improved their stability in water.

When the nano magnetic units for assembly are anisotropic, more complex structures can be achieved under field-induced assembly. For instance, Förster *et al.* discovered that cubic iron oxide nanoparticles with a size of 8.2 nm assembled into highly regular 1D, 2D, and even 3D structures, including chains, ribbons, sheets, and large cuboids, when subjected to an external magnetic field (Fig. 5b).[142] The applied magnetic field aligned the dipole moments of the nanoparticles, resulting in attractive interactions that drove the particles to come into close contact. Short-range van der Waals interactions then arranged the nanoparticles in a face-to-face attachment configuration, which remained stable even after the magnetic field was turned off. Notably, this study highlighted the crucial role of particle geometry, as cubic nanoparticles formed ordered assemblies while spheres did not exhibit the same behavior.

Furthermore, through optimization of the interplay between shape anisotropy and magnetocrystalline anisotropy, Plajn *et al.* successfully assembled helical nanowires using cubic magnetite nanocrystals (Fig. 5c).[143] By placing a hexane solution of monodisperse magnetite nanocubes at the diethylene glycol-air interface and allowing solvent evaporation in the presence of a magnetic field, they achieved the spontaneous formation of single-, double-, and triple-stranded helix superstructures. The surface concentration of particles and the complete evaporation of the solvent in the magnetic field were crucial factors in the formation of well-defined nanoparticle assemblies.

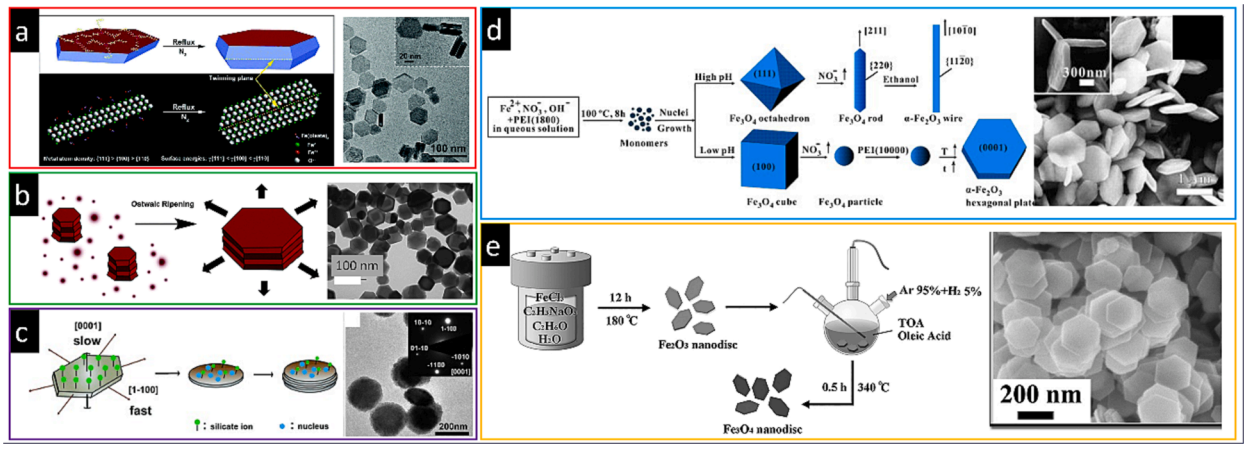

Fig. 6. (a) Schematic illustration for the synthesis of iron oxide twin nanoplates and representative TEM images of the product, adapted with permission from ref.[146], copyright 2018 Royal Society of Chemistry. (b) Hexagonal magnetic nanoprisms formed by stacking of hexagonal-shaped nuclei on {1 1 1}-type facets, adapted with permission from ref.[147], copyright 2015, Royal Society of Chemistry. (c) α-Fe_2O_3 nanodiscs with a layered structure assembled from nanoplates with silicate anions as capping ligands, adapted with permission from ref.[150], copyright 2019, Wiley-VCH. (d) Controllable synthesis of Fe_3O_4 and α-Fe_2O_3 nanocrystals via hydrothermal process, adapted with permission from ref.[152], copyright 2012, Elsevier. (e) Synthesis of iron oxide nanodisc based on an alcohol-thermal reaction, adapted with permission from ref.[154], copyright 2014, Wiley-VCH.

4.3. Primary synthetic methods of 2D MIPS

4.3.1. Thermal decomposition

Once again, thermal decomposition has emerged as a powerful technique not only for the production of uniform 0D and 1D MIPs but also for the synthesis of 2D MIPs. In a study conducted by Gu *et al.*, the synthesis of single-crystalline superparamagnetic γ-Fe_2O_3 ultrathin 2D nanoplates with a remarkable thickness of 1.4 nm was achieved through thermal decomposition of an iron oleate complex with 1-octadecene and sodium oleate.[144] The formation of nanoplates is attributed to the unique structural characteristics of bidentate bonding between Fe and a carboxyl group, which originate from the preparation of an iron oleate complex in pure methanol. Additionally, by adjusting the reaction conditions, such as temperature, the lateral sizes and thickness of the nanoplates can be controlled and varied.

Iron oxide nanoplates with a thickness of around 3 nm were synthesized by Bao *et al.* utilizing the thermal decomposition method.[145] The careful control over reaction temperature and the introduction of trioctylphosphine oxide (TOPO), a ligand with lower affinity to iron ions, exerted significant influence on the nucleation and growth processes of the iron oxide plates. These controlled variables played a crucial role in governing the formation of highly defined and homogeneous iron oxide nanoplates, enhancing their overall quality. Building upon this approach, Gao *et al.* utilized the 3 nm thick iron oxide nanoplates as seeds to prepare iron oxide twin nanoplates. Through this approach, they achieved the formation of uniform twin nanoplates with an edge length of 25.0 nm and a thickness of 13.0 nm (Fig. 6a).[146]

In the work by Bossmann *et al.*, hexagonal Fe_3O_4 nanoplatelets were synthesized by incorporating stearic acid as a second ligand pair along with oleic acid as stabilizers (Fig. 6b).[147] The formation of these nanoplatelets was attributed to the asymmetric growth rate between the {1 1 1} and {1 1 0} crystallographic faces. Through the process of Ostwald Ripening, hexagonal-shaped nuclei twinned on {1 1 1}-type facets, resulting in the formation of well-defined hexagonal nanoplatelets. These nanoplatelets exhibited an edge length of 45 nm and thickness of 5 nm. The use of stearic acid as a ligand pair and the selective growth on specific crystallographic facets allowed for the controlled synthesis of hexagonal Fe_3O_4 nanoplatelets with desired dimensions and morphology.

4.3.2. Hydrothermal

Hydrothermal synthesis is a technique used to synthesize MIPs by subjecting the reaction mixture to high temperature and pressure conditions in an autoclave, typically above 100 °C and at vapor pressures exceeding 1 atm. This method offers several advantages, including a straightforward experimental procedure, the production of high-purity products, cost-effectiveness, and excellent water dispersibility of the resulting materials.[148] $FeCl_2$, $FeCl_3$, $FeSO_4$ and $Fe(NO_3)_3$ are often used as iron precursors for hydrothermal synthesis of MIP.[135,149] In addition to selecting the appropriate iron precursors, the incorporation of a directing agent is often necessary to facilitate the formation of 2D MIP structures using the hydrothermal approach.

Through hydrothermal synthesis, Song *et al.* utilized iron chloride as the iron precursor to prepare α-Fe_2O_3 nanodiscs with a layered assembled structure.[150] The incorporation of a silicate anion played a crucial role in the formation of 2D crystallites by selectively adsorbing onto the {0 0 1} plane of α-Fe_2O_3 nanoplates, resulting in the generation of nanoplate-like building units (Fig. 6c). The presence of silicate anions not only influenced the growth of iron oxide, promoting platelike morphology through ion-doping effects, but also facilitated the self-assembly of the nanoplates into a layered structure. The α-Fe_2O_3 nanodiscs with layered structures theoretically could be converted to Fe_3O_4 *via* a reduction reaction.

In another study conducted by Zhang *et al.,* Fe_3O_4 triangular nanoprisms (TNPs) with a 2D structure were prepared through a 1,3-propanediamine (PDA) assisted hydrothermal synthesis method with $FeCl_3$ as the iron precursor.[151] The addition of sodium acetate (NaAc) was found to play a crucial role in the formation of the TNP structure. The optimal amount of NaAc resulted in the fabrication of well-defined TNPs, while deviations from this amount led to the formation of pseudoctahedral or irregular TNPs. The addition of NaAc was crucial for the formation of well-defined TNPs, while deviations from the optimal amount resulted in pseudoctahedral or irregular TNPs. PDA and ethylene glycol (EG) also played significant roles in shaping Fe_3O_4 TNPs. Substituting PDA with other compounds led to the formation of Fe_3O_4 microspheres, while replacing EG with diethylene glycol resulted in irregular nanoparticles. The shape transformation of TNPs is influenced by the volume ratio of EG to PDA, wherein varying ratios result in TNPs with different structures, such as polyhedral structures, perfect TNPs, or octahedral structures.

Zhang *et al.* demonstrated that pH and concentration of oxidant could regulate the shape of iron oxide nanocrystals (Fe_3O_4 and α-Fe_2O_3) in hydrothermal synthesis. By carefully manipulating the experimental conditions, they prepared a series of well-controlled morphologies including 0D octahedra and cubes, 1D rods and wires, and 2D plates (Fig. 6d).[152] At a higher pH value of 12.95, Fe_3O_4 octahedra with an average lateral size of approximately 150 nm were obtained using $FeSO_4$ as the iron precursor. Subsequently, by increasing the amount of oxidant (KNO_3) by 10-fold, rod-shaped Fe_3O_4 structures with a width of 20 nm and lengths ranging from 300 to 400 nm were achieved. Conversely, at a relatively lower pH value of 10.01 and lower oxidant concentration, cubic Fe_3O_4 structures with a length of 400 nm were obtained. Furthermore, when the reaction time was extended to 16 h and the reaction temperature was elevated from 100 to 220 °C in the presence of high-molecular-weight polyethyleneimine (Mw = 10,000 $g.mol^{-1}$) instead of polyethyleneimine with a molecular weight of 1,800 $g.mol^{-1}$, these nanocubes were transformed into hexagonal plate structure of α-Fe_2O_3, which had a width of around 1 μm and a thickness of around 100 nm.

Notably, in a modified hydrothermal synthesis approach, other polar solvents could be used as a substitute for water to synthesize 2D iron oxide nanodiscs.[153] Ding *et al.* successfully prepared uniform α-Fe_2O_3 nanodiscs using a solvent mixture of water and ethanol, with sodium acetate as a stabilizer and iron chloride as the precursor. The resulting nanodiscs had a thickness of approximately 26 nm and a mean diameter of 225 nm. These nanodiscs could be thermally reduced to Fe_3O_4 while maintaining their 2D morphology using oleic acid as a reducing agent (Fig. 6e).[154] By partially replacing water with ethylene glycol (EG) (EG/H_2O = 1:1),

Gu *et al.* prepared ultrathin iron oxide nanoplates by a one-pot modified hydrothermal synthesis with iron(II) sulfate as precursor. [155] EG played a critical role in the formation of ultrathin iron oxide nanoplates. When the EG-to-water ratio was 1:1, the nanoplates exhibited a uniform plate-like morphology with a thickness of 10 to 15 nm and a side length of 150 to 200 nm. Higher EG concentrations resulted in thinner Fe_3O_4 nanoplates with a more irregular shape.

Despite their relative success in controlling the structure and morphology of 2D materials, the yields of the desired nanoparticle morphology produced by hydrothermal methods are highly variable. This is mainly attributed to the fact that the system is sensitive to parameters such as purity, temperature and pH and any slight variation from the desired conditions, making it difficult to achieve precise control over the process.

4.3.3. Exfoliation

Exfoliation has emerged as a promising and effective approach for large-scale production of various 2D materials, including graphene, hexagonal form boron nitride (h-BN), transition metal dichalcogenides (TMDS), transition metal trichalcogenides, metal halides, clays, layered double hydroxides (LDHs), oxides and other layered compounds.[156–161] In recent years, this strategy has also been successfully applied to the synthesis of 2D manganese oxide nanomaterials and their derivatives. These nanosheets exhibit inherent paramagnetic properties, making them highly valuable for bio-applications such as magnetic hyperthermia and MRI.[81,162]

Notably, the Ajayan group recently achieved a significant milestone by preparing 2D "hematene" from natural iron ore hematite α-Fe_2O_3 for the first time (Fig. 7a). The hematite ore was initially ground into a fine powder, followed by dispersion in *N,N*-dimethylformamide (DMF) and subjected to 50 h of sonication.[163] In a followed study by Kumar *et al.*, $FeCl_3$ was utilized as the precursor,

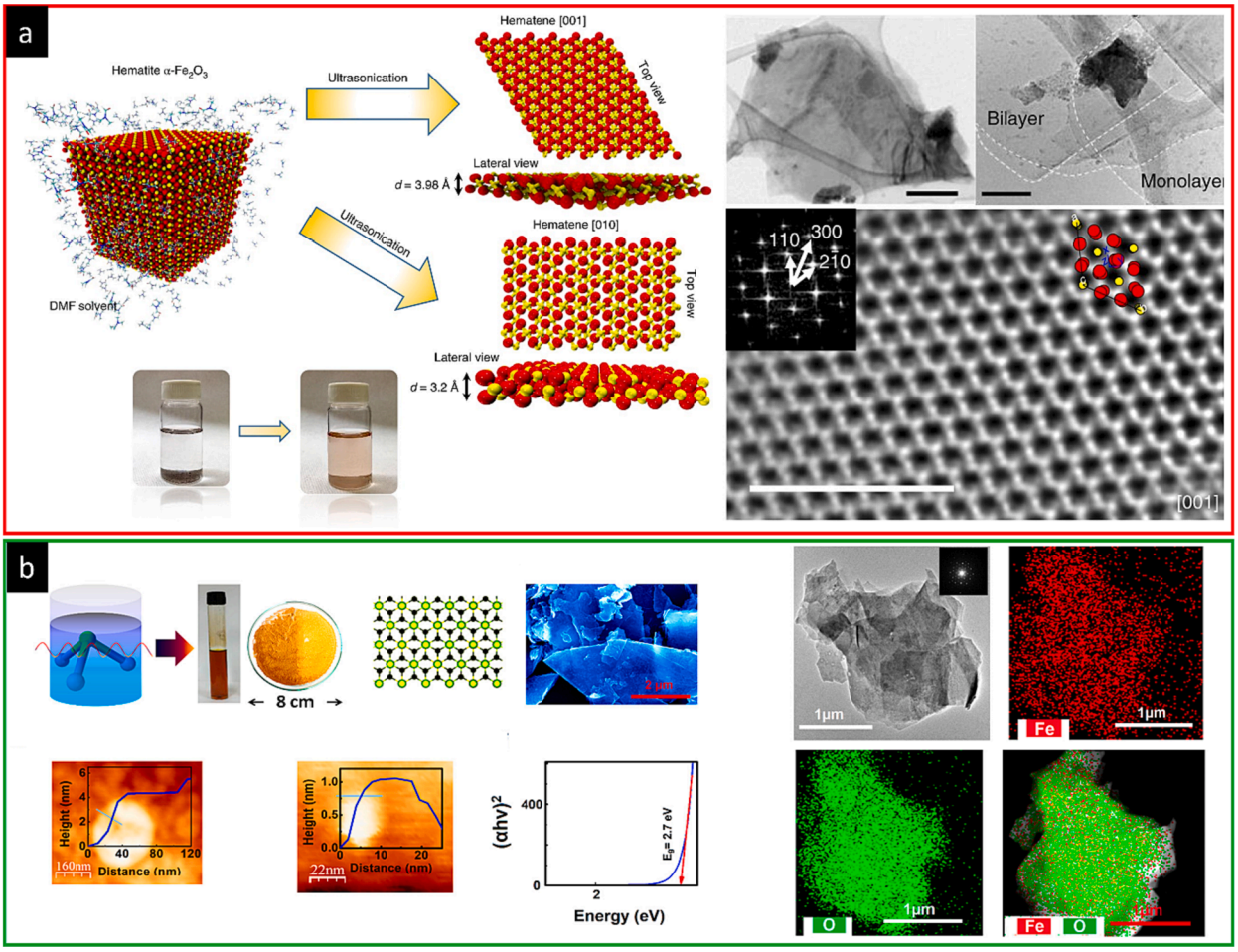

Fig. 7. (a) Left panel: schematic of the exfoliation of bulk hematite in DMF to hematene. Right panel: TEM images (top left, scale bar, 500 nm) and high-magnification bright-field TEM image (top right, scale bar, 50 nm) of hematene; (bottom panel) HRSTEM image of hematene in the [0 0 1] orientation with its Fourier transform in the inset and position of atoms shown by red (oxygen) and yellow (iron) spheres. Scale bar, 2 nm. Adapted with permission from ref.[163], copyright 2018, Springer Nature. (b) Left panel: schematic illustration for synthesizing hematene using $FeCl_3$ as precursor, and the corresponding 2D structure, layer height and XPS spectrum of the synthesized hematene. Right panel: TEM image and elemental mapping of synthesized hematene sheets. Adapted with permission from ref.[164], copyright 2019, American Chemical Society. (For interpretation of the references to color in this figure legend, the reader is referred to the web version of this article.)

with DMF serving as the solvent, and microwave radiation employed as the power source (Fig. 7b).[164] The researchers observed that employing dilute solutions with a low concentration of the precursor as the solute, coupled with high microwave power, facilitated the preferential growth of 2D crystals.

Hematene, synthesized through exfoliation, displays a weak ferromagnetic phase and high saturation at room temperature. It also exhibits improved photocatalytic activity when combined with wide bandgap semiconductors.[163,165] Moreover, when hematene is engineered with nanostructures and oxygen vacancies, it becomes a remarkably efficient catalyst for the oxygen evolution reaction, outperforming even the state-of-the-art IrO_2/C catalyst.[166] Although exfoliated hematene nanosheets are fully oxygen-passivated, stable under ambient conditions, and possess distinct magnetic properties like a striped ferrimagnetic ground state with a small net magnetic moment,[167] their potential applications in the field of biotechnology remain largely unexplored.[168]

4.4. Challenges associated with the application of thermal decomposition

The thermal decomposition method has proven to be a prevalent approach for creating uniform anisotropic MIPs in various dimensions (0D, 1D, and 2D). This method is favoured for proof-of-concept research due to its precise control over the resulting nanoparticle characteristics. However, it does present two noteworthy drawbacks that impede its biomedical applications. Firstly, the thermal decomposition process hinges on the controlled nucleation and subsequent growth procedure of the nuclear core, both of which are profoundly influenced by synthesis conditions such as solvent polarity, temperature, precursor and ligand types, heating procedure, and the protective atmosphere. This sensitivity makes scaling up a challenge, resulting in yields that fall short of meeting industry and clinical demands. For instance, in the context of clinical trials for magnetic hyperthermia therapy, a gram-scale dose per patient is often essential.

Extensive efforts have been directed towards scaling up the thermal decomposition synthesis of iron oxide over the past two decades. Notably, in 2004, Hyeon *et al.* achieved ultra-large-scale syntheses (up to 40 g) of monodisperse iron oxide nanocrystals using iron oleate as a precursor.[83] Subsequently, they developed a method for the large-scale synthesis of extremely small-sized iron oxide nanoparticles in 2011.[92] Expanding on these achievements, Pellegrino *et al.* in 2023 refined a scale-up approach for preparing anisotropic-shaped MIPs using a high boiling point alcoholic solvent, alkylamine as stabilizing agents, organometallic metal molecules such as iron pentacarbonyl as precursors, along with an aldehyde shape-directing agent.[169]

However, achieving consistent results from one batch to another in 'lab-scale' production remains a challenge. An alternative for large-scale production is continuous synthesis, where the production volume can be increased with longer operation times. Recent advancements highlight flow synthesis of iron oxide nanoparticles using the thermal decomposition method.[170] For instance, in 2020, Torrente-Murciano *et al.* employed continuous microreactors to prepare uniform magnetic Fe@Fe_3O_4 core–shell nanoparticles at a high production rate of 2.6 g per hour.[171] Similarly, in 2023, Gavriilidis *et al.* achieved gram-per-day scale synthesis of iron oxide nanoparticles with controllable sizes in the range of 2–17 nm *via* flow synthesis.[172] Despite the great effort that has been devoted to scaling up thermal decomposition synthesis, the control of the resulting particles is still far from satisfactory. There is therefore still a gap between the real application of thermal decomposition in producing materials for clinical trials.

Another limitation of MIPs synthesized through the thermal decomposition approach is the hydrophobic coating on the particles, rendering them stable only in low-polarity media. Consequently, a post-synthesis surface modification process is necessary to transfer these MIPs into aqueous-based biological environments, a topic addressed in Section 5.

5. Surface modification

To achieve desirable *in vivo* characteristics such as water solubility and colloidal stability under physiological conditions, it is crucial to passivate MIPs by introducing a protective coating layer. This coating not only acts as a barrier against oxidation reactions, but also enhances the cyto- and biocompatibility of MIPs. Additionally, the coating layer also introduces reactive functional groups, such as amine, thiol, and carboxyl groups to the surface of nanoparticles. These functional groups play a vital role in enabling precise and adjustable surface modifications, as well as facilitating effective conjugation with other bioactive molecules, thereby expanding the potential applications of MIPs in biomedicine.[173–175] In the case of MIPs, the ratio of surface atoms to bulk atoms is increased, leading to a greater influence of surface spins on magnetization. Consequently, the surface effect plays a significant role in magnetization, with canted spins becoming more pronounced. The presence of a coated layer on the surface of MIPs can further alter the canted shell, either positively or negatively.[176–178] For instance, it has been observed that oleic acid can reduce the magnetic surface anisotropy, resulting in magnetite nanoparticles without surface spin canting. This absence of spin canting in particles synthesized through thermal decomposition can be attributed to two factors: the high synthesis temperature and the presence of oleic acid molecules covalently bonded to the particle surface.[179] A notable study conducted by Begin-Colin *et al.* involved the preparation of magnetite-based nanoparticles that were phosphonated and carboxylated. Interestingly, spin canting was only observed in the carboxylated particles. The researchers proposed a hypothesis suggesting that carboxylate interactions restrict the surface exchange bonds, whereas phosphonate interactions enable further superexchange magnetic interactions.[180] Therefore, when selecting materials for coating MIPs, careful consideration should be given to their potential impact on the surface canting phenomenon, as the choice of coating materials can significantly influence the magnetic properties of MIPs.

Depending on the materials, surface modifications can be classified into 3 broad groups: small molecular ligands, macromolecules (polymers and hydrogels), inorganic materials (including silica, metal or metal oxide *etc.*).[181] It is worth mentioning that the surface coating is mainly determined by the surface chemistry of the MIPs and hence they can be applied regardless of the 0D, 1D or 2D structure/shape, as the surface chemistry is mappable across these different structures. Therefore, in this section some representative

reference includes both the coating on spherical and non-spherical magnetic nanoparticles. The general surface modification chemistry has been well-reviewed by others[182–187] and here we only list a few typical materials widely used for the modification of MIPs.

5.1. Surface engineering with organic surface ligands

MIPs prepared through thermal decomposition are typically stabilized using hydrophobic ligands, necessitating additional engineering to render them hydrophilic for biological applications.[188,189] There are three main approaches to achieve hydrophilic ligand stabilized MIPs: ligand exchange, ligand post-modification and secondary-ligand insertion. Ligand exchange requires the second ligand featuring stronger anchoring groups to displace the initial ligand and form metal–ligand coordination onto the surface of inorganic nanocrystals, together with hydrophilic segments to enhance the MIPs' affinity to water.[190,191] Taking advantage of well-designed functional moieties of the initial ligand, ligand post-modification is usually achieved through post-chemical reactions to convert initial ligand into its corresponding hydrophilic derivatives.[192] Instead of complete removal of the initial ligand or modification of its chemical structure, an alternative approach is secondary-ligand insertion. This involves introducing an amphiphilic ligand together with the initial ligand onto the surface of the MIPs. The combination of these ligands forms a bilayer structure coating through hydrophobic interactions, effectively enhancing the hydrophilic properties of the MIPs.[193]

A good example of ligand exchange was shown by Gao *et al.* who prepared hydrophobic Fe_3O_4 particles through conventional thermal decomposition method by using oleic acid and oleylamine as surface ligands.[194] To achieve ligand exchange, three types of polyethylene glycol with diphosphate, hydroxamate, and catechol groups were chosen (Fig. 8a). These groups exhibited higher binding affinities to Fe^{3+} compared to the anchoring groups of the initial hydrophobic ligands. The ligand exchange process resulted in MIPs with enhanced aqueous dispersibility. Furthermore, the chemical structure of the anchoring groups had a significant impact on the MRI properties, specifically the r_2 relaxivity and r_2/r_1 ratio. The presence of a conjugated structure in the anchoring group notably amplified the T_2 effect by increasing the inhomogeneity of the local magnetic field. Notably, although ligand exchange is simple, incomplete exchange or desorption of ligands could lead to the loss of colloidal stability in aqueous media.

Post surface modification of the chemical structure of the initial ligand is another effective method to convert hydrophobic MIPs into hydrophilic ones.[192] An illustrative example of direct surface modification for achieving hydrophilicity is demonstrated by Lin *et al.*[195] They proposed a straightforward and scalable synthesis approach towards hydrophilic nanoparticles through the direct modification of oleic acid (OA) or oleylamine (Oam) ligands using thiol-terminated poly(ethylene glycol) (HS-PEG) *via* ultraviolet-induced thiol-ene chemistry (Fig. 8b). The integration of active groups, such as carboxylic acid (HS-PEG-COOH) and amine (HS-

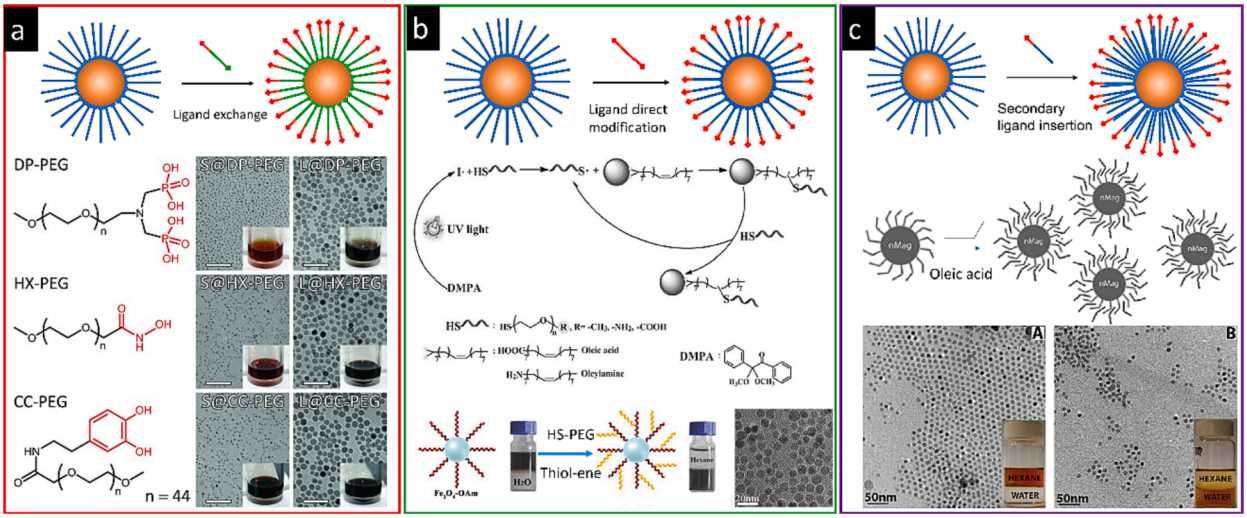

Fig. 8. (a) Top panel: a schematic illustration of ligand exchange with a hydrophilic ligand. Bottom left panel: chemical structures of three type of PEGs used for exchanging the hydrophobic ligands. Bottom right panel: TEM images of the PEGylated particles (scale bars, 50 nm); Insets: photographs of aqueous solutions of the PEGylated Fe_3O_4 particles. (b) Top panel: a schematic illustration of direct modification on the initial hydrophobic ligand. Middle panel: schematic illustration of the surface modification through thiol–ene click chemistry and the corresponding reactive mechanism. Bottom left panel: schematic illustration of the surface modification process by thiol–ene click reaction for oleylamine-capped Fe_3O_4 nanoparticles. Photographs show the soluble properties of the Fe_3O_4 particles in H_2O and hexane mixture before and after modifications. Bottom right: TEM image presents the morphologies of the HS-PEG1000-modified Fe_3O_4 particles (scare bar corresponds to 20 nm). (a-b) were adapted with permission from ref.[194,195], respectively, copyright 2014 and 2017 Wiley-VCH. (c) Top panel: a schematic illustration of the secondary ligand insertion to form a bilayer structure together with the initial hydrophobic ligand. Middle panel: schematic illustration of the aqueous transfer of iron oxide nanoparticles via the introduction of oleic acid as the 'secondary ligand' to form bilayers on the surface of nanoparticles. Transmission electron micrographs of iron oxide nanoparticles (bottom left panel) in organics, (bottom right panel) phase transferred into water via bilayer formation. Inset pictures show phase separated mixtures with water phase at the bottom and hexane phase at the top. Adapted with permission from ref.[197], copyright 2009 American Chemical Society.

PEG-NH_2), into the oligo PEG structure was feasible, enabling additional bioconjugation possibilities. This versatile method can be applied to various hydrophobic nanocrystals with diverse compositions, including rare earth, metal oxides, and metal sulfides, as well as nanoparticles with different morphologies.

Another frequently employed approach to alter the hydrophobic particles while preserving the integrity of the original ligand is by inserting a secondary amphiphilic ligand/surfactant to create a bi-layer coating. For example, Hyeon *et al.* utilized

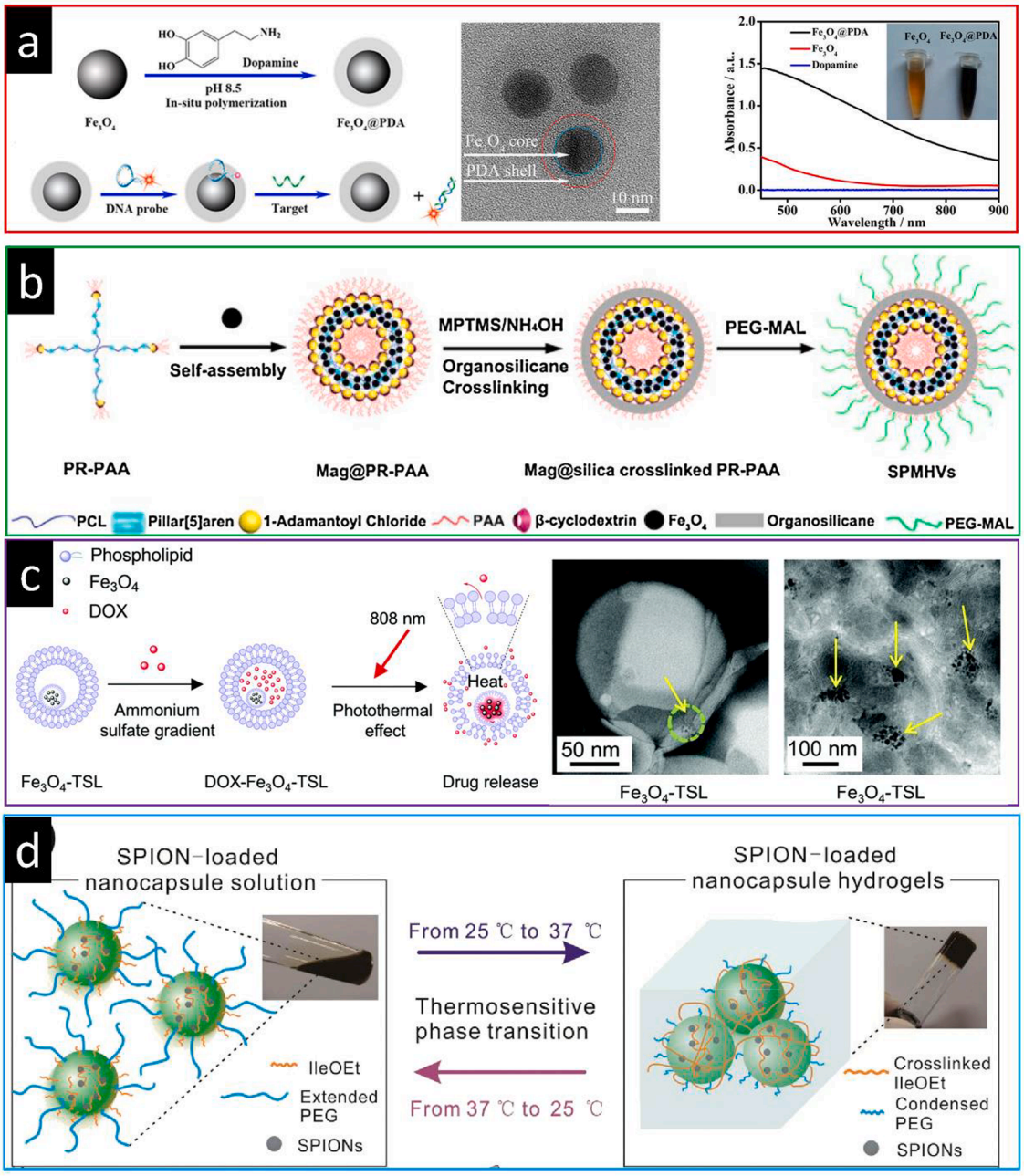

Fig. 9. (a) Left panel: schematic illustration of the preparation of Fe_3O_4@PDA nanocomposites (NC). Middle panel: representative TEM images of synthesized Fe_3O_4@PDA nanocomposites. Right panel: UV–vis absorption spectra of Fe_3O_4 nanoparticles (0.1 mg mL_{-1}) before and after PDA coating. The inset photo shows the colour change between Fe_3O_4 NPs and Fe_3O_4@PDA NCs. Adapted with permission from ref.[208], copyright 2014 American Chemical Society. (b) Schematic illustration for the synthesis of supramolecular PEGylated magnetic hybrid vesicles (SPMHVs). Adapted with permission from ref.[209], copyright 2018 Elsevier. (c) Left panel: schematic illustration of the NIR-triggered DOX release from DOX–Fe_3O_4– thermosensitive liposomes (TSL). Right panel: representative TEM images of Fe_3O_4–TSL. Adapted with permission from ref.[211], copyright 2019 Royal Society of Chemistry. (d) Schematic illustration of the composition of SPION-loaded nanocapsule and thermosensitive phase transition from solution to hydrogel. Adapted with permission from ref.[219], copyright 2016 Elsevier.

cetyltrimethylammonium bromide (CTAB), a well-known molecular surfactant, for the translocation of hydrophobic Fe_3O_4 into the aqueous phase. The CTAB not only functions as a stabilizing agent but also serves as organic template for the subsequent formation of mesoporous silica.[196] Colvin *et al.* successfully transferred hydrophobic oleic-acid stabilized MIPs to the aqueous phase by simply introducing very little fatty acid (*e.g.* 0.2 w/w %) to the system (Fig. 8c).[197] Furthermore, a large group of molecular surfactants have been proven to be effective in phase transition through the formation of bilayer coating.[193,198–200]

To enhance tumor targeting, surface modification of MIPs with specific ligands is a promising approach. Ligands such as folic acid, hyaluronic acid, lactobionic acid, and antibodies have been used to functionalize MIPs for cancer cell targeting.[78] For a representative example, Shi *et al.* demonstrated the functionalization of citric acid-covered Fe_3O_4 nanoparticles (NPs) with folic acid (FA) and a light-addressable unit diazirine (DA) to create ultrasmall Fe_3O_4 -PEG-(DA)-FA NPs. These particles exhibited cytocompatibility, targeted specificity to arthritis-associated macrophage cells mediated by FA, and tunable relaxivities. The modified MIPs hold great promise for targeted cancer therapy, with prolonged accumulation at tumor sites.

5.2. Surface engineering with polymer coating

The surface modification of MIPs with polymers, including polyethylene glycol (PEG), polyvinyl alcohol (PVA), polyethylenimine (PEI), polyacrylic acid (PAA), poly(lactic acid) (PLA), poly(lactide-co-glycolide) (PLGA), poly(amino acid) copolymers, as well as natural polymers like dextran and proteins, offers a versatile approach to control the interface properties of MIPs. These polymer-coated MIPs provide several advantages, such as reduced toxicity, enhanced repulsive forces to counterbalance attractive forces, and facile functionalization.[201,202] Additionally, the incorporation of polymers enables the development of multifunctional MIPs for magnetic theranostics. Stimuli-responsive coatings can be engineered using polymeric materials, which undergo structural changes in response to specific stimuli such as variations in pH, ionic strength, light, temperature, and more. These responsive coatings enable controlled release of encapsulated payloads at the desired location, enabling targeted and precise delivery capabilities.[203]

Among a plethora of polymers, polydopamine (PDA) is one of the most straightforward and highly versatile choices for functionalizing materials surfaces.[204,205] During polymerization, PDA exhibits a remarkable ability to spontaneously generate a conformal and continuous coating layer on a wide range of materials, including noble metals, metal oxides, semiconductors, ceramics, and synthetic polymers.[206] The strong binding affinity of catechol functional groups enables the effective adhesion of PDA onto these surfaces. For instance, Xue *et al.* developed a nanocomposite material with integrated photothermal and nitric oxide (NO)-releasing properties by utilizing a PDA coated iron oxide nanocomposite (Fe_3O_4@PDA) as a photoconversion agent.[207] They grafted three generations of dendritic poly(amidoamine) (PAMAM-G3) on the surface of Fe_3O_4@PDA and loaded nitric oxide in the dendritic polymer shell. The resulting nanocomposite exhibited synergistic photothermal effects and controllable NO release under intermittent 808 nm laser irradiation. In another example, Liu *et al.* synthesized Fe_3O_4@PDA core–shell nanocomposites through an *in situ* self-polymerization method (Fig. 9a).[208] The PDA in the composite was capable of adsorbing dye-labelled ssDNA probes and exhibited high fluorescence quenching efficiency. As a result, the Fe_3O_4@PDA nanocomposites demonstrated effective nanoprobes for the detection of mRNA in living cells. Furthermore, the Fe_3O_4@PDA nanocomposites possessed magnetic properties due to the Fe_3O_4 core and exhibited near-infrared (NIR) absorption due to the PDA, enabling their application in both MRI and photoacoustic imaging.

Amphiphilic and supramolecular polymers are commonly employed as coating materials for MIPs, enabling the achievement of controllable composite vesicles or micelles through self-assembly. One example is the work by Li *et al.*, who designed and synthesized supramolecular-based PEGylated magnetic hybrid vesicles (SPMHVs) as T_2-weighted MR contrast agents (Fig. 9b).[209] The SPMHVs were formed through the self-assembly of a supramolecular-based amphiphilic pseudo-block copolymer called polyrotaxane-poly (acrylic acid) (PR-PAA) with hydrophobic magnetite nanoparticles. The resulting vesicles could be tuned between vesicular and micellar morphology by adjusting the initial Fe_3O_4 concentrations in the oil phase. SPMHVs with well-defined vesicular morphology, small particle sizes (<100 nm), and excellent colloidal stability were achieved. Notably, these SPMHVs exhibited a remarkable increase in the exchange rate of water protons and a decrease in the water diffusion coefficient, leading to an ultra-high r_2 value of up to 641.7 mM^{-1} s^{-1} *in vitro*.

Liposomes are highly regarded in biomaterials research due to their biocompatibility and versatile functionalities. They have the ability to enhance solubility, protect drugs, and respond to external stimuli for controlled drug release.[210] For example, Wu *et al.* developed magnetic nanoparticles-loaded thermosensitive liposomes (Fe_3O_4-TSL) for combined photothermal-chemotherapy of tumors (Fig. 9c). These liposomes efficiently delivered the anticancer drug doxorubicin (DOX), exhibited tumor accumulation, heat generation under near-infrared (NIR) laser, and enhanced magnetic resonance imaging (MRI) contrast.[211] Very recently, cells membrane such as red blood cells (RBC) or macrophage membranes have recently been found to be a powerful tool to functionalize nanoparticles for bioapplications due to their native long prolonged blood circulation, high biocompatibility, immune-evasion and reduced acerated blood clearance effect.[212–214] For example, Sun *et al.* developed magnetic nanoparticles coated with myeloid-derived suppressor cell (MDSC) membranes to achieve active tumor targeting by harnessing the host immune system. By coating the nanoparticles with MDSC membranes, they not only evade the immune system's attack on MDSCs but also benefit from the increased presence of MDSCs. These MDSC membrane-coated iron oxide nanoparticles demonstrated exceptional performance in immune escape, tumor targeting, magnetic resonance imaging (MRI), and photothermal therapy-induced tumor eradication.[215] In another study, Liu *et al.* introduced a microfluidic electroporation method for the synthesis of red blood cell (RBC) coated magnetic nanoparticles (MIPs).[216] By applying electric pulses, MIPs could be efficiently fused with RBC vesicles in a scalable manner. The resulting particles exhibited prolonged circulation in the bloodstream and demonstrated improved MRI of tumors, as well as enhanced efficacy in photothermal therapy.

Hydrogels as an emerging important biomaterial[217,218] have been recently applied to MIPs coating. Song *et al.* proposed a

system called superparamagnetic iron oxide nanoparticle-loaded nanocapsule hydrogels (SPION-NHs) (Fig. 9d). These hydrogels are injectable, biodegradable, thermosensitive, and contain SPIONs for multiple magnetic hyperthermia therapy and long-term MRI contrast.[219] The amphiphilic polymer polyphosphazene (PPZ) forms self-assembled polymeric nanocapsules that effectively trap hydrophobic SPIONs by utilizing hydrophobic interactions between the PPZ polymer backbone and the alkyl chains of oleic acid on the surface of the SPIONs. This interaction leads to the formation of a core–shell structure. Importantly, when the SPION-loaded nanocapsule solution was injected at body temperature, the hydrophobic interaction triggered its transformation into a hydrogel form. Such a transformation is significant as it allows the SPIONs to remain within tumors for over three weeks following a single injection of SPION-NHs. This extended retention period greatly facilitates successful multiple magnetic hyperthermia therapy. This extended retention time is advantageous compared to traditional magnetic nanoparticle fluids, which have shorter retention times and are unable to generate enough heat for repeatable treatment. In another study, Bañobre-López *et al.* developed a biocompatible composite hydrogel based on xanthan gum (XG) and Fe_3O_4 magnetic nanoparticles.[220] The hydrogel exhibited magnetically responsive properties for thermally induced controlled drug delivery *via* magnetic hyperthermia and allowed non-invasive monitoring through MRI. With prolonged sustained release and enhanced antifungal activity, the XG/Fe_3O_4 magnetic nanoparticle composite hydrogel represent a versatile theranostic platform for injection and implantation in clinical scenarios.

5.3. Surface engineering with inorganic coatings

Inorganic shells like carbon,[221] silica,[181] metal or metal oxide,[222] provide protective layers against oxidation or reactive species and enable facile surface modification. Gold shells are biocompatible, inert, and easily modified by thiol-containing ligands.[223] Silica is a commonly employed material for functionalizing magnetic nanoparticles due to its biocompatibility and the ease of modification using commercially available silane compounds.[224] From a geometric perspective, the inorganic coating can be classified into three main structures: single-layer core–shell; multi-layers core-shells; disconnected stacked shells, often known as yolk-shell.

The single-layer core–shell structure represents the most conventional and traditional form of coating. A representative example is that by Zhang *et al.* who prepared a multifunctional theranostic magnetic mesoporous silica nanoparticle (MMSN) with a magnetic core, which was developed for magnetic-enhanced tumor-targeted MR imaging and precise therapy (Fig. 10a).[225] The surface of the mesoporous silica shell was modified by immobilizing β-cyclodextrin (β-CD) as a gatekeeper through platinum(IV) prodrug linking, enabling reduction-triggered intracellular drug release. Additionally, they introduced an Arg-Gly-Asp (RGD) peptide ligand onto the β-CD gatekeeper *via* host–guest interaction, enhancing cancer targeting capabilities. This multifunctional MMSN demonstrated selective uptake by cancer cells and effectively induced the intracellular redox-sensitive release of the anticancer drug, leading to the elimination of cancer cells.

In practical biomedical applications, nanocomposites need to possess multiple functionalities to fulfill the requirements of an ideal platform, including imaging, diagnosis, and drug delivery capabilities. To achieve this, the use of multi-layered coatings has been employed to fabricate theranostic platforms that integrate both therapeutic and diagnostic functions. For example, Yeh *et al.* developed a multimodal nanocarrier by incorporating gold onto the surface of iron oxide nanoparticles, thereby combining magnetic and plasmonic functionalities. Subsequently, a mesoporous SiO_2 ($mSiO_2$) nanoshell was fabricated onto the Fe_3O_4@Au surface, resulting in the formation of Fe_3O_4@Au@$mSiO_2$ nanoparticle (Fig. 10b).[226] This innovative design allows the nanocarriers to possess magnetic targeted drug delivery, MRI-monitored magnetic targeting of tumors, near-infrared (NIR) photothermal ablation and on-demand drug release capabilities. By integrating these functionalities into a single platform, the nanocomposites exhibit enhanced potential for precise and efficient cancer treatment, imaging, and therapy monitoring.

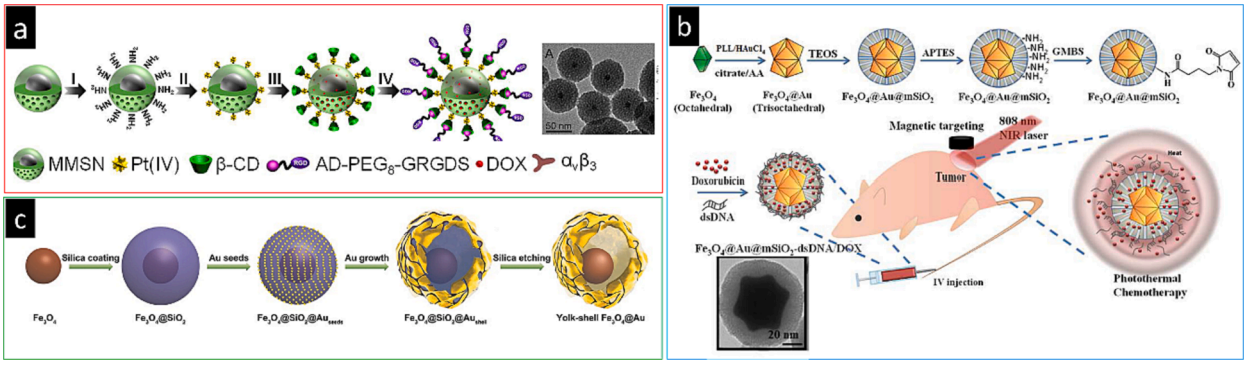

Fig. 10. (a) Schematic illustration of the design of the multifunctional magnetic mesoporous silica nanoparticles (MMSNs) and representative TEM image of MMSN. Adapted with permission from ref.[225], copyright 2016 Elsevier. (b) Schematic illustration of the synthesis process of Fe_3O_4@Au@$mSiO_2$-dsDNA/DOX nanocomposites for therapy combining chemotherapy and photothermal treatment of cancer cells. Inset: Representative TEM image of Fe_3O_4@Au@$mSiO_2$ nanoparticles. Adapted with permission from ref.[226], copyright 2014 American Chemical Society. (c) Scheme showing the synthesis of yolk–shell Fe_3O_4@Au NPs using SiO_2 as the sacrificial template. Adapted with permission from ref.[227], copy right 2017 Wiley-VCH.

Taking this concept one step further, surface coatings can also be designed as disconnected stacked shells, which offer unique advantages in terms of core protection and influence on physical/chemical properties. For example, Chen *et al.* designed yolk–shell structured magnetic–plasmonic hybrid nanoparticles (MPHNs) consisting of a Fe_3O_4 core within a hollow cavity surrounded by a porous Au outer shell (Fig. 10c).[227] In contrast to the conventional core–shell MPHNs, where the water-impermeable coating limits the proximity of protons to the magnetic portion, the introduction of a hollow cavity between the magnetic and plasmonic components in the yolk-shell structure significantly mitigates the decline in relaxivity of the Fe_3O_4 core caused by the Au layer. This design feature allows for improved magnetic resonance imaging (MRI) performance. Furthermore, the yolk-shell Fe_3O_4@Au nanoparticles offer additional benefits. The porous outer shell not only provides high near-infrared absorption for plasmonic component-based imaging techniques such as photoacoustic (PA) and positron emission tomography (PET), but also enables NIR light-induced chemothermal synergistic therapy. Additionally, the hollow cavity and pores within the outer shell offer ample storage space and release channels for anticancer drugs, making the yolk-shell Fe_3O_4@Au nanoparticles promising candidates for light-triggered hyperthermia and controlled drug release.

6. Impact of shape-dependent properties on bio-applications

Due to their biocompatibility and ability to enhance proton relaxation under an external magnetic field, MIPs possess unique material properties and an integrated design capacity for cell targeting, imaging, and therapy. This makes them an ideal platform for theranostics. In this section, we will investigate and compare the performances of 0D, 1D, and 2D magnetic nanomaterials in various biological applications. We will critically assess the relationships between structure and properties, as well as identify areas for expansion and improvement in the field.

6.1. Magnetic resonance imaging (MRI)

MRI is widely recognized as a powerful non-invasive imaging modality in clinical medicine due to its exceptional soft tissue contrast, high spatial resolution, absence of ionizing radiation, deep signal penetration, and broad clinical applicability.[228] The fundamental principle of MRI is based on nuclear magnetic resonance (NMR) and the relaxation of proton spins in a magnetic field. When subjected to brief radiofrequency (RF) energy pulses, the protons in water molecules undergo excitation within microseconds. Subsequently, they gradually return to their equilibrium state through relaxation processes. Two distinct relaxation pathways are involved in this process. The first pathway, known as longitudinal or T_1 relaxation, corresponds to the recovery of the net magnetization (M_z) to its initial state. The second pathway, referred to as transverse or T_2 relaxation, involves the loss of magnetization in the perpendicular plane (M_{xy}) due to the dephasing of spins. The emitted signal during relaxation is translated into familiar grayscale images by capturing spatially resolved electron signals.[228]

Despite the advantages of MRI, there are limitations in clinical diagnostics, particularly in achieving sufficient contrast and signal-to-noise ratio. To address this, contrast agents (CAs) are utilized to enhance the MR signal of water protons in the surrounding tissues. CAs can be classified into two major types based on their impact on relaxation processes: (1) Positive contrast agents: These agents primarily reduce the longitudinal T1 relaxation time, resulting in bright MR images. Gd^{3+}- based paramagnetic complexes are commonly used as positive contrast agents. They accelerate the T_1 relaxation process through strong dipolar interactions between protons and unpaired electrons. (2) Negative contrast agents: These agents primarily reduce the transverse T_2 relaxation time, leading to areas of hypointense signal and dark MR images. Superparamagnetic nanoparticles are an example of negative contrast agents. They accelerate the T2 relaxation process by inducing rapid loss of phase coherence through their strong local magnetic field gradient.[229]

In general, the relaxation time (T_i) of water protons can be expressed by Equation (1), where incorporates both the intrinsic relaxation time of the tissues or external environment (T_{io}) and the contrast agent contribution (T_i^{CA}).

$$\frac{1}{T_i} = \frac{1}{T_{i0}} + \frac{1}{T_i^{CA}} (i = 1, 2) \tag{1}$$

The contrast ability of an agent can be quantitatively characterized by its longitudinal and transverse relativities. The relativity values indicate the magnitude to which a contrast agent can enhance the hydrogen nucleus relaxation rate constant R_i normalized to the millimolar concentration of the agent, as shown in Equation (2).[230]

$$R_i^{CA} = \frac{1}{T_i^{CA}} = r_i[CA] (i = 1, 2) \tag{2}$$

6.1.1. T_2 Contrast agents

MIPs have been widely used as contrast agents in MRI since their first application 20 years ago. They are primarily employed as T_2 contrast agents due to their ability to induce T_2 relaxation effects. This is attributed to their high magnetization values, which create microscopic field variations leading to accelerated dephasing of protons. Consequently, neighboring regions experience shortened T_2 relaxation times, resulting in increased hypointense signal intensity in T_2-weighted MR images. The effectiveness of MIPs in enhancing proton relaxation rates is described by their relaxivity (r_2 or $1/T_2$). In a simplified approximation, r_2 is related to the square of the saturation magnetization (M_S) of the nanoparticles.[231] The magnetic properties of iron oxide nanoparticles are influenced by various factors, including their size, composition, shape, and surface characteristics. These parameters can be controlled to improve the MR contrast properties of MIPs. Research studies have demonstrated that non-spherical nanocrystals exhibit higher relaxivities

compared to spherical counterparts. This is largely attributed to their larger effective radii, which have a stronger impact on the relaxation rates of surrounding water proton spins. Based on this premise, the controllable synthesis of uniform MIPs in different morphologies, such as 0D spheres, octopods, cubes, 1D rods, and 2D plates, provides a valuable tool for investigating how shape influences their behavior in MRI.

The T_2 relaxation, which leads to spin–spin relaxation, occurs when magnetic nanoparticles cause the dephasing of magnetic moments due to the magnetic-field gradients generated by the MIPs. According to the outer sphere motional average regime theory, [232,233] the r_2 relaxivity is given by (where the nanoparticles can be simulated as spheres):

$$r_2 = \left(256\pi^2\gamma^2/405\right) * kM_S{}^2r^2 \Big/ D\left(1+\frac{L}{r}\right) \tag{3}$$

Where M_s and r represent the saturation magnetization and effective radius of the magnetic nanostructure, respectively, it is therefore important for nanoparticles to possess a larger magnetization and a larger effective magnetic core radius to be efficient T_2 contrast agents. Additionally, factors such as the diffusion coefficient (D), thickness of an impermeable surface coating (L), and conversion factor (k) also play roles in the overall efficiency of the nanoparticles as T_2 contrast agents. However, a larger magnetization and effective magnetic core radius are particularly critical considerations for achieving optimal T_2 contrast in MRI.

The T_2 MRI performance of ferromagnetic particles is influenced by the non-spherical shape of the particles, which can be attributed to three main factors: an additional contribution to the anisotropy energy, improved saturation magnetization, and a larger

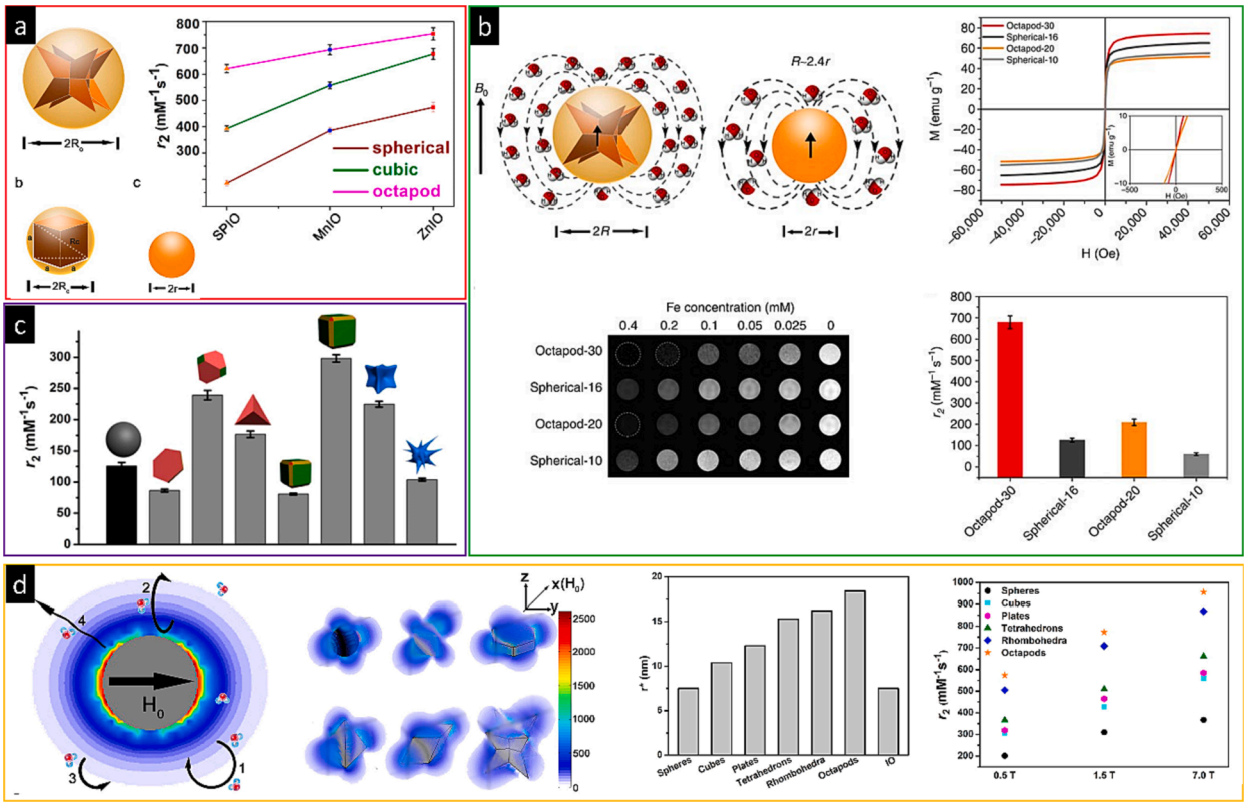

Fig. 11. (a) Comparison of the effective radii of octapod, cubic, and spherical nanoparticles, and comparison of r_2 of SPIO, MnIO, and ZnIO with different morphologies and effective radii. adapted with permission from ref.[236], copyright 2016 American Chemical Society. (b) Top left panel: schematic illustration to show the ball models of octapod and spherical iron oxide nanoparticles with the same geometric volume; Top right panel: the M−H curves of Octapod-30 and Octapod-20 (octapod iron oxide nanoparticles with average edge lengths of 30 nm and 20 nm, respectively), Spherical-16 and Spherical-10 (spherical nanoparticles with mean diameters of 16 nm and 10 nm, respectively) measured at 300 K (inset: M−H curves of Octapod-30 and Octapod-20 in low-magnetic field areas). Bottom left: T_2-weigthed MR images of Octapod-30, Octapod-20, Spherical-16 and Spherical-10 in aqueous solution with 1 % agarose at various concentrations of iron using a Varian 7 T microMRI scanner. Bottom right: comparison of r_2 values of Octapod-30, Octapod-20, Spherical-16 and Spherical-10. Adapted with permission from ref.[94], copyright 2013 Nature Portfolio. (c) comparison of r_2 of anisotropic iron oxide nanostructures with spherical shaped iron oxide nanoparticles. (d) Left panel: (left scheme) water molecular diffusion and relaxation process around spherical magnetic NPs. The color indicates the intensity of local field induced by magnetic NPs under an external magnetic field (H_0); (right scheme) the spatial distribution of stray field of the six different shapes when the external magnetic field H_0 is along the longest diagonal of the MIPs. The color bars illustrate the strength of the stray field. Middle panel: the effective radius (r*) of MnIO and IO NPs with different geometries. Right panel: the r_2 of the MnIO and IO NPs at 0.5, 1.5, and 7.0 T. (c) and (d) were adapted with permission from ref.[237,238], copyright 2015 and 2018 American Chemical Society.

effective radius. (1) Anisotropy Energy: The magnetic behavior of nanoparticles is governed by particle anisotropy, which includes magnetocrystalline anisotropy (dependent on crystal structure), stress anisotropy (dependent on applied or residual stress), and shape anisotropy (dependent on grain shape). Shape anisotropy arises from the demagnetizing field and relies on the shape of the particle. Symmetric spheres have no net shape anisotropy.[11] Importantly, the relative saturation magnetization depends largely on the magnetic anisotropy value for each particle size. Non-spherical particles with shape anisotropy can induce magnetic field inhomogeneities, causing nearby proton magnetic moments to precess at different rates. This results in accelerated reduction in phase coherence and shorter T_2 relaxation times.[26,234] (2) Spherical nanoparticles exhibit multiple facets, leading to increased surface spin disorder and lower M_s values. In contrast, non-spherical particles such as octahedral, cubic, wire, and rod-shaped nanoparticles have fewer facets and lower degrees of spin disorder, resulting in higher M_s values.[14,16,24,25] Higher M_s values have a greater impact on proton relaxation, typically leading to improved MRI contrast. (3) Anisotropic particles generally possess a larger effective magnetic core radius. The effective radius determines the area of field perturbation for outer sphere protons, which dominates the relaxation mechanism and is proportional to the achievable T_2 relaxivity.[234] Therefore, particles with larger effective radii have increased T_2 relaxivity, contributing to enhanced MRI contrast.

6.1.1.1. Non-spherical 0D vs spheres. The presence of MIPs with anisotropic shapes can induce local field inhomogeneity due to their shape anisotropy.[25,94,234] This shape-induced effect leads to a non-uniform distribution of the magnetic field surrounding the particles. As a result, nearby protons experience accelerated dephasing, which significantly shortens the T_2 relaxation time. Furthermore, the surface area of nanostructures directly affects the field perturbation area. Non-spherical particles, in particular, exhibit larger surface areas compared to spherical nanoparticles of similar volumes. As a result, the presence of non-spherical particles leads to more significant interactions between water molecules and the particle surface. This, in turn, enhances water diffusion and influences relaxation processes. The induced local magnetic field around non-spherical particles further contributes to the modulation of water proton behavior, resulting in improved diffusion and relaxation effects. Overall, the combination of a larger surface area and the induced local magnetic field in non-spherical particles offers distinct advantages for water diffusion and relaxation, ultimately contributing to enhanced MRI performance and contrast enhancement.[56,235]

For instance, when comparing magnetic nanoparticles with the same geometric volumes, the effective radii of octapod and cubic superparamagnetic iron oxide (SPIO) nanoparticles are approximately 2.4 and 1.4 times larger than those of spherical SPIO nanoparticles, respectively (Fig. 11a).[236] This larger effective boundary radius contributes to a remarkable increase in the transverse relaxivity (r_2). Specifically, the corresponding r_2 values of spherical, cubic, and octapod zinc doped iron oxide (ZnIO) nanoparticles with equivalent volumetric values are 473.9, 677.5, and 754.2 $mM^{-1}\ s^{-1}$, respectively.

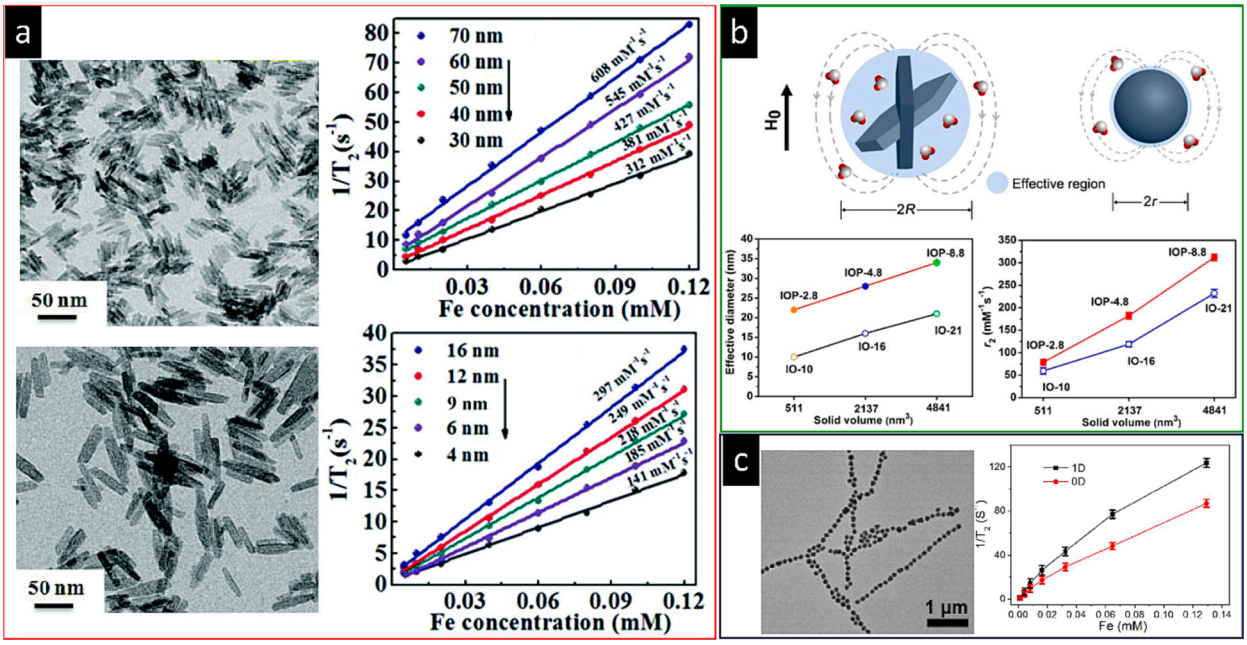

Fig. 12. (a). Representative TEM micrographs of different lengths of Fe_3O_4 nanorods: (top left) 30 ± 5 nm and (bottom left) 60 ± 5 nm. Right panel: Plots of R_2 values of (top right) Fe_3O_4 nanorods and (bottom right) Fe_3O_4 nanoparticle of different sizes. Adapted with permission from ref.[25], copyright 2015 Royal Society of Chemistry. (b) Top panel: comparison of the effective radii of nanoplate and their spherical counterpart that have the equivalent solid volumes. Bottom panel: The comparisons of (bottom left) effective diameter and (bottom right) T_2 relaxivity of nanoplates and spheres. Adapted with permission from ref.[239], copyright 2014 American Chemical Society. (c) Left panel: representative TEM images of the Fe_3O_4 chains. Right panel: T_2 relaxation rates for the dispersed Fe_3O_4 nanoparticles (0D building blocks) and their assembled linear Fe_3O_4 chains (1D), respectively. Adapted with permission from ref.[243], copyright 2014 American Chemical Society.

Gao *et al.* conducted a study where they synthesized octapod iron oxide nanoparticles with controllable sizes and achieved a remarkably high transverse relaxivity value of 679.3 mM^{-1} s^{-1} (Fig. 11b).[94] The researchers employed simulations using a spherical ball model that fully covered the octapod structure to represent the nanoparticles under an external magnetic field B_0. Their simulations revealed that the effective radii of the octapod iron oxide nanoparticles were approximately 2.4 times larger than those of spherical nanoparticles with the same geometric core volumes. In a related investigation by the same research group, the effect of shape on relaxation properties was further explored using Fe_3O_4 particles with different shapes, including plates, tetrahedrons, and octahedrons with Fe_3O_4{1 1 1} facets.[237] Their findings revealed that the T_1 and T_2 relaxation behavior was dependent on the morphology of the particles. Notably, among all the shapes studied, the cube-shaped magnetic iron oxide particles (M_s ~56.1 emu/g) with an edge length of 21 nm exhibited the highest r_2 value of 298.02 ± 5.8 mM^{-1} s^{-1} (Fig. 11c). This significant enhancement in relaxivity can be attributed to their relatively large effective radii of approximately 36.3 nm. In contrast, the spherical magnetic iron oxide particles with a diameter of 16 nm (M_s ~60.5 emu/g) displayed a lower r_2 value of 125.7 ± 5.63 mM^{-1} s^{-1}. These results further emphasize the influence of shape on the relaxation properties of magnetic nanoparticles, highlighting the advantage of non-spherical shapes in achieving enhanced MRI contrast.

The influence of particle morphology on their MRI performance were further investigated with manganese-doped iron oxide (MnIO) particles as models (Fig. 11d).[238] Differently shaped particles, including spheres (with 15 nm diameters), cubes (with edge lengths of 12 nm), hexagonal plates (with side length of 12 nm and thickness of 5 nm), regular tetrahedrons (with side lengths of 25 nm), rhombohedra (oblique parallelepiped, side length of 13.5 nm with a tilt angle of 60°), and octapods (average edge length between two nearby arms of 30 nm and each corner angle of 40°), were prepared. Despite having similar geometric volumes, these particles exhibited significant variations in surface areas. The effective radii of the particles followed a specific order: spheres, cubes, hexagonal plates, tetrahedrons, rhombohedra, and octapods, ranging from 16.36 to 38.94 nm. Additionally, the saturation magnetization showed an increasing trend from spheres to octapods. Consequently, the r_2 values of the particles increased from 201.4 ± 4.6 to 573.5 ± 12.8 mM^{-1} s^{-1} for spheres, cubes, plates, tetrahedrons, rhombohedra, and octapods, respectively. These findings provide further evidence of the significant impact of particle morphology on the MRI performance of magnetic nanoparticles, with non-spherical shapes exhibiting enhanced relaxivity compared to spherical counterparts.

6.1.1.2. 1D or 2D vs spheres. When comparing 1D or 2D structures to spheres, an additional factor that becomes significant is spin canting. This is primarily due to the larger surface-to-volume ratio in 1D or 2D geometries, which results in the increased intrinsic surface disorder area that strongly influences their magnetic properties. In contrast to anisotropic 0D MIPs that typically exhibit larger magnetization values compared to their spherical counterparts, 1D or 2D structures tend to have smaller magnetization values.

For example, M_s values for 50 nm nanorods are 58 emu/g, while for the same volume of nanospheres (16 nm) it is 83 emu/g.[25] However, due to the larger effective radius of the 1D rods, their r_2 values are 427 and 297 mM^{-1} s^{-1}, respectively (Fig. 12a). This discrepancy in r_2 values can be attributed to the outer sphere theory, where the nanorods possess a larger surface area and effective radii compared to the nanospheres. Consequently, under an applied magnetic field, nanorods can generate a larger area of local field inhomogeneity, resulting in higher r_2 relaxivity values. It is noteworthy that as the length of the nanorods increases, the induced local magnetic field strength outside the nanorods also increases. As a result, with an increase of nanorods length from 30 to 70 nm, the r_2 relaxivity value increases linearly from 312 to 608 mM^{-1} s^{-1}.

Highly uniform magnetite nanoplates with flattened hexagonal basal planes have been synthesized *via* thermal decomposition by Gao *et al.*[239] These nanoplates, denoted as IOP-8.8, IOP-4.8, and IOP-2.8, exhibit varying edge lengths and thicknesses of 8.8, 4.8, and 2.8 nm, respectively. According to Hwang and Freed's theory,[240] the r_2 relaxivity value is influenced by two key parameters: the M_s value and the effective radius of the magnetic core, which are both squared. In the case of the nanoplates, their rapid random flipping behaviour in aqueous media allows them to be approximated as simulated spheres or ellipses based on their edge lengths. Notably, the effective radius of a nanoplate is significantly larger than that of a sphere with a similar solid volume. Comparing nanospheres with equivalent solid volumes to IOP-8.8, IOP-4.8, and IOP-2.8, the r_2 values of the nanoplates (ranging from 311.88 ± 7.47 to 78.63 ± 6.41 mM^{-1} s^{-1}) are significantly higher than those of the spherical counterparts (ranging from 232.16 ± 4.91 to 59.38 ± 5.34 mM^{-1} s^{-1}) (Fig. 12b). Additionally, the M_s values of the nanoplates exhibit a decreasing trend with decreasing thickness. The M_s values of IOP-8.8, IOP-4.8, and IOP-2.8 are measured to be 74.1, 57.6, and 34.5 emu/g, respectively. The decrease in M_s values with reduced thickness can be attributed to the more pronounced spin-canting effect of the surface layer in thinner nanoplates.[14,241]

In another study, Gao *et al.* presented a novel type of iron oxide nanoplate (IOP) with a unique twinning plane that was synthesized through seed growth.[146] The synthesized uniform iron oxide twin nanoplates had an edge length of 25.0 nm and a thickness of 13.0 nm (referred to as IOP-13). For comparison, spherical Fe_3O_4 nanoparticles with a diameter of 34.0 nm (referred to as IO-34) were used as a control, as they had a similar material volume. The iron oxide twin nanoplates showed distinct advantages over the conventional iron oxide spherical nanoparticles. They had a larger effective radius, higher saturation magnetization, and greater anisotropy, resulting in significantly higher r_2 relaxivity. The iron oxide twin nanoplates exhibited an r_2 relaxivity of 571.21 mM^{-1} s^{-1}, while the r_2 value for IO-34 was only 161.02 mM^{-1} s^{-1}.

In addition to the comparison of different nanoparticle shapes, research has also investigated the differences between dispersed MIPs and assembled linear MIP chains. Ivanisevic *et al.* coated MIPs with pyrrolidinone and utilized self-assembly of positively charged nanoparticles with negatively charged DNA to synthesize 1D iron oxide chains.[242] The assembled chains showed a significantly higher transverse relaxivity average (r_2 = 78.6 ± 35.0 mM^{-1} s^{-1}) compared to the dispersed NPs (r_2 = 12.2 ± 0.3 mM^{-1} s^{-1}). The enhanced spin–spin relaxation of water protons in the NP chains was attributed to the increased magnetization and NP assembly. Similarly, Zhou *et al.* also reported that assembled 1D hybrid NP chains exhibited much higher MRI contrast compared to dispersed

building block NPs (Fig. 12c).[243] Xiong *et al.* also demonstrated that compared to the dispersed monodisperse sphere MIPs and clustering MIPs, 1D worm-like MIPs achieved better results in T_2-weighted MRI.[135]

It is therefore clear that the structure and shape of iron oxide nanostructures have a significant impact on their r_2 relaxation behavior, primarily due to variations in their M_s, effective radii, and the presence of local inhomogeneous magnetic fields.

6.1.2. T_1 contrast agents

The T_1 relaxation enhancement in T_1 contrast agents occurs due to the energy loss of spin resulting from dipole-dipole interactions between water protons and magnetic ions.[244,245] These interactions take place in three regions: the inner-sphere, secondary or intermediate sphere, and outer sphere. The inner-sphere impact refers to the direct interaction between water protons and magnetic ions, and it predominantly influences the enhancement of T_1 relaxation for T_1 contrast agents.[246] The r_1 value in the inner sphere is given by:[247]

$$R_1 = qP_m[1/(T_{1m} + \tau_m)] \tag{4}$$

$$\frac{1}{\tau_m} = \frac{2}{15} \bullet \frac{\gamma^2 g^2 S(S+1)\mu_B{}^2}{r^6} \left(\frac{3\tau_{c1}}{1+\omega^2{}_H\tau^2{}_{c1}} + \frac{7\tau_{c2}}{1+\omega^2{}_H\tau^2{}_{c2}} \right) \tag{5}$$

$$1/\tau_{ci} = 1/\tau_r + 1/\tau_{is} + 1/\tau_m \tag{6}$$

$$\tau_r = \frac{4\pi\eta a^3}{3kT}$$

where a, η, k, and T are hydrodynamic radius of the nanoparticles, viscosity, Boltzman constant, and temperature, respectively. P_m

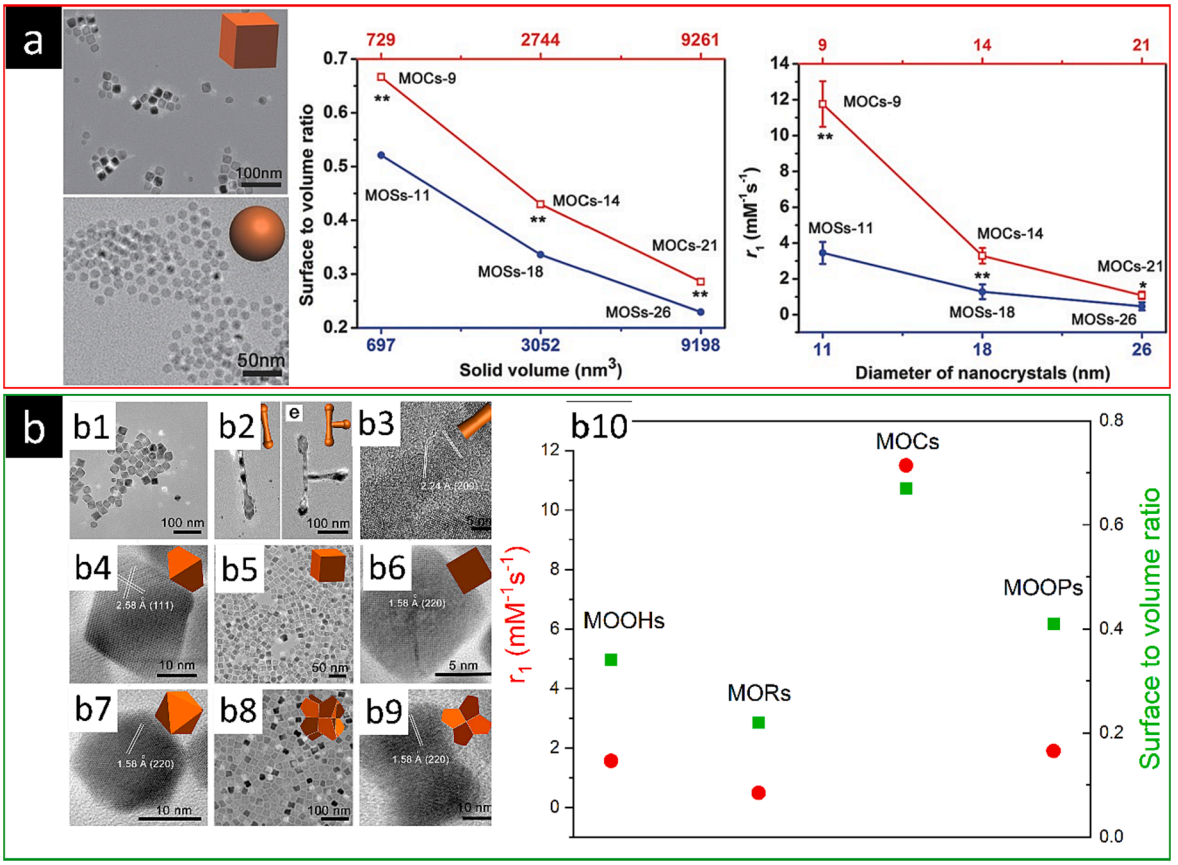

Fig. 13. (a). Left panel: Representative TEM images of manganese oxide nanocubes (MOCs) (top left) and manganese oxide spheres (MOSs) (bottom left). The comparisons of (middle panel) surface-to-volume ratio and (right panel) T_1 relaxivity of MOCs and MOSs containing a similar amount of manganese ions. Adapted with permission from ref.[189], copyright 2017 Wiley-VCH. (b) TEM images of monodispersed manganese oxide (MO) nanoparticles (b1) nanooctahedrons (MOOHs), (b2) nanorods (MORs), (b5) nanocubes (MOCs), and (b8) nanooctapods (MOOPs), respectively. HRTEM images of (b4, b7) MOOHs, (b3) MORs, (b6) MOCs, and (b9) MOOPs, respectively. Insets show the geometric model. (b10) The comparisons of surface-to-volume ratio and T_1 relaxivity of MOOHs, MORs, MOCs and MOOPs. Adapted with permission from ref.[252], copyright 2017 American Chemical Society.

is the mole fraction of water coordinating to the metal tracer, T_{1m} is the applicable dipole–dipole relaxation, q is the coordination number of water, τ_m is proton residence lifetime, τ_{ci} is the correlation time, τ_r is the molecular tumbling time, r is the distance between the magnetic ions and protons, and τ_{is} is the electronic relaxation time.

T1 CAs are usually dominated by paramagnetic, for example Gd^{3+} chelates, however MIPs can also be considered as T_1 CAs given certain characteristics. An ideal T1 contrast agent (CA) should possess a large coordination number (q), short proton residence lifetime (τ_m), long molecular tumbling time (τ_r), long electronic relaxation time (τ_s), and a low r_2/r_1 ratio to achieve high T_1 relaxivity. Therefore, (1) to achieve a low r_2 value and consequently reduce the r_2/r_1 ratio, one approach is to decrease the M_s. This can be accomplished by reducing the size of MIPs, which increases the surface spin canting area, leading to decreased r_2 values, as previously described. (2) Alternatively, an increase in the surface-to-volume ratio can elevate the surface area, allowing for a greater number of ions on the surface to be exposed to water. This, in turn, increases the coordination number of water (q). (3) Lastly, a higher T_1 performance can be achieved by increasing the molecular tumbling time τ_r. [248] To achieve long τ_r, MIPs with larger hydrodynamic radius are preferred. While as we discussed in the previous section regarding T_2 contrast agent, non-spherical MIPs possess a larger surface-to-volume ratio, meeting the first two criteria. Furthermore, the non-spherical shape of MIPs contributes to a larger effective hydrodynamic radius. Due to their irregular shape and extended dimensions, non-spherical MIPs experience slower rotational motion, which results in a longer molecular tumbling time τ_r.

In the first approach mentioned earlier, reducing the size of MIPs has been shown to enhance T_1 MR imaging capability. Ultrasmall iron oxide nanoparticles with a diameter smaller than 5 nm have been studied and proven effective in enhancing T_1 contrast in MR imaging.[28,92,249–251] However, it is important to note that synthesizing anisotropic non-spherical MIPs at such small sizes is more challenging compared to spherical ones. As a result, there is currently no available report directly comparing spherical and non-spherical particles for T_1 enhancement using MIPs. Nonetheless, it is worth mentioning that in this context, manganese and gadolinium exhibit advantages over iron. Manganese/gadolinium oxide nanoparticles with different shapes provide a valuable tool for

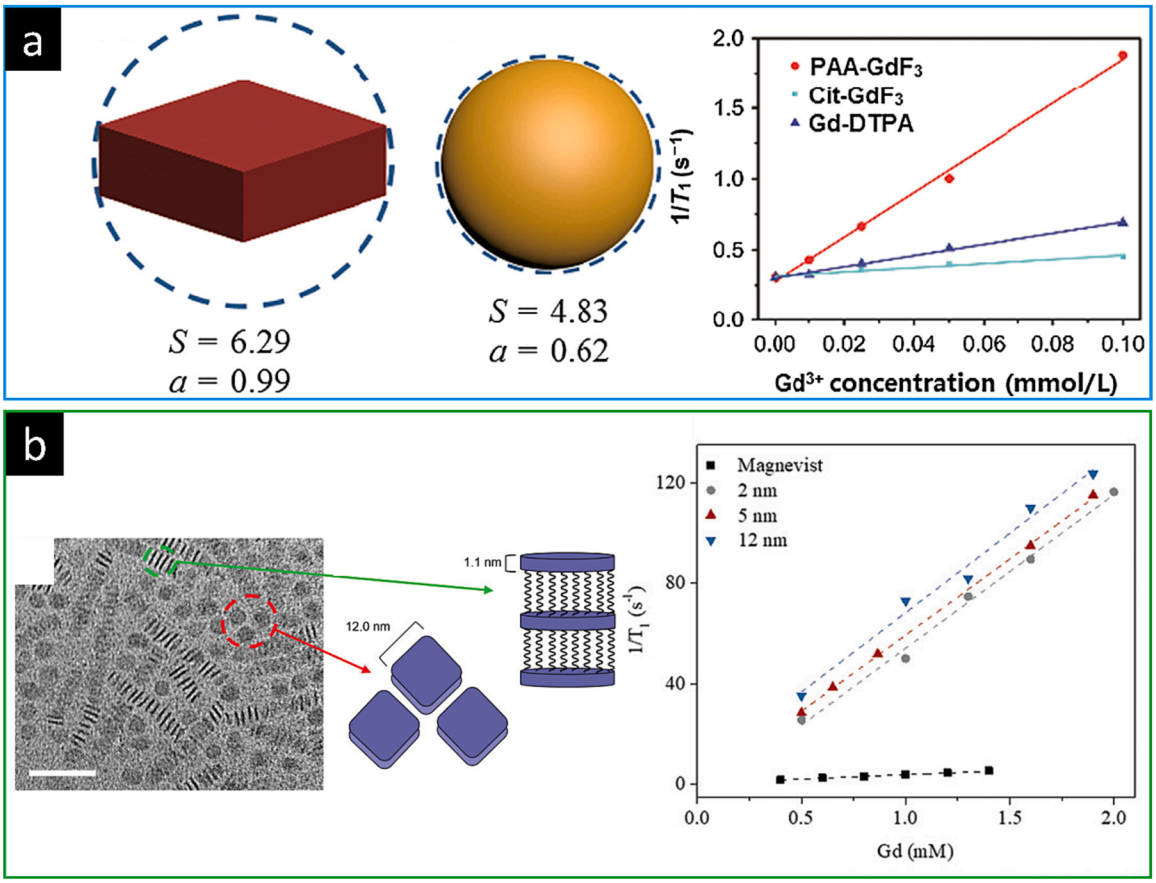

Fig. 14. (a) Schematic of geometry models of 2D plate (left panel) and sphere nanoparticles (middle panel). The blue dash circle represents hydrodynamic equivalent sphere. The volumes of two models were normalized. Right panel: T_1 relaxivity plot of GdF_3 nanoplates and Gd-DTPA. Adapted with permission from ref.[27], copyright 2015 Elsevier. (b) Left panel: TEM image of as-synthesized gadolinium oxide nanoplates (GONP) sample (scale bar = 50 nm). Middle panel: diagram depicting edge-to-edge (red) and face-to-face (orange) alignment of GONP on the TEM grid. Right panel: Longitudinal relaxation rates as a function of gadolinium concentration for poly (2-acrylamido-2-methylpropane sulfonic acid-lauryl acrylate)-GONP (with edge size 2, 5, and 12 nm) compared to Magnevist at 1.4 T. Adapted with permission from ref.[254], copyright 2021 Wiley-VCH. (For interpretation of the references to color in this figure legend, the reader is referred to the web version of this article.)

investigating the correlation between nanoparticle morphology and T_1-weighted MRI performance. These aspects will be further discussed and compared in subsequent sections.

6.1.2.1. Non-spherical 0D vs spheres. Zhao *et al.* prepared manganese oxide nanocubes (MOCs) by thermal decomposition of manganese-oleate in the presence of oleic acid, sodium chloride, and 1-octadecene.[189] These MOCs exhibited highly crystalline surfaces and uniform shapes, making them ideal models for investigating the impact of shape-induced differences in MRI. The edge length of the MOCs was adjusted by varying the reflux time, resulting in three representative types of MOCs with average edge lengths of 9.3 nm, 14.7 nm, and 21.4 nm, denoted as MOCs-9, MOCs-14, and MOCs-21, respectively. For comparison, manganese oxide nanospheres (MOSs) with mean diameters of 11 nm, 18 nm, and 26 nm, denoted as MOSs-11, MOSs-18, and MOSs-26, were used due to their similar manganese ion content.

The MOSs-11, MOSs-18, and MOSs-26 exhibited T_1 relaxivities of 3.45 mM^{-1} s^{-1}, 1.28 mM^{-1} s^{-1}, and 0.47 mM^{-1} s^{-1}, respectively. Impressively, the MOCs demonstrated significantly stronger T1 contrast effects compared to the MOSs. The r_1 values of MOCs-9, MOCs-14, and MOCs-21 were 11.76 mM^{-1} s^{-1}, 3.29 mM^{-1} s^{-1}, and 1.08 mM^{-1} s^{-1}, respectively, which were approximately 3.41, 2.57, and 2.30 times higher than their corresponding MOSs (Fig. 13a). The higher r_1 values observed in MOCs can be attributed to their high surface-to-volume ratio, which allows for a larger number of exposed manganese ions on the surface and accelerates the spin relaxation process of water protons. Additionally, an interesting trend was observed, where the r_1 values of both MOCs and MOSs gradually decreased with increasing sizes. This inverse correlation provides further evidence that a high surface-to-volume ratio is advantageous in elevating T_1 relaxivity values.

In another study by Zhao *et al.*, the researchers conducted a systematic comparison of structure-dependent T_1 relaxivity using different shaped nanoparticles, including 0D nano octahedrons, cubes, octopods, and 1D nanorods (Fig. 13b).[252] The results showed a clear reduction in T_1 relaxation as the surface-to-volume ratio decreased. The cubes, octopods, octahedrons, and rods exhibited T_1 relaxivity values of 11.50 mM^{-1} s^{-1}, 1.89 mM^{-1} s^{-1}, 1.56 mM^{-1} s^{-1}1, and 0.48 mM^{-1} s^{-1}, respectively. These findings are consistent with the theoretical understanding that the surface-to-volume ratio primarily determines the number of exposed paramagnetic ions on the nanoparticle surface, thereby influencing the capacity for T_1 relaxation enhancement.

6.1.2.2. 1D or 2D vs spheres. Yeh *et al.* prepared water dispersible Mn_3O_4 nanoparticles with various morphologies as MRI contrast agents.[253] They found that compared to Mn_3O_4 0D nanospheres (~9.8 nm in diameter) although 2D Mn_3O_4 nanoplates (~ 10 nm in length) have similar effective radii of nanoparticles and smaller geometric volumes, the r_1 relaxivity of the 2D nanoplate is 2.06 mM^{-1} s^{-1} while it is 1.31 mM^{-1} s^{-1} for 0D nanospheres. The larger relaxivity of the nanoplates is very likely caused by a larger surface-to volume ratio, giving greater accessibility and interaction between the water molecules and the nanoplates, coupled with longer rotational correlation times than spherical equivalents of the same volume.

In another study by Yan *et al.*, GdF_3 rhombic nanoplates were synthesized through thermolysis reactions, with average dimensions of long diagonal, short diagonal, and thickness measuring approximately 10.6 ± 1.1 nm, 7.0 ± 0.8 nm, and 4.2 ± 1.2 nm, respectively (Fig. 14a).[27] Notably, to facilitate a straightforward comparison between the types of nanoplates, the sizes of the plate numerical model were adjusted to be proportional to the dimensions of GdF_3 nanoparticles, while ensuring that the volumes of all models were normalized to 1. After converting the hydrophobic nanoplates to hydrophilic through ligand exchange with polyacrylic acid (PAA), the r_1 relaxivity of PAA-capped nanoplates reaches up to 15.8 (L/mmol s) and the r_2/r_1 ratio is 1.3. In contrast, after ligand exchanged with citric acid, recrystallization happened and the nanoplates were reshaped into spheres and their r_1 relaxivity is 1.5 (L/mmol s). After numerical calculation, compared with the spheres with same volumetric value (normalized as 1), the surface-to-volume ratio (S/V) of nanoplates and spheres are 6.24 and 4.83, respectively. Moreover, the hydrodynamic size for the nanoplates and nanospheres are 0.99 and 0.62, respectively. Therefore, based on the comparison between the 2D plate structure and the 0D sphere, the 2D plate structure exhibits superiority in both in S/V and τ_r. The authors proposed that further reducing of thickness of the 2D nanoplates would result in an increased S/V, ultimately leading to higher r_1 values.

In a study by Gao *et al.*, iron oxide nanoplates with thicknesses of 8.8 nm (IOP-8.8), 4.8 nm (IOP-4.8), and 2.8 nm (IOP-2.8) were synthesized and compared to their spherical counterparts.[239] After functionalizing the particles with *meso*-2,3-dimercaptosuccinic acid to make them hydrophilic, their MRI performance was evaluated and compared with iron oxide spheres of equivalent surface areas, with diameters of 26 nm, 21 nm, and 16 nm. The r_1 relaxivity values of IOP-8.8, IOP-4.8, and IOP-2.8 were found to be 38.11 ± 1.04 mM^{-1} s^{-1}, 43.18 ± 3.33 mM^{-1} s^{-1} 1, and 14.36 ± 1.24 mM^{-1} s^{-1}, respectively. In comparison, the corresponding r_1 values of the nanospheres decreased with decreasing diameter, measuring 16.49 ± 2.87 mM^{-1} s^{-1}, 11.73 ± 0.24 mM^{-1} s^{-1}, and 7.67 ± 1.05 mM^{-1} s^{-1}. The superior performance of the nanoplates suggests that there are more exposed iron ions on their surfaces, attributed to their larger surface-to-volume ratio. However, it is important to note that the r_1 value of IOP-2.8 (14.36 ± 1.24 mM^{-1} s^{-1}) exhibited a significant reduction compared to IOP-8.8 and IOP-4.8. This decrease may be attributed to spin disorder occurring at the corners of the ultrathin nanoplates. The presence of disordered metal atoms at the spin-canted corners can hinder the effective coordination and chemical exchange process of protons, resulting in a reduced number of exposed metal centers on the surface and weakened T_1 contrast ability. Overall, the study demonstrates that iron oxide nanoplates with larger surface-to-volume ratios can exhibit enhanced T_1 relaxivity compared to spherical counterparts. However, when the thickness of the nanoplates is reduced to a certain extent, spin disorder at the corners can have a detrimental effect on the T_1 contrast ability.

However, conducting a systematic investigation solely focusing on the effects of shape on MRI performance can be challenging. In order to isolate the influence of shape, it is necessary for the ideal geometric pairs to be identical in terms of other parameters such as composition, surface coating, and crystalline structures. Of course, in practice, achieving such precise control over all parameters of

non-spherical particles can be complex and challenging. For instance, in a study by Colvin and co-workers, a series of 2D gadolinium oxide nanoplates with varying face lengths ranging from 6 to 15 nm and an edge width (thickness) of 1.1 nm were prepared through a thermal decomposition reaction (Fig. 14b).[254] Surprisingly, they observed that the large dimensions of the nanoplates had little impact on their r_1 relaxivity. This contradictory and weak size dependence is likely attributed to vacant edges. As the size of the nanoplates increases, the number of gadolinium ions on the surface available for facilitating water proton relaxation per unit volume of the contrast agent decreases. This research highlights the complexity involved in isolating the sole influence of shape on MRI contrast enhancement and emphasizes the importance of considering other parameters and factors in addition to shape when studying the MRI performance of nanomaterials.

6.2. *Magnetic particle imaging (MPI)*

MRI, despite its advantages of high spatial resolution and depth penetration, has some limitations. T_2-weighted MRI contrast agents can produce a dark signal that may be indistinguishable from intrinsic hypointense regions like hemorrhage, bones, and lungs. Additionally, the sensitivity of T_1-weighted MRI for molecular imaging is currently limited by the performance of existing T_1 contrast agents, some of which raise safety concerns due to the potential leaching of toxic ions, as seen with gadolinium-based agents.[255,256] In recent years, magnetic particle imaging (MPI) has emerged as a promising imaging modality that is rapidly gaining attention.[183,257] MPI directly visualizes the spatial distribution of magnetic nanoparticles by detecting the signals generated from the nonlinear magnetization of these nanoparticles.[258] MPI offers several advantages, including being irradiation-free, high signal-to-noise ratio (SNR), zero signal attenuation, and potentially high sensitivity. These features make MPI an ideal platform for *in vivo* tracking of various species, such as stem cells, due to its ability to provide real-time imaging and enhanced sensitivity compared to traditional MRI techniques.[259]

MPI relies on the nonlinearity of the magnetization curves of ferromagnetic materials. It takes advantage of the fact that the magnetization of magnetic nanoparticles saturates at a specific magnetic field strength. By applying an oscillating drive field $H_D(t)$ with sufficient amplitude, the particles exhibit a magnetization response $M(t)$ that contains higher harmonics compared to the drive

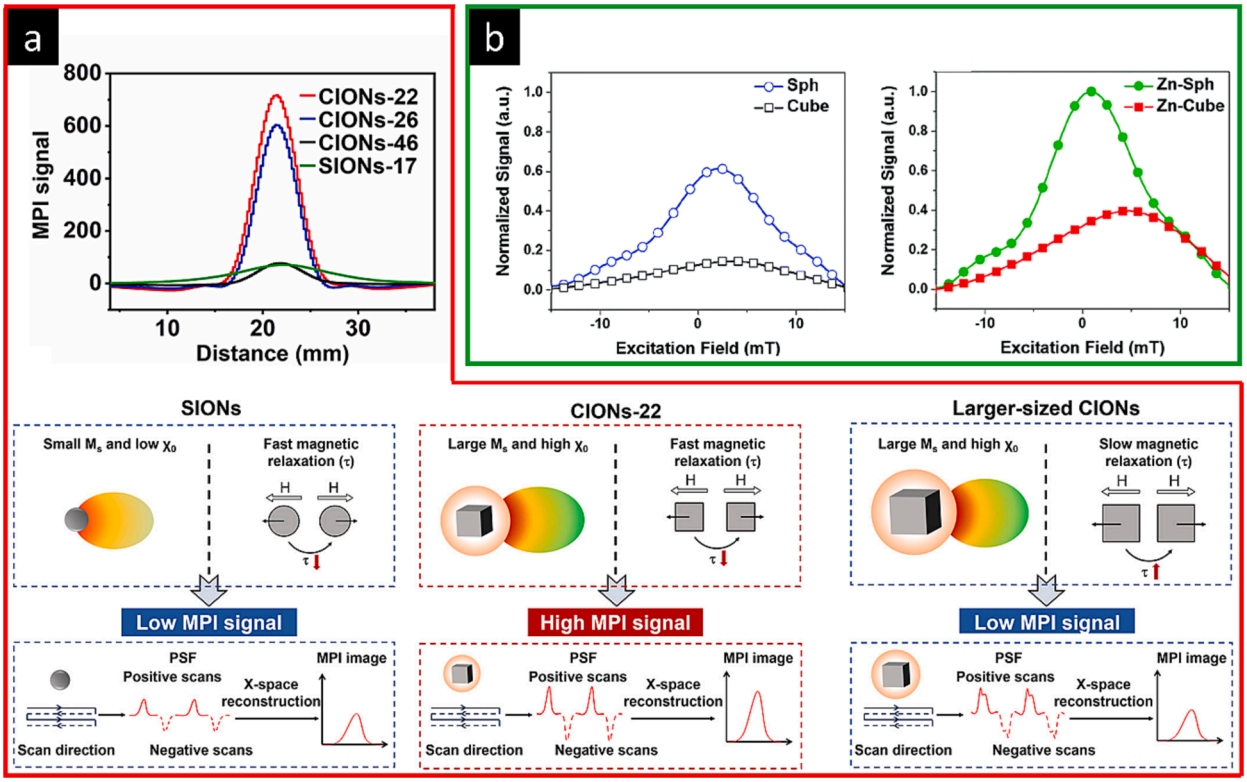

Fig. 15. (a) Top panel: MPI performance of spherical iron oxide nanoparticles with diameter of 16.7 ± 1.5 nm (SIONs-17) and different sized cubic iron oxide nanoparticles (CIONs) with the same Fe concentration of 1.7 mM. Bottom panel: schematic illustrating that CIONs-22 exhibit better MPI performance than SIONs or larger-sized counterparts due to their large M_s, high $\chi 0$, and fast magnetic relaxation. adapted with permission from ref.[266], copyright 2020 American Chemical Society. (b) Left panel: the normalized point spread functions (PSFs) for the magnetite spherical nanoparticles (Fe_3O_4, Sph) and cubic NPs (Fe_3O_4, Cube). Right panel: the normalized PSFs for the zinc-doped magnetite spherical nanoparticles ($Zn_{0.4}Fe_{2.6}O_4$, Zn-Sph), and cubic nanoparticles ($Zn_{0.4}Fe_{2.6}O_4$, Zn-Cube). Adapted with permission from ref.[268], copyright 2016 Royal Society of Chemistry.

field.[257] In MPI, a time constant magnetic field with a significant magnitude is combined with a weak magnetic modulation field. This creates a time-dependent field-free point (FFP) where magnetic particles experience minimal magnetic field influence. Magnetic particles located at the FFP produce a distinct signal that contains higher harmonics. By mapping the magnitude of these harmonics, an image of the magnetic tracer distribution can be obtained. Compared to MRI, MPI promises a higher temporal resolution with high acquisition rates, allowing for a higher signal-to-noise ratio (SNR).[260]

Rahmer proposed that the magnetization of the particles obeys the Langevin theory,[261]

$$M(\xi) = M_o(coth\xi - 1/\xi) \tag{7}$$

Where M_o is the saturation magnetization and ξ is the ratio between magnetic energy of a particle with magnetic moment m in an external field H, and thermal energy given by the Boltzmann constant k_B and temperature T:

$$\xi = \frac{\mu_0 mH}{k_B T} \tag{8}$$

Where μ_0 is the magnetic permeability of vacuum. A higher magnetic moment results in a steeper magnetization curve and creates higher harmonics for a given drive field amplitude. The spatial resolution is given by

$$\Delta x = \frac{k_B T}{\mu_0 mG} \Delta\xi_{FWHM} \tag{9}$$

Where m is the particle magnetization, G is the selection field gradient strength, $\Delta\xi_{FWHM}$ is the full width at half maximum (FWHM) of Langevin curve. The particle magnetization depends on particle diameter d according to the following relation:

$$m = \frac{\pi}{6} M_s d^3 \tag{10}$$

Therefore, both saturation magnetization M_s and particle diameter d play crucial roles in achieving high spatial resolution. A high Ms allows for a stronger magnetization response, leading to better signal detection. Furthermore, the steep slope (dM/dH) on their magnetization-applied field (M−H) curve is important for MPI tracers[262,263]. Importantly, the slope is related to the inherent magnetic properties of the MPI tracer, including saturation magnetization (M_s), magnetic susceptibility (χ), magnetic relaxation time (τ), and coercivity (H_c).[258,264,265]

6.2.1. Non-spherical shapes vs spheres

The shape and structural anisotropy of magnetic nanoparticles can be utilized to tune their properties and enhance their performance in magnetic particle imaging (MPI), although research in this area is still in its early stages. Ling *et al.* conducted a study where they prepared uniform cubic iron oxide nanoparticles (CION) with sharp edges and varying edge lengths (CIONs-22, CIONs-26, CIONs-46) as well as spherical iron oxide nanoparticles (SIONs) with different diameters (SIONs-17, SIONs-22).[266] The results of their study showed that CIONs-22, despite having a similar saturation magnetization (M_s) compared to larger-sized CIONs, exhibited a smaller coercivity (Hc) and a steeper slope (larger dM/dH value) on the magnetization-applied field (M−H) curve (Fig. 15a). It is known that the coercivity and remnant magnetization of single-domain magnetic nanoparticles increase with increasing size.[267] Therefore, CIONs-22 with a smaller size are more favorable for achieving a steeper slope. Additionally, CIONs-22 outperformed SIONs in terms of their MPI signal due to their higher M_s values. This is attributed to the inherent higher portion of disordered spins on the surface of the cubic nanoparticles, which is a result of their anisotropic shape.[14] The presence of these disordered spins contributes to a higher M_s and consequently a stronger MPI signal compared to SIONs or larger-sized CIONs at the same iron concentration.

However, another study reported by Samia *et al.* reported a controversial shape effect on the MPI performance of MIPs.[268] In their research, they prepared spherical nanoparticles with a diameter of 19.2 ± 1.3 nm and cubic nanoparticles with an edge length of 15.5 ± 1.1 nm, ensuring both particle types had equal volumes. Surprisingly, despite both particle shapes exhibiting high and similar saturation magnetization (101.5 emu/g Fe for spheres and 107.3 emu/g Fe for cubes), the spherical nanoparticles outperformed the cubic nanoparticles in terms of MPI performance (Fig. 15b). This phenomenon was attributed, at least in part, to the greater propensity of magnetic cubic nanoparticles to spontaneously assemble into chains.[142,269,270] This chain formation may affect the response of the particles to the applied magnetic fields in MPI and result in a less efficient signal generation.

To further investigate the influence of saturation magnetization, the researchers doped the nanoparticles with zinc, which increased the M_s value compared to the undoped particles. As expected, with the shape unchanged, the increase in M_s (125.7 emu/g Fe for spheres and 130.4 emu/g Fe for cubes after doping) led to enhanced MPI performance albeit with the spheres still outperforming the cubes. The results showed that the zinc-doped spherical MIPs exhibited a 2-fold increase in signal-to-noise ratio (SNR) and a 10 % smaller full width at half maximum (FWHM) compared to the undoped sample. In the case of the cubic MIPs, the enhancement in SNR was even more pronounced, with approximately a 3-fold increase for the zinc-doped cubes compared to the undoped cubic sample.

Overall, these findings suggest that the shape effect on MPI performance can be complex and multifaceted. While the cubic shape of the nanoparticles may have advantages in certain scenarios, such as higher inherent saturation magnetization, the propensity for chain formation can hinder their performance in MPI. Nonetheless, doping the particles to increase their saturation magnetization can effectively enhance the MPI signal, regardless of the particle shape.

The development of MPI tracers is still in its early stages, and much of the research has focused on studying the effects of nanoparticle size on MPI sensitivity and resolution enhancement. Most of the investigated MPI tracers have been based on spherical

particles, which provide a good starting point for understanding the basic principles of MPI. However, there is a need for further optimization and exploration of non-spherical magnetic nanoparticles to enhance their MPI performance.[265,271]

6.3. Photothermia

Photothermal therapy is a technique used to destroy abnormal cells by increasing their temperature through light-induced thermal ablation. Laser-induced photothermal ablation is commonly employed because human tissues have strong absorption coefficients in the visible range of the electromagnetic spectrum. To enhance the efficacy and selectivity of laser-induced photothermal ablation, light-absorbing materials known as photothermal agents (PA) can be introduced. Traditionally, noble metal nanoparticles, particularly gold nanoparticles, have been extensively used as photothermal agents due to their well-developed synthesis methods and strong light absorption properties. However, gold nanoparticles are non-biodegradable, which limits their long-term applications in biological systems.

More recently, spherical MIPs have also emerged as potential photothermal agents.[272] These MIPs offer advantages such as biodegradability and the ability to tune their properties through precise synthesis techniques. Researchers have investigated the photothermal effect of monodisperse iron oxide particles with varying sizes. For example, Guo *et al.* conducted a study where they synthesized monodisperse iron oxide particles with sizes ranging from 10 to 310 nm. They observed that the photothermal effect increased with the size of the particles, indicating a size-dependent heating capability for photothermal therapy.[273,274] Sun *et al.* prepared highly crystallized spherical iron oxide nanoparticles as effective and biodegradable mediators for photothermal cancer therapy.[275] These nanoparticles exhibited a uniform shape and size distribution, with an average diameter of 15 nm. In their experiments, a nanocrystal solution containing these iron oxide nanoparticles at a concentration of 0.5 mg mL^{-1} Fe was exposed to an 885 nm diode laser with a power of 2.5 W/cm^2. As a result, the temperature increased by 33 °C from room temperature. In contrast, the control sample of water showed only a temperature increase of approximately 3 °C under the same laser conditions. This significant temperature increase in the presence of iron oxide nanoparticles demonstrates their strong photothermal effect, which can be harnessed for effective cancer therapy. These studies highlight the potential of iron oxide nanoparticles, both in terms of size-dependent photothermal performance and their biodegradability, making them promising candidates for photothermal therapy in the treatment of cancer and other diseases.

The photothermal conversion efficiency of a material is expressed as:[276]

$$\hat{\mathrm{I}}\cdot = \frac{hS(T_{max} - T_{amb}) - Q_s}{I(1 - 10^{-A})} \tag{11}$$

where h is the heat transfer coefficient, S is the surface area of the container, T_{max} is the maximum equilibrium temperature, T_{amb} is the ambient temperature of the surroundings, I is the laser power, a is the absorbance of PA at emission wavelength of the laser, and Q_s is the heat associated with the absorbance of the solvent.

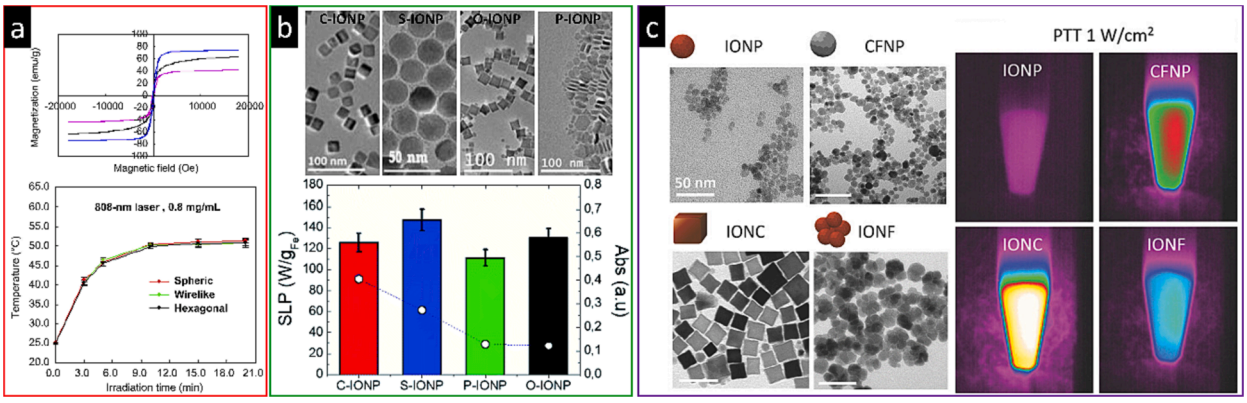

Fig. 16. (a) Top panel: magnetization of hexagonal, spherical, and wire-like nanoparticles (M_s values from high to low, respectively). Bottom panel: temperature vs. irradiation time of the aqueous suspensions of Fe_3O_4 nanoparticles with spherical, hexagonal, and wire-like shapes at a concentration of 0.8 mg/mL. Irradiation was carried out with 808 nm lasers. Adapted with permission from ref.[279], copyright 2013 Elsevier. (b). Top panel: TEM images of iron oxide nanoparticles (IONPs) with different shapes. From left to right: spheres (S-IONP), cubes (C-IONP), platelets (P-IONP) and octopods (O-IONP). Bottom panel: Optical specific loss power (SLP) (bars) and absorbance (empty dots) values at 808 nm for different shape IONPs. Irradiation conditions: 808 nm, 0.3 W cm^{-1}. IONPs were dispersed in double distilled water at [Fe] = 1 g/L. Adapted with permission from ref.[280], copy right 2021 Royal Society of Chemistry. (c) Left panel: TEM images of magnetic nanomaterials: iron oxide nanoparticles (IONP, 9 nm), cobalt ferrite nanoparticles (CFNP, 11 nm), iron oxide nanocubes (IONC, 20 nm), and iron oxide nanoflowers (IONF, 25 nm). Scale bar = 50 nm. Right panel: Infrared thermal images of magnetic nanomaterials (IONP: 9 nm, CFNP: 11 nm, IONC: 20 nm, and IONF: 25 nm) after 1 min of laser irradiation at 808 nm and 1 W cm^{-2} (PTT). Adapted with permission from ref.[281], copyright 2018 Wiley-VCH.

6.3.1. Non-spherical shapes vs spheres

In the context of photothermal therapies, the shape of nanoparticles plays a crucial role in their photothermal performance. While plasmonic nanoparticles, such as gold nanoparticles, have been extensively studied for their photothermal properties,[277,278] the investigation of shape-anisotropic MIPs in this regard is relatively limited.

Chu *et al.* conducted a study to examine the impact of particle shape on the photothermal effect of iron oxide particles.[279] They synthesized three types of particles: spherical nanoparticles with a diameter of 9.1 ± 1.9 nm, hexagonal particles with a size of 9.4 ± 1.3 nm, and wire-like nanoparticles with a diameter of 12.6 ± 5.9 nm and a length of several hundred nanometers. Interestingly, all three types of particles exhibited effective photothermal performance. For instance, at a concentration of only 0.08 mg/mL of spherical Fe_3O_4 nanoparticles, the suspension experienced a temperature increase of over 13 °C after 10 min of irradiation with an 808 nm laser. Control experiments using distilled water subjected to laser irradiation at different wavelengths (655 nm, 671 nm, and 808 nm) resulted in temperature increases of no more than 6.7 °C after 20 min of irradiation.

Notably, the photothermal conversion effects of hexagonal and wire-like Fe_3O_4 nanoparticle suspensions upon 808 nm laser irradiation were found to be similar to those of the spherical Fe_3O_4 particles (Fig. 16a). This similarity in performance was attributed to their comparable absorptions at the 808 nm wavelength, suggesting that the anisotropic shape of the particles had minimal influence on the photothermal effect in this particular study. In another study by Teran *et al.*, iron oxide nanoparticles in various shapes including platelets, nanocubes, octopods, and spheres were prepared, and it was again observed that the nanoparticle shape had no significant influence on the photothermal behaviour when compared to other intrinsic features of MIPs such as size, crystallinity, and iron oxidation state (Fig. 16b).[280]

In contrast to those previous studies, Espinosa *et al.* found that magnetite nanocubes exhibited higher photothermal ability compared to iron oxide nanospheres and cobalt ferrite nanospheres (Fig. 16c).[281] The magnetite nanocubes had a size of 20 nm and a M_s of 75.3 emu/g, while the iron oxide nanospheres were 9 nm in size with an M_s of 53.8 emu/g, and the cobalt ferrite nanospheres had a size of 11 nm and an M_s of 61.3 emu/g. It is important to consider that the anisotropic particle pairs in each study were prepared using different approaches, which could introduce variations in their properties. To accurately assess the shape effect on the photothermal effect, it is crucial to use uniform non-spherical MIPs with comparable sizes (volume or surface area) that are prepared using the same methods. Further research in this area is necessary to gain a better understanding of the impact of particle shape on photothermal performance.

6.4. Hyperthermia

In the presence of an alternating current (AC) magnetic field, MIP undergo magnetization reversals, resulting in the dissipation of magnetic energy, known as hyperthermia. This process can be characterized by two relaxation mechanisms: Néel relaxation (with relaxation time τ_N) and Brownian rotation (with relaxation time τ_B)[282]:

$$\tau_{\mathrm{N}} = \tau_0 \exp\left(\frac{\mathrm{K_{eff}V}}{\mathrm{k_BT}}\right) \tag{12}$$

$$\tau_{\mathrm{B}} = \frac{3\eta \mathrm{V_H}}{\mathrm{k_BT}} \tag{13}$$

where τ_0 is the attempted relaxation time of 10^{-9} s. The Néel relaxation is determined by the anisotropy energy ($K_{eff}V$) of the MIPs. The anisotropy energy is influenced by factors such as the size, shape, and magnetic properties of the nanoparticles. On the other hand, the Brownian rotation relies on the hydrodynamic volume of the nanoparticles (V_H) and the viscosity of the dispersing medium (η). If Néel relaxation and Brownian rotation occur in parallel, the effective relaxation time τ is given by [283]

$$\tau = \frac{\tau_{\mathrm{N}}\tau_{\mathrm{B}}}{\tau_{\mathrm{N}} + \tau_{\mathrm{B}}} \tag{14}$$

and the heat dissipation (P) associated with the lost magnetic energy during the magnetization reversal process can be expressed as [283,284]:

$$P = f \times A = \mu_0 \pi H_{ac}^2 f X'' \tag{15}$$

in which f is the frequency of the alternating magnetic field (AMF), A is the hysteresis loop area caused by AMF, μ_0 is the permeability of free space (a constant value), H_{ac} is the applied magnetic field strength, and the loss component of susceptibility X'' can be further expressed as

$$X'' = X_0\left[\omega\tau/(1+\omega\tau)^2\right] \tag{16}$$

Where X_0 is the static susceptibility,[285]

$$X_0 = \frac{M_s^2 V}{3k_B T} \tag{17}$$

Where M_s is the saturation magnetization and V is the magnetic volume of the MIPs.

Based on the equations given above, higher M_s, larger V and larger τ, hence Néel relaxation (τ_N) and Brownian rotation (τ_B) are favorable to increase heat dissipation P. Since τ_N and τ_B are determined by anisotropy energy and hydrodynamic size, respectively, anisotropic non-spherical nanoparticles with higher anisotropy energy tend to have longer relaxation times, which can enhance heat dissipation.

To quantitively describe the amount of heat generated by MIPs, the specific absorption rate (SAR) is used. The SAR is determined by several factors and can be calculated using the following equation:[286]

$$SAR = \frac{C}{m}\left(\frac{dT}{dt}\right) \tag{18}$$

where C is the specific heat of the colloid (*i.e.*, for water, this value is 4.18 J g^{-1} °C), dT/dt represents the initial slope of the temperature versus time graph, indicating the rate of temperature increase, and m is the mass of magnetic material in the suspension (in mg/mL). To summarize, apart from the applied AC magnetic field amplitude and frequency, SAR also depends on several other factors, including M_S, size, shape, concentration, and effective anisotropy of the nanoparticles.

6.4.1. Non-spherical 0D vs spheres

Anisotropic 0D particles, such as nanocubes, have been extensively studied and shown to be more efficient in hyperthermia compared to spherical particles. Multiple examples have demonstrated the superior performance of magnetic nanocubes over spheres.[287] For example, Samia *et al.* conducted a study where they prepared magnetite nanoparticles in both spherical and cubic shapes with equivalent volumes for direct comparison.[268] The SAR values of the synthesized spherical and cubic samples were found to be 189.6 and 356.2 W/g, respectively, under specific conditions ($f_m = 380$ kHz and $H_{max} = 16$ kA/m). It is worth noting that the saturation magnetization (M_s) values for both samples were very close, with 101.5 emu/g for the spheres and 107.3 emu/g for the cubes. This indicates that the high SAR value observed in the cubic particles is primarily due to the shape anisotropy, highlighting the enhanced heating efficiency conferred by the cubic shape.

Additional studies have provided evidence supporting the superior magnetic heating efficiency of cubic nanoparticles compared to spherical particles. Baldomir *et al.* conducted a study where they investigated ferrimagnetic nanocubes with an edge length of

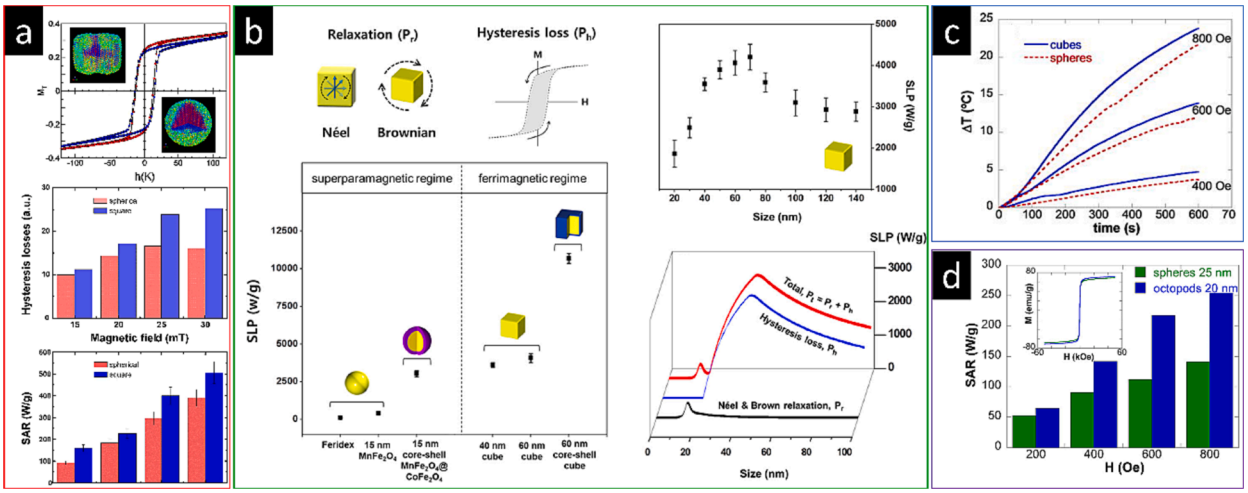

Fig. 17. (a) Top panel: Hysteresis loops for a spherical (red circles, diameter 20 nm) and a cubic particle (blue squares, side 20 nm) obtained from Monte Carlo (MC) simulations of an atomistic spin model of maghemite at low temperature. The simulation results indicate that the area of the hysteresis loop of the cubic particle is bigger than that of the spherical particle. Middle panel: MC simulations for the macrospin model with dipolar interactions at 300 K. Bottom panel: SAR values for two nanoparticle solutions of similar concentration (0.5 mg/mL) and size volume but different shape. Adapted with permission from ref.[33], copyright 2013 Nature Portfolio. (b) Heat emission processes and observed specific loss power (SLP) of magnetic nanoparticles. Top left: schematic representation of the major mechanisms for heat dissipation of magnetic nanoparticles in response to an alternative magnetic field (AMF). Magnetic spin rotation (Néel) and particle rotation (Brownian) processes in the superparamagnetic regime and hysteresis loss for ferrimagnetic regime. Top right: Measured SLPs of various sized cubes. The 70 nm cube has the highest SLP value (4206 W/g) with the maximized hysteresis loss. Bottom right: calculated SLP vs nanoparticle size. Black line: Contribution of relaxation loss (Pr) including Néel and Brownian relaxation; blue line: contribution of hysteresis loss (Ph); red line: summation of relaxation loss (Pr) and hysteresis loss (Ph). Bottom left: summarized SLP values of various nanoparticles. For sphere and cube, core–shell nanoparticles have higher SLP values than those of single component nanoparticles in both the superparamagnetic and ferrimagnetic regimes. Among them, 60 nm CS-cube has the highest SLP of 10600 W/g. Standard deviation are represented as error bars. Adapted with permission from ref.[14], copyright 2012 American Chemical Society. (c) Heating curves for the spheres and cubes measured at 310 kHz and H = 400–800 Oe. Adapted with permission from ref.[288], copyright 2015 AIP Publishing LLC. (d) SAR values for 26 nm nano-octopods and 25 nm spherical nanoparticles. Inset is the M−H loops at room temperature. Adapted with permission from ref.[289], copyright 2016 American Chemical Society. (For interpretation of the references to color in this figure legend, the reader is referred to the web version of this article.)

approximately 20 nm. They demonstrated that these nanocubes exhibited about 20 % superior magnetic heating efficiency compared to spherical particles of similar sizes (Fig. 17a).[33] Cheon *et al.* and Srikanth *et al.* also demonstrated theoretically (Fig. 17b)[14] and experimentally (Fig. 17c)[288] that cubic NPs have higher magnetization and higher efficacy of hyperthermia compared to their spherical counterparts.

An alternative to the cubic shape is the nano-octapod shape, which is essentially a deformed nanocube with sharper and elongated cube edges. Srikanth *et al.* conducted a study where they synthesized octapod-shaped nanoparticles using a thermal decomposition method.[289] Compared to spherical shaped particles, octopods exhibit a deformed shape that leads to an increased surface anisotropy by generating local symmetry breaking. The experimental results obtained by Srikanth *et al.* were consistent with theoretical predictions. Although the magnetization versus magnetic field (M−H) loops of the nano-octapods (20 nm) were found to be very similar to their spherical counterparts (25 nm) with the same volume, the specific absorption rate (SAR) values showed significant differences (Fig. 17d). With increasing applied AC magnetic field strength, the SAR of the nano-octapods became increasingly larger than that of the spherical nanoparticles. The SAR of the nano-octapods exhibited more than a 50 % increase compared to spherical nanoparticles when an 800 Oe magnetic field was applied.

6.4.2. 1D or 2D vs spheres

In another study conducted by the Srikanth group, they investigated the SAR values of 1D Fe_3O_4 nanorods and compared them with nanospheres and nanocubes synthesized under similar experimental conditions.[32] The results showed that the SAR values of the nanorods were significantly higher than those obtained for the spheres and cubes, particularly in the high field region (>600 Oe) (Fig. 18a). At 800 Oe, the SAR value for the nanorods was measured to be 862 emu/g, while it was only about 140 and 314 W/g for the spheres and cubes, respectively. The enhanced heating efficiency of nanorods can be attributed to their larger effective anisotropy, which are directly linked to their higher aspect ratio.

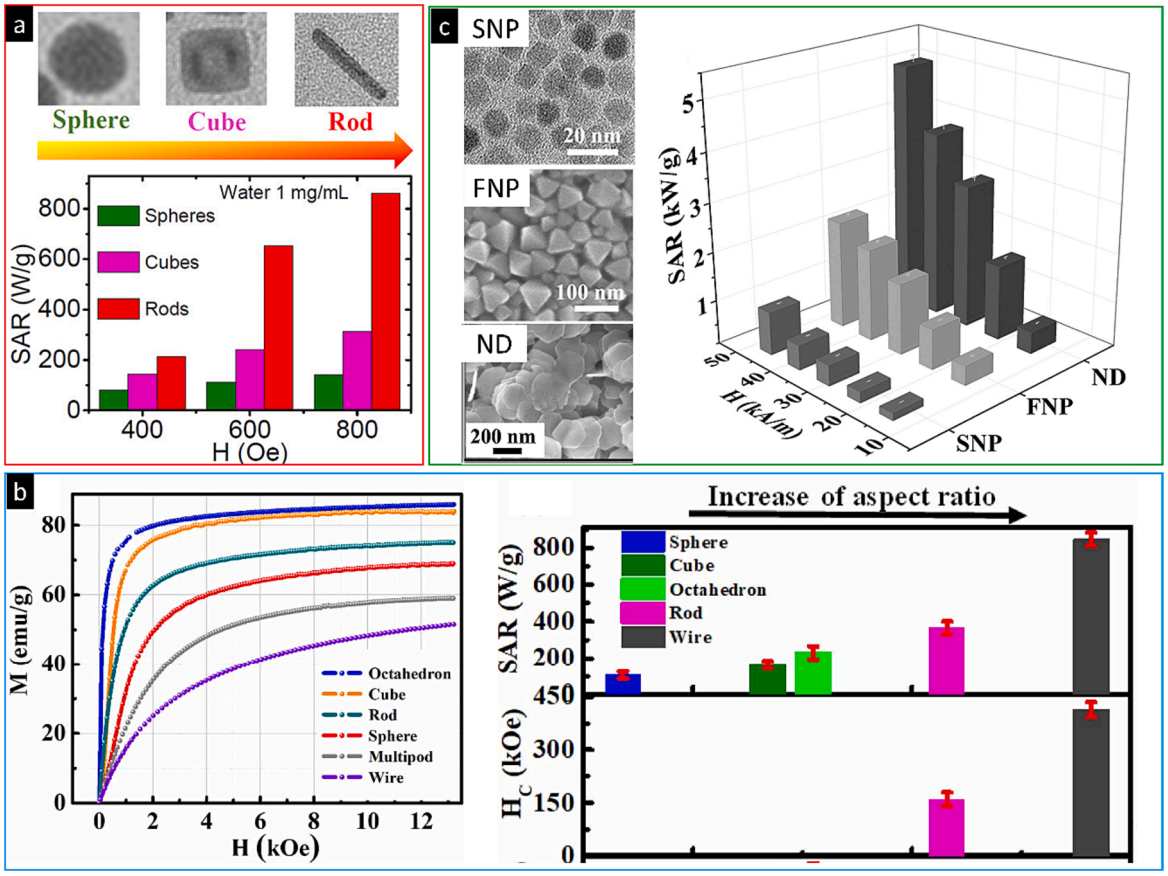

Fig. 18. (a) Top panel: representative TEM images of Fe_3O_4 sphere, cube and rod. Bottom panel: specific absorption rate (SAR) vs. field plot for the Fe_3O_4 spheres, cubes, and nanorods of roughly the same volume (~2000 nm^3). Adapted with permission from ref.[32], copyright 2016 American Chemical Society. (b) Left panel: room temperature field-dependent initial magnetization curves of different shaped Fe_3O_4 nanoparticles. Right panel: the variation of coercivity (H_C) and SAR values of different shapes and sizes Fe_3O_4 nanoparticles. Adapted with permission from ref.[24], copyright 2020 IOP Publishing. (c) Left panel: TEM and SEM images of Fe_3O_4 superparamagnetic nanoparticles (SNP), ferrimagnetic nanoparticles (FNP) and Fe_3O_4 nanodiscs (ND) respectively. Right panel: SAR values of Fe_3O_4 nanostructures measured at different AC magnetic field strengths H. Adapted with permission from ref.[291], copyright 2014 Wiley-VCH.

Liu *et al.* also prepared Fe_3O_4 nanoparticles with different shapes by a 'solventless' synthesis approach to probe shape anisotropy effects on the magnetic and inductive heating properties.[24] Fe_3O_4 in the shapes of spheres, octahedrons, cubes, multipods, rods and high aspect ratio 1D wires were produced. The researchers found that, at a fixed frequency of 265 kHz, the nanowires exhibited a superior SAR of 846 W/g compared to the other shapes of Fe_3O_4 NPs (Fig. 18b). More specifically, the SAR values followed a specific order: wire (long rod) > rod > octahedron > cube > sphere, which correlated with the aspect ratios of the respective shapes (wire: 5.7, rod: 2.5, octahedron: 1.7, cube: 1.7, and spheres: 1). This trend demonstrated that the heating efficiency was influenced by the shape anisotropy, with the nanowires having the highest aspect ratio and the most pronounced shape anisotropy. The observed phenomenon can be attributed to the high shape anisotropy of the nanowires, which significantly increased the hysteresis loss and, consequently, enhanced the heating efficiency. In comparison to spherical Fe_3O_4 nanoparticles (M_S = 69 emu/g), the octahedral, cubic, and rod-shaped nanoparticles exhibited not only higher saturation magnetization (Ms) values (86 emu/g, 84 emu/g, and 75 emu/g, respectively) but also larger hydrodynamic sizes and higher surface anisotropy.[290]

Another higher dimension structure was observed by Ding *et al.*, who prepared highly uniform Fe_3O_4 nanodiscs which showed much higher SAR than isotropic nanoparticles (Fig. 18c).[291] The synthesized nanodiscs had a thickness of approximately 26 nm, a mean diameter of about 225 nm, and an aspect ratio of 8.6. These nanodiscs demonstrated strong shape anisotropy, as reflected by

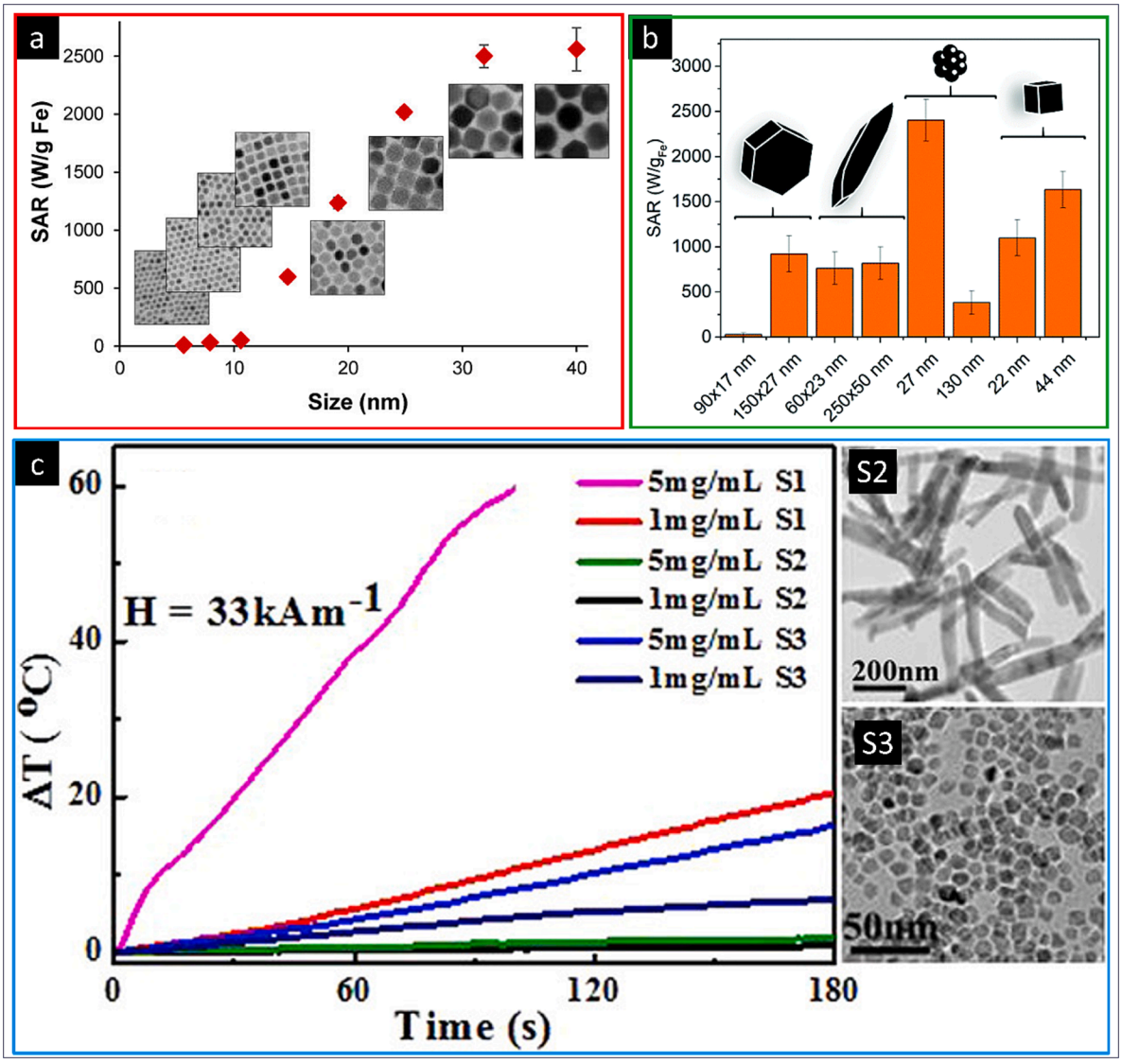

Fig. 19. (a) The specific absorption rate (SAR) values for magnetic iron oxide nanoparticles with different sizes. Adapted with permission from ref. [292], copyright 2017 American Chemical Society. (b) The SAR values for MIPs with different shapes (discs, spindles, flowers and nanocubes) in different sizes. Adapted with permission from ref.[295], copyright 2021 Royal Society of Chemistry. (c) Left panel: heating curves of Fe_3O_4 nanorods with different aspect ratios of 4.5 (S1) and 10 (S2) and 15 nm Fe_3O_4 nanoparticles (S3) at different concentrations. Right panel: (top panel) and (bottom panel) show the corresponding TEM images of S2 and S3. Adapted with permission from ref.[298], copyright 2016 Wiley-VCH.

their magnetic properties. The M_s of the nanodiscs was around 83 emu/g at room temperature, which was more than two times higher than their isotropic counterparts. Additionally, the coercivity (Hc) of the nanodiscs was approximately 21.3 kA/m, further emphasizing their strong shape anisotropy. To compare their performance, the researchers chose ferrimagnetic spheres with a diameter of 58.7 nm, which closely approximated the optimal size for achieving the highest hysteresis loss. The nanodiscs outperformed the ferrimagnetic spheres, demonstrating SAR values of 5 kW/g at 47.8 kA/m, which were more than two times higher than those of the ferrimagnetic nanospheres.[14]

6.4.3. *Size-dependent heating of non-spherical MIPs*

Extensive research has confirmed the influence of size on the heating capabilities of spherical MIPs. In a study conducted by Bao *et al.*, a series of MIPs with sizes ranging from 6 nm to 40 nm were synthesized using thermal decomposition (Fig. 19a).[292] Interestingly, despite the variations in size, the MIPs exhibited similar saturation magnetization (M_s) values of approximately 110 emu/g, which closely resembled the bulk value of 98 emu/g.[293] The magnetization curves of these nanocrystals, measured at a low field strength of $\pm$ 25 $\times$ 103 A/m, which is commonly used in SAR measurements, revealed strong size-dependent microhysteresis curves. Consequently, the heating efficiency of the MIPs increased with size. Therefore, size, along with shape, is a crucial factor that must be considered in understanding and optimizing the heating properties of non-spherical MIPs.

Supporting this notion, Bahadur *et al.* conducted a study where they synthesized octahedral-shaped iron oxide nanoparticles with sizes of 6, 8, and 12 nm.[294] The hydrodynamic size and M_s of the nanoparticles increased as their size increased, ranging from 24 to 43 nm and 71 to 82 emu/g, respectively. Consequently, the SAR also exhibited a corresponding increase with size, ranging from 163 to 275 W/g. Similarly, Serantes *et al.* also found observed a similar trend, where an increase in dimensions for various shapes such as discs, spindles, and cubes resulted in an increased SAR (Fig. 19b).[295] These findings are consistent with the theory that larger saturation magnetization and hydrodynamic size contribute favourably to higher SAR values.

According to the Neél relaxation mechanism for heat generation, greater heating efficiency can be achieved by increasing the effective anisotropy of MIPs. However, a limitation arises when dealing with larger particles, which is that they undergo non-coherent

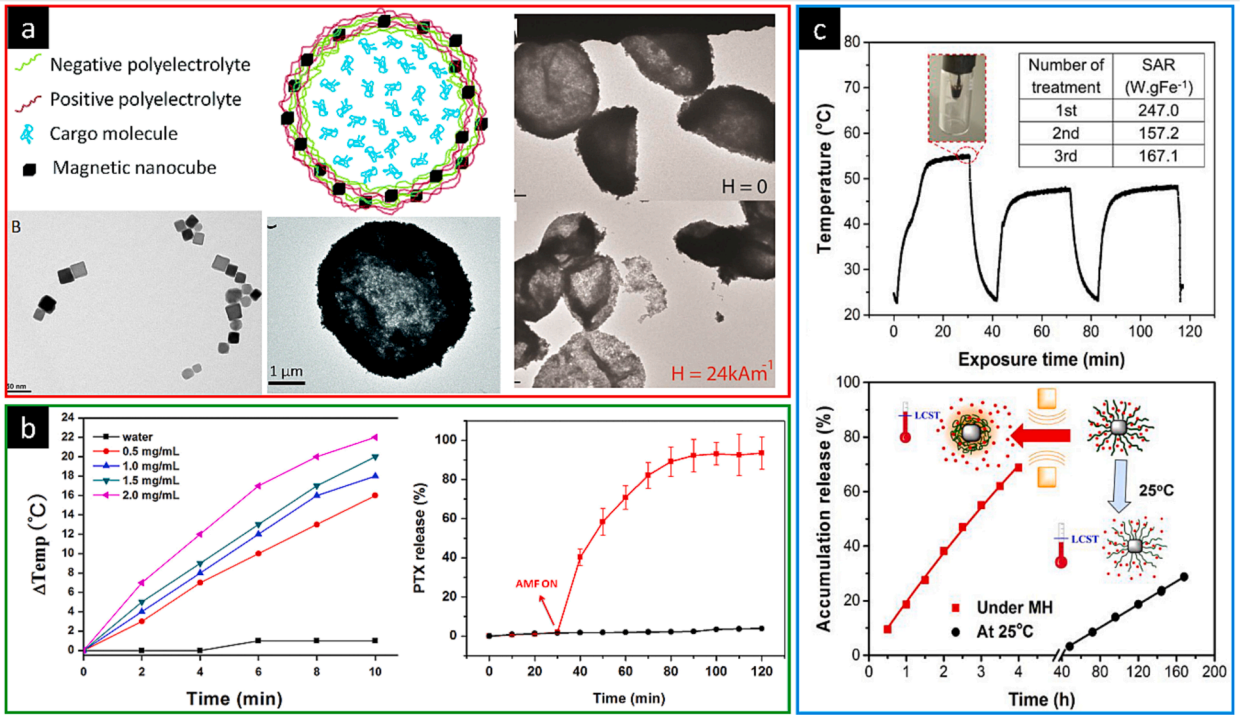

Fig. 20. Left panel: (top panel) sketch of one polyelectrolyte capsule comprising Cascade Blue-labelled dextran as fluorescent cargo in the cavity and magnetic nanoparticles in the wall; TEM images of iron oxide cubes (bottom left) and dried capsules (bottom right). The scale bar corresponds to 1 µm. Right panel: TEM images of polyelectrolyte microcapsules decorated with iron oxide NPs before (top panel) and after (bottom panel) being exposed to an AMF (300 kHz, 24 kAm^{-1}) for 90 min. Adapted with permission from ref.[312], copyright 2015 Royal Society of Chemistry. (b) Left panel: temperature change of iron oxide cubes in PBS solution with different particle concentrations under AMF. Right panel: paclitaxel (PTX) release profile with or without AMF. Adapted with permission from ref.[317], copy right 2016 Elsevier. (c) Top panel: heat profile of thermoresponsive-cubes measured with an optical fiber (cube edge: 19.0 nm, 3.0 g of Fe L^{-1}, in saline) upon 3 cycles of 30 min treatment under MH. Inset: SAR values calculated for each of the three cycles of treatment. Bottom panel: profiles of cumulative doxorubicin (DOXO) release vs time at room temperature (black) and under MH (red). The cumulative releases reached 70 % after 4 h under MH and 25 % after 7 days at 25 °C. Adapted with permission from ref.[318], copyright 2019 American Chemical Society. (For interpretation of the references to color in this figure legend, the reader is referred to the web version of this article.)

magnetization rotation that may negatively affect the specific absorption rate.[296,297] Li *et al.* conducted an experiment with iron oxide nanorods of three different aspect ratios (4.5, 10, and 15) and comparable M_s values (78 emu/g at room temperature). They found that the nanorods with an aspect ratio of 4.5 had a coercivity (H_c) value of only about 38 Oe, whereas the nanorods with an aspect ratio of 10 had an increased H_c value of 334 Oe.[298] Surprisingly, at a concentration of 5 mg/mL and an alternating current (AC) magnetic field of 33 kA/m, the nanorods with an aspect ratio of 4.5 achieved a SAR of up to 1072 W/g. Remarkably, the SAR of the nanorods with an aspect ratio of 4.5 was nine times higher than that of the nanorods with an aspect ratio of 10 (Fig. 19c). The authors proposed that this difference in SAR could be attributed to the fact that nanorods with a very high aspect ratio require a larger switching field to reverse their magnetization moment, resulting in lower heating efficiency.

In addition to the previously mentioned research, Srikanth *et al.* also found that for a given shape, when the amplitude of the AC field and the field induced coercive field becomes much bigger than the intrinsic coercive field of the particles, the bigger particles start to fully respond to the magnetic field excitations and their corresponding SAR continuously increases, while for the smaller particles, only a minor improvement in the heating efficiency can be observed.[289]

Notably, similar to what has been found in the study of spherical MIPs for hyperthermia that both size and size polydispersity have an important influence on their hyperthermia,[299,300] the shape polydispersity of MIPs also play an important role in magnetic fluid hyperthermia. Baldomir *et al.* investigated the role of the particles' anisotropy dispersity in relation to the amplitude (H_{max}) of the AC magnetic field using a Monte Carlo technique.[301] Their results indicate that large anisotropy leads to enhanced global heating, whereas lower anisotropy to better homogeneous local heating.

6.4.4. Hyperthermia mediated drug release

MIPs possess unique physicochemical properties such as high surface area, biocompatibility, and tunable surface functionalization. These properties, combined with their ability to act as heat mediators, make MIPs promising platforms for efficient drug delivery.[302–304] One promising strategy for achieving targeted drug delivery using MNPs involves the utilization of magnetic force. Typically, drug molecules and magnetic moieties are combined to create stable formulations using polymers, liposomes, inorganic materials, proteins, or other methods.[305–308] Moreover, the combination of heat-responsive drug delivery, magnetically mediated hyperthermia, and drug targeting has gained significant attention.[309] When an alternating magnetic field is applied, energy is transferred to the magnetic nanoparticles, resulting in their heating and causing mechanical responses that agitate the carrier vehicle. This agitation enhances drug release. There are two primary mechanisms by which magnetically triggered release can occur. In the first mechanism, the drug molecule is linked to the MIP, and drug release is facilitated through hyperthermia-induced bond breaking. Alternatively, drug release can be achieved through the creation of mechanically forced or thermally responsive openings, especially in the case of thermoresponsive polymers.[310,311]

Non-spherical magnetic MIPs offer clear advantages over spherical MIPs for drug delivery. Their high surface-to-volume ratio, combined with enhanced magnetic response and improved cargo hosting capabilities, make them particularly promising. A notable proof-of-concept experiment by Parak *et al.* demonstrated magnetically triggered molecular cargo release from MIP-loaded microcapsules.[312] The microcapsules were constructed using polyelectrolyte layer-by-layer self-assembly techniques, employing sacrificial $CaCO_3$ spheres as templates. The resulting microcapsules had a diameter of 4.5 μm, with polymeric walls integrated with iron oxide cubes measuring 18 nm on each edge (Fig. 20a). Cascade blue-labelled dextran, an organic fluorescent polymer, was loaded into these capsules as a model molecular cargo. The loaded capsules exhibited a high SAR of 427 W/g (at 300 kHz and 24 kA/m). Although this SAR was lower than that of non-encapsulated iron oxide cubes (with a SAR of 824 W/g), the reduction in SAR can be attributed to the low thermal conductivity of the polymer coating and the increased magnetic dipole–dipole interactions when the cubes were embedded within the polymer shells.[313,314] Upon applying an alternating magnetic field with a frequency of 300 kHz and amplitude of 24 kA/m for 90 min, the walls of the capsules were broken, leading to the release of the loaded molecular cargo. Besides heat generation, the alignment of the magnetic particles embedded in the polyelectrolyte shell structure along the direction of the magnetic field created stress within the polyelectrolyte network. This stress resulted in the loosening of the particles and facilitated the penetration and desorption of the cargo macromolecules.[315]

Another approach to achieve AMF-triggered release involves utilizing heat to induce a phase transition in thermosensitive (co) polymers or to weaken the hydrophobic interactions between hydrophobic drugs and hydrophobic composites.[316] In line with this strategy, Wang *et al.* functionalized magnetic nanocubes with a thermo-sensitive sol–gel block copolymer.[317] The resulting composite material exhibited high sensitivity to the applied AC field, leading to pulsatile drug release. When an AC field was applied at a concentration of 2.0 mg/mL (200 kHz, 300 A), the temperature increased by up to 22 °C within 10 min (Fig. 20b). Upon turning on the field, rapid drug release occurred, with 40.3 % of the drug released within the first 10 min and a total of 93.4 % released after 2 h of AMF application. Pellegrino's group reported the surface functionalization of magnetite nanocubes with a thermoresponsive polymer shell through surface-initiated polymerization.[318] These thermoresponsive magnetic nanocubes exhibited remarkable SAR performance under clinically relevant magnetic hyperthermia (MHT) conditions ($H = 11$ kA/m, $f = 105$ kHz). The temperature difference (ΔT) between the tumor and the skin (distant from the tumor) reached approximately 15 °C, which is the highest ΔT reported for such iron oxide-based MIPs in an *in vivo* experiment under clinical AMF conditions ($Hf \leq 5 \times 10^9$ A/m s^{-1}). After loading the antitumoral drug doxorubicin (DOXO), the DOXO-cubes composite material demonstrated efficient heat-mediated drug release at a significantly lower DOXO dose. The release profile of DOXO was enhanced by 3-fold compared to that at room temperature, with 70 % of the loaded DOXO released after 4 h of magnetic hyperthermia (equivalent to 32.9 μg of DOXO per 1 mg of Fe) (Fig. 20c). At 25 °C, the maximum DOXO release was reached after 7 days, corresponding to only 25 % of the loaded amount (*i.e.*, 11.8 μg of DOXO per mg of Fe).

Considering recent experimental findings, a key challenge in hyperthermia-controlled drug delivery is to maximize the SAR during hyperthermia, which allows for a reduction in the required ferrofluid dose *in vivo*. As discussed in the previous section regarding the

structure-dependent SAR based on particle shape, anisotropic particles hold great potential for hyperthermia-mediated drug release.

6.5. Magneto-mechanical actuation for cancer therapy

In contrast to the high-frequency alternating magnetic field (AMF)-induced magnetic hyperthermia, recently, low-frequency mechanical vibrations of magnetic nanoparticles have gained great attention due to their diverse applications in tissue engineering, [319,320] drug delivery,[321,322] neuronal stimulation and regeneration,[323,324] artificial muscles,[325] microrobots or micro-swimmers,[326,327] and more. These applications leverage the unique properties of magnetic nanoparticles at lower frequencies, expanding their utility beyond hyperthermic effects to various fields of biomedical research and technology development. More interestingly, the magneto-mechanical actuation (MMA) effect, propelled by low-frequency magnetic fields, presents an intriguing avenue for applying targeted forces to investigate cellular responses in tumor cells. This approach holds promise, potentially yielding fewer side effects compared to methods based on hyperthermia, as MMA requires lower frequencies (*i.e.* $f <$ 100 Hz compared to $f >$ kHz frequencies required for magnetic hyperthermia).[322,328] This article does not delve into a detailed exploration of the mechanisms governing energy transfer from MIPs to target objects and their role in mediating cell growth, as comprehensive discussions on these aspects can be found in existing papers[44,329–336] and reviews.[40–42,337–340] Instead, our focus here will center on the shape-dependent magneto-mechanical actuation (MMA) effects of MIPs for cancer therapy.

In a low-frequency alternating magnetic field, the MMA effect of MIPs can be characterized by the following formulas. In a uniform AMF with induction $\boldsymbol{B}$, the magnetic torque is given by $\boldsymbol{L} = \boldsymbol{\mu} \times \boldsymbol{B}$, while in a non-uniform AMF, the rotation moment is supplemented by the force $\boldsymbol{F} = (\boldsymbol{\mu} \cdot \nabla)\boldsymbol{B}$, where μ is the magnetic moment of MIPs, $\boldsymbol{B}$ is the induction of the magnetic field, $\boldsymbol{L}$ and $\boldsymbol{F}$ are the torque and force, respectively.[40,339] The amplitude of MMA for a magnetic nanoparticle is governed by factors such as its hydrodynamic radius, magnetic moment, the viscoelastic properties of the environment, the intensity and frequency of the magnetic field, and the initial angle between vectors $\boldsymbol{\mu}$ and $\boldsymbol{B}$. Frequency is a key factor in optimizing the magneto-mechanical actuation (MMA) effect while minimizing energy loss from heating and dissipation processes. In general, larger hydrodynamic radii of MIPs tend to favor lower AMF frequencies. As previously mentioned, anisotropic particles have a larger hydrodynamic size compared to spherical counterparts, making them more suitable for lower AMF frequencies. Additionally, anchored MIPs can apply maximum contact force on binding macromolecules, further highlighting the advantage of anisotropic nanoparticles with their higher surface-to-volume ratios over

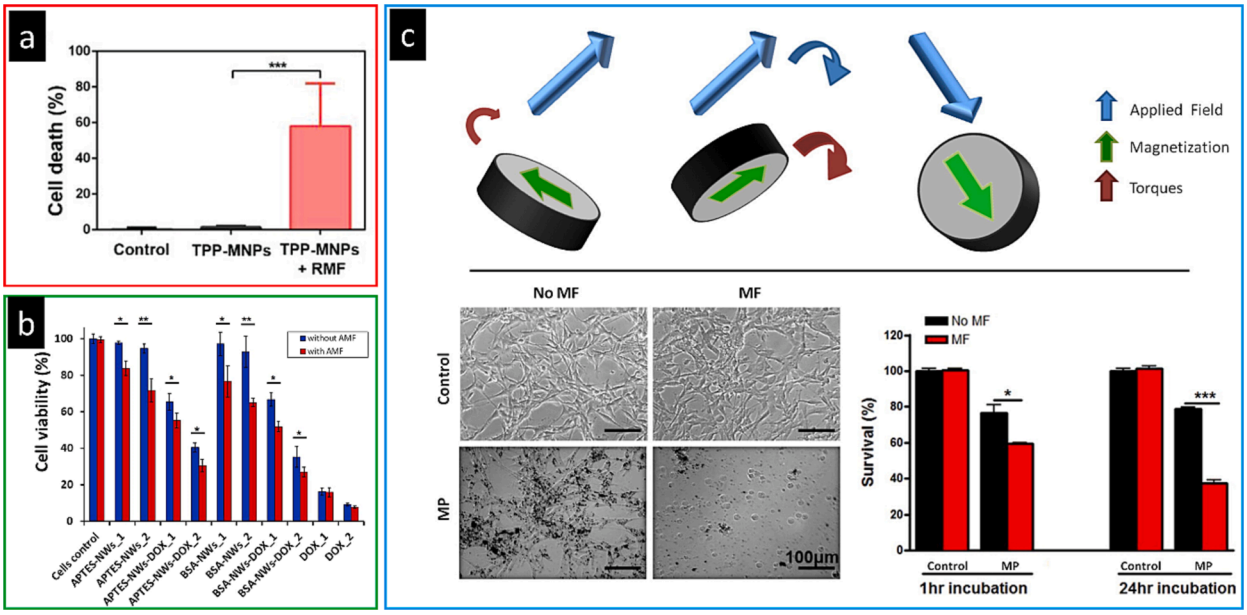

Fig. 21. (a) Cell death rate of U87 cells after 4 h of treatment *in vitro* calculated by ImageJ. The concentration of Fe was 50 μg mL^{-1}, and the incubation time was 24 h. The apoptosis rate was 58.0 % in the TPP-MNPs (triphenylphosphonium cation (TPP) functionalized zinc-doped iron oxide nanocubes (MNPs) group under rotating magnetic field compared to the 0.5 % in the control and 1.3 % in the TPP-MNPs group. Adapted with permission from ref.[44], copyright 2019 John Wiley and Sons. (b) Viability of MDA-MB-231 cells incubated with different formulations and with or without application of a low frequency alternating magnetic field (AMF) ((1 mT, 10 Hz for 10 min)). The Fe magnetic nanowires (NWs) were functionalized with different biocompatible coatings, (3-aminopropyl)triethoxysilane (APTES), bovine serum albumin (BSA), doxorubicin (DOX). Adapted with permission from ref.[342], copy right 2016 Springer Nature. (c) In vitro cell destruction using disk-shaped magnetic particles (MPs) under a rotating magnetic field (MF). Top panel: schematic of MPs under a rotating MF. Bottom left panel: optical images of U87 glioma cells with (MF) and without (no MF) MF treatment (1 Tesla at 20 Hz for 30 min). Cells were treated with either growth media (control) or MPs at 50 particles per cell for 24 h. Scale: 100 μm. Bottom right panel: quantification of the U87 cells viability after incubation with the MPs for 1 h and 24 h or not, and after MF treatment or not. Data are presented as Mean ± SE. * $p < 0.05$, *** $p < 0.001$ (Student's *t* test). Adapted with permission from ref. [344], copyright 2016 Elsevier.

spherical ones.

Kabanov *et al.* utilized nitrodopamine PEG (ND-PEG) coated cubic-shaped MIPs to remotely control the expression of the tumor necrosis factor-related apoptosis-inducing ligand (TRAIL) protein, secreted by transduced cells.[341] Their findings demonstrated a significant downregulation of TRAIL, with secretion levels reduced to 30 %, when intracellular particles at a concentration of 0.100 mg/mL Fe were activated by magnetic fields (65 mT and 50 Hz for 30 min). This effect is attributed to the excellent magnetic properties of cubic ND-PEG-SPIONs, which, even at low magnetic field strengths (<100 mT), retained approximately 60 % of their saturation magnetization. Cubic-shaped MIPs offer an additional advantage as they can be easily aligned with an external field, generating a localized mechanical force to disrupt cancer cells. For instance, Cheng *et al.* designed 20 nm mitochondria-targeted zinc-doped iron oxide nanocubes for the investigation of magneto-mechanical destruction of cancer cells under a rotating magnetic field (which can be considered a form of a non-uniform alternating magnetic field) (Fig. 21a).[44] Upon internalization into cancer cells, the nanocubes accumulated in the mitochondria and could be assembled by applying a magnetic field. The application of a rotating magnetic field with a frequency of 15 Hz and a modulus of 40 mT induced mitochondrial dysfunction, leading to cancer cell death.

Rather than relying on the assembly of nanocubes under a magnetic field, wire- or rod-shaped MIPs, with their intrinsic 1D structure, exhibit a high degree of cellular internalization (see section 6.6), making them promising candidates for magneto-mechanical actuation. In a study by Kosel *et al.*, cancer cell death was induced by combining the chemotherapeutic effect of doxorubicin (DOX)-functionalized iron nanowires (NWs) with mechanical disturbance under a low-frequency alternating magnetic field (Fig. 21b).[342] The functionalized NWs demonstrated a comparable cytotoxic effect in breast cancer cells in a DOX concentration-dependent manner (approximately 60 % at the highest concentration tested), which significantly differed from the effects produced by free DOX and non-functionalized NWs formulations. A synergistic cytotoxic effect was observed when applying a magnetic field (1 mT, 10 Hz) to cells treated with DOX-functionalized BSA or APTES-coated NWs, reaching approximately 70 % cell death at the highest concentration.

Disk-shaped MIPs have demonstrated effectiveness in generating mechanical torque under a magnetic field, making them ideal magnetomechanical actuators for disrupting cancer cell integrity.[43,343] Lesniak *et al.* exemplified this by successfully using spin-vortex, disk-shaped permalloy magnetic particles in a low-frequency (20 Hz), rotating magnetic field for both *in vitro* and *in vivo*

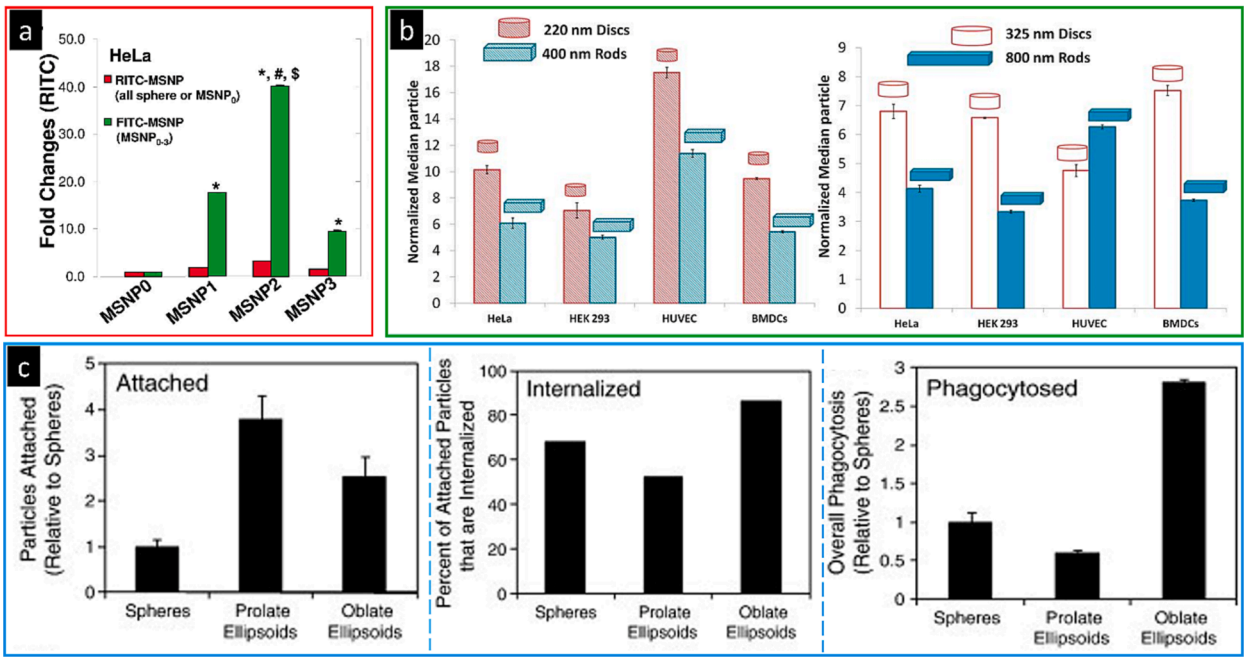

Fig. 22. (a) HeLa cells were treated with 20 μg/mL FITC-labelled particles of different dimensions for 6 h in complete RPMI cell culture medium, with the graph showing the fold increase in mean fluorescence intensity (MFI) compared to spherical FITC-labelled mesoporous silica nanoparticle (MSNP). MSNP0 (spheres of ~110 nm diameter), rod-shaped cylinders with dimensions (height/diameter) of 110–130/60–80 nm (MSNP1), 160–190/60–90 nm (MSNP2), and 260–300/50–70 nm (MSNP3) were used for comparison. RITC-labelled nanosphere uptake was used as another internal control for comparing each FITC-labelled spheres and rods to an alternatively labelled sphere. Adapted with permission from ref.[352], copyright 2011 American Chemical Society. (b) Cellular-uptake kinetics of different shape-specific polyethylene glycol diacrylate nanoparticles in various cell lines. Normalized median particle uptake per cell (indicates relative number of particles internalized by cells when normalized to 100 particles of 80 × 70-nm discs) at the maximum internalization time point (72 h for HeLa and BMDC, 48 h for HEKs, and 24 h for endothelial cells). Adapted with permission from ref[357], copyright 2013 National Academy of Sciences. (c) Comparison of attachment and internalization of polystyrene particles of various shapes prepared from 1 μm spheres. (Left panel) Number of particles attached to cells; (middle panel) particles internalized by cells; and (Right panel) overall phagocytosis after a 6 h incubation. Adapted with permission from ref.[359], copyright 2010 Elsevier.

destruction of glioma cells (Fig. 21c).[344] The internalized nanomagnets aligned themselves to the plane of the rotating magnetic field, creating a potent mechanical force that damaged the cancer cell structure and induced programmed cell death. In their *in vitro* studies, a significant percentage of magnetic particles were internalized into glioma cells, generating enough force to compromise the integrity of cancer cell membranes, resulting in a substantial loss of viability—up to 89 % non-viable cells were induced after magnetic field treatment.

6.6. Cellular uptake

Cellular uptake plays a crucial role in drug and gene delivery, and nanomaterials exploit various endocytic pathways to reach intracellular compartments. The efficiency of intracellular uptake is heavily influenced by particle properties such as shape, size, and surface functionalization, as well as membrane characteristics and particle geometry.[345] The shape of nanoparticles plays a crucial role in determining their cellular uptake efficiency and mechanisms.[346,347] While current research predominantly focuses on noble metal and polymeric nanoparticles due to their well-established synthesis methods, it is crucial to expand these investigations to encompass a broader range of materials and morphologies. Recent studies have highlighted the importance of particle shape in cellular uptake, emphasizing the need to explore different shapes, sizes, and surface functionalizations to optimize drug delivery systems.[348,349] However, it is worth noting that there are a limited number of studies which compare directly analogous 0D, 1D and 2D MIPs in terms of their cellular behavior, uptake and drug delivery. Therefore, here we will provide general knowledge about the impact of particle shape on cellular uptake, which can be applicable to a wider range of materials, with principles not limited to magnetic materials.[346,350,351]

6.6.1. 0D vs 1D

Recent research has indicated that elongated nanoparticles offer advantages over spherical nanoparticles. While various materials and sizes have been studied, one noteworthy investigation by Nel *et al.* synthesized mesoporous spherical and rod-shaped silica NPs. The researchers examined the cellular uptake of these particles using cytometry and found that the rod-shaped NPs exhibited significantly higher uptake compared to the spherical NPs (Fig. 22a). This observation was made in HeLa and A549 cells, suggesting that the elongated shape of the particles enhances their cellular uptake.[352] Another study by Desimone *et al.* also highlighted the importance of particle shape in cellular internalization. Notably, the hydrogel particles were fabricated using a top-down lithographic technique, allowing for precise control over their size in three dimensions. Although the reported low-aspect-ratio cylindrical particles, with a diameter of 200 nm and a height of 200 nm, and the high-aspect-ratio cylindrical particles, with a diameter of 150 nm and a height of 450 nm, possess comparable volumes (6.3×10^{-3} μm^3 and 7.9×10^{-3} μm^3, respectively), their rates of internalization exhibited notable differences. This highlights the significant influence of particle morphology on cellular uptake dynamics, where rod-like nanoparticles with high aspect ratios were internalized more rapidly and efficiently compared to their symmetric cylindrical counterparts of similar volumes. The higher-aspect-ratio particles, with their larger surface areas in contact with the cell membrane, are thought to facilitate stronger multivalent cationic interactions with the cells, leading to enhanced internalization.[353] It is worth noting that these advantageous properties of elongated nanoparticles have been observed across different studies utilizing diverse materials.[354] Notably, similar trends have emerged in studies involving anisotropic magnetic nanochains and spherical magnetic nanoparticles. For example, Kreft *et al.* explored the impact of shape anisotropy in magnetic nanoparticles on cellular uptake. In contrast to spherical particles, anisotropic nanochains exhibited a preference for accumulating in cancer cells.[355]

While there is evidence supporting the idea that elongated particle shapes may improve cellular uptake efficiency, conflicting results have been reported on the association between nanoparticle shape and cellular uptake. One study by Crespy *et al.* involved the synthesis of fluorescently labelled spherical polymer nanoparticles, which were then mechanically deformed to produce quasi-ellipsoidal particles with varying aspect ratios, thus ensuring that spherical particles have equal volumes to their elongated ellipsoid counterparts.[356] The researchers used electron microscopy, confocal laser scanning microscopy, and flow cytometry to investigate the cellular uptake behaviors of spherical and non-spherical particles of equal volume. The findings revealed that non-spherical particles exhibited decreased cellular uptake compared to their spherical counterparts, indicating a negative correlation between aspect ratio and uptake rate. This was attributed to the larger average curvature radius of adsorbed non-spherical particles experienced by the cells.

Significantly, the cellular uptake behavior of nanoparticles is intricately linked to their physicochemical attributes, encompassing dimensions such as size, shape, and surface properties.[356] Given the innate divergence in shape within the chosen models, it is imperative to underscore the significance of selecting nanoparticles with similar sizes to ensure methodological rigor. Without commensurate consideration for factors such as surface area and volumetric parameters, the derivation of conclusive findings becomes inherently challenging.

6.6.2. 1D vs 2D

In a study conducted by Roy *et al.*, monodispersed rod-shaped and disc-shaped hydrogel nanoparticles were prepared to investigate the shape-specific mechanisms of cellular uptake.[357] The researchers selected polyethylene glycol diacrylate as the material for particle fabrication due to its biocompatible, hydrophilic, and anionic properties, which minimized aggregation in serum and electrostatic adsorption to negatively charged cell membranes. The aim was to examine how particle shape influences cell uptake. The findings of the study demonstrated that, across three types of cells (epithelial, endothelial, and immune cells), both disc-shaped and rod-shaped nanoparticles with larger volumes exhibited more effective cellular uptake compared to their spherical counterparts. Furthermore, when evaluating discoidal nanoparticles and nanorods of comparable volume, it was found that the disc-shaped

nanoparticles were internalized with greater efficiency, except in HUVEC cells, where intermediately sized discs were most effective among all the models (Fig. 22b). The researchers proposed three key parameters that contribute to the intracellular uptake of particles: the contact or adhesion force between the nanoparticle surface and the cell membrane (governed by the particle shape), sedimentation (governed by the weight of particles), and the strain energy required for membrane deformation (governed by the particle shape). In the case of particles with the same volume and surface area, the strain energy cost for uptake was found to be higher for rods compared

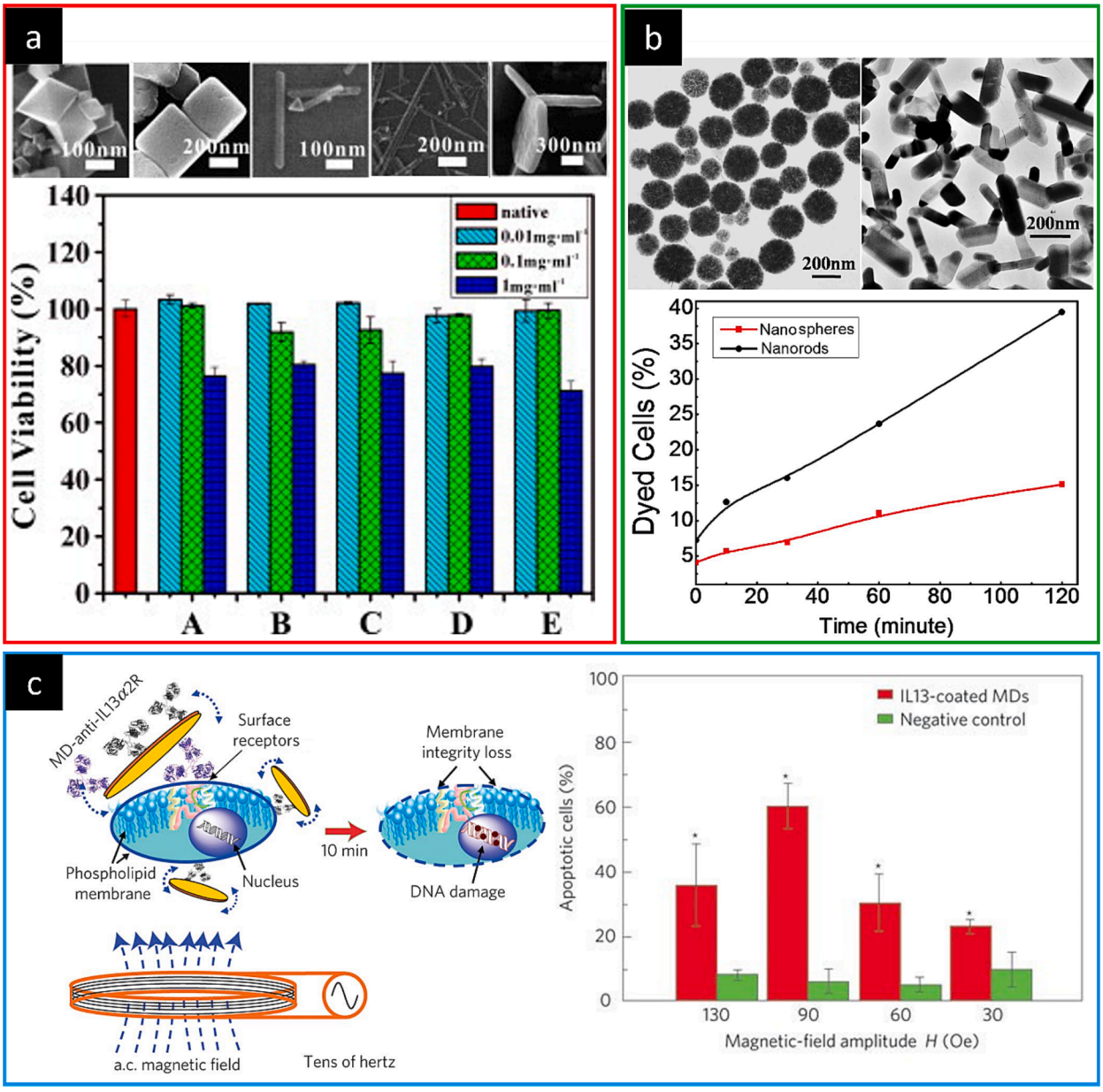

Fig. 23. (a) Top panel: representative SEM images of iron oxide nanocrystals with various morphologies (from left to right): Fe_3O_4 octahedron, Fe_3O_4 cube, Fe_3O_4 rod, α-Fe_2O_3 wire, α-Fe_2O_3 hexagonal plate. Bottom panel: Cell viability results of A549 cells after 24 h exposure to 1, 0.1 and 0.01 mg mL^{-1} iron oxide samples: (A) Fe_3O_4 octahedron, (B) Fe_3O_4 cube, (C) Fe_3O_4 rod, (D) α-Fe_2O_3 wire, (E) α-Fe_2O_3 hexagonal plate. Adapted with permission from ref.[152], copyright 2012 Elsevier. (b) Top panel: TEM images of spherical (left) and rod-shaped (right) iron oxide nanoparticles. Bottom panel: Percentage of trypan blue-stained cells. These cells had been pre-cultured in 100 μg/mL iron oxide nanoparticles suspended culture medium and exposed to an AMF for up to 2 h. Adapted with permission from ref.[374], copyright 2014 Springer Nature. (c) Left panel: the microdiscs are biofunctionalized with anti-human-IL13α2R antibody, specifically targeting human glioblastoma cells. When an alternating magnetic field is applied, the magnetic discs oscillate, compromising membrane integrity and initiating spin-vortex-mediated programmed cell death. Right panel: apoptosis of the N10 cells induced by an AC magnetic field. Adapted with permission from ref.[375], copyright 2010 Springer Nature. (For interpretation of the references to color in this figure legend, the reader is referred to the web version of this article.)

to discs. As a result, 2D discs were taken up more efficiently than rods.

6.6.3. 0D vs 1D vs 2D

Mitragotri *et al.* prepared polystyrene nanoparticles of different shapes and investigated the effect of particle shape on phagocytosis.[358] Surprisingly, the results revealed that particle shape, rather than size, played a dominant role in macrophage uptake. The local particle shape at the point of initial contact, rather than the overall particle shape, was found to determine the complexity of the actin structure required to initiate phagocytosis. This, in turn, dictated whether the particles were phagocytosed or simply spread on the cell membranes. In a subsequent study, the researchers further explored the effects of particle shape on the attachment and internalization of particles by macrophages.[359] They prepared polystyrene particles in the shapes of spheres, 1D prolate ellipsoids, and 2D oblates as model particles. The findings showed that 1D prolate ellipsoid particles attached more efficiently to the macrophages compared to the oblate ellipsoid or spherical particles (Fig. 22c). However, the 2D oblate particles exhibited higher internalization efficiency compared to the spherical or prolate ellipsoid particles. The lower aspect ratio of the oblate ellipsoids required less actin remodeling for internalization, which likely contributed to their higher internalization efficiency.

There have also been studies exploring the cellular uptake behaviors of MIPs as models; for example, Begin-Colin *et al.* undertook the synthesis of a variety of iron oxide nanoparticles with diverse shapes, encompassing cubic, spherical, octopod, and nanoplate structures.[360] Their focus was on investigating the uptake efficiency in non-spherical iron oxide particles compared to their spherical counterparts. Intriguingly, the study revealed that both cubic and octopod-shaped particles exhibited higher internalization compared to the spherical and nanoplate-shaped ones. In another study, Li *et al.* synthesized a series of Fe_2O_3 nanoparticles, including four hexagonal nanoplates with controlled diameters and thicknesses, along with four nanorods with systematically adjusted lengths and diameters.[361] When investigating their cellular uptake in THP-1 cells, the results revealed that nanorods exhibited higher bioavailability compared to hexagonal nanoplates.

Thus, the shape of particles has been shown to have a significant impact on particle-cell interactions. However, when it comes to attachment and internalization, the effects of particle shape are not yet fully understood, and the design of particles for cellular uptake involves considering multiple complex factors. For particles with complex shapes, extra caution should be exercised when attempting to utilize particle shape to modulate particle-cell interactions. The influence of shape on cellular uptake, despite garnering significant attention recently, remains a topic of debate and controversy among researchers. For example, Jiang *et al* conducted a study where they compared the uptake of silver nanorods (with an average diameter of around 55 nm and length of 200 nm) to that of nanospheres (with an average diameter of about 60 nm) by Hela and HUVEC cells. Surprisingly, they found that the nanorods were taken up by a far lesser extent than the nanospheres across a wide range of concentrations.[362] This highlights the complexity of the relationship between particle shape and cellular uptake. It is important to note that the interaction between a nanoparticle and the cell membrane is also influenced by the proteins adsorbed onto the nanoparticles' surfaces. Therefore, in addition to shape, other surface properties such as diameter, charge, and functional groups should also be taken into consideration when designing particles for cellular uptake.[363,364]

6.7. Cytotoxicity

Comprehensive cytotoxicity studies are indeed crucial for the development of MIPs in biomedical applications such as diagnostics and therapeutics. Generally, the cytotoxicity of MIPs is considered to be dependent on their concentration, and at lower levels, no observable toxicity is usually seen as these particles can be effectively cleared from the body.[365–367] It is worth noting that iron oxide and oxyhydroxide nanoparticles, which are commonly used in MIPs, have been approved by the Food and Drug Administration (FDA) for various applications. For example, they are used as iron supplements, and iron oxides have been approved as contrast agents for MRI. Ferumoxytol, a superparamagnetic iron oxide nanoparticle-based agent, has been clinically tested in over 2000 patients for the detection of lymph node metastasis using MRI.[368,369] Magnetic iron-based nanoparticles, due to their lower safety concerns compared to other nanomaterials, hold promise for the development of theranostic agents for image-guided and targeted cancer therapies.[78,370] It is critical to design MIPs that possess sufficient internalization properties and meet the specific demands of a particular application without compromising cellular toxicity. While most cytotoxicity studies have focused on spherical MIPs, only a few studies have investigated non-spherical MIPs. Considering the increasing interest in non-spherical particles, additional research efforts are necessary to comprehensively evaluate their cytotoxicity and establish their safety profiles. This will help ensure the development of safe and effective MIPs for biomedical applications.

One example of non-spherical particles is by Zhang *et al.*, who conducted research on iron oxide nanocrystals with various well-controlled morphologies (octahedra, cubes, rods, wires, and plates) and compositions (Fe_3O_4 and α-Fe_2O_3) to assess their cytotoxicity.[152] It was demonstrated that, after 24 h incubation, more than 90 % cells could survive when the concentration of these nanocrystals were 0.01 or 0.1 mg mL^{-1}, which suggested that these iron oxide NCs are quite safe to the living cells (Fig. 23a).

Another study investigated the cytotoxicity and cell uptake of elongated magnetic nanorods compared to their spherical counterparts with equivalent volumes.[371] The results indicated that the elongated nanorods exhibited over 2.5-fold higher cell uptake compared to the spherical nanorods. However, both the oligosaccharide-coated spherical and elongated nanorods demonstrated low toxicities at a concentration of 0.25 Fe mg/mL after 24 h across five different cancer cell lines: 4 T1, MiaPaCa2, HepG2, Raw264.7, and HeLa. An *in vitro* biocompatibility study carried out on MIPs with different morphologies including nanooctahedrons, nanorods and nanocubes in human A549 lung tumor cells also suggested that these nanoparticles were quite safe to the cells within the tested concentration range.[279]

Similarly, Chen *et al.* conducted a study examining the cytotoxicity of glycopolymer (poly(2-(methacrylamido)glucopyranose))-

decorated iron oxide nanoparticles (IO-PMAG) featuring various shapes and compositions,[372] including spindle-like Fe_2O_3@PMAG core@shell particles and cubic-like Fe_3O_4@PMAG. Despite variations in composition and shape, the researchers used the CCK-8 assay kit to evaluate cytotoxicity. Remarkably, both Fe_2O_3@PMAG and Fe_3O_4@PMAG demonstrated no cytotoxicity at the tested concentrations. Importantly, even at concentrations surpassing typical levels of conventional iron oxide-based MRI contrast agents used in mice (1–20 mg kg^{-1}), the glycopolymer-decorated iron oxide nanoparticles showed no harmful effects. This highlights the robust biocompatibility of these nanoparticles, suggesting their potential for safe use in biomedical applications.

On the other hand, as described in section 6.4 and section 6.5, it has been found that the physical rotation and mechanical disruption caused by the movement of MIPs in response to alternating magnetic fields can indeed induce cell death.[373] For example, in a study comparing the cellular effects of elongated magnetic nanorods (200 x 50 nm in length, and 50 to 120 nm in diameter) with spherical MIPs (200 $\pm$ 50 nm), it was found that the elongated nanorods exhibited slightly higher cell uptake than the spherical MIPs, but their cytotoxicity was comparable.[374] However, when an AMF was applied at a concentration of 100 μg/mL, the corresponding cell viability decreased significantly to 30.9 % for elongated nanorods and 11.7 % for spherical MIPs (Fig. 23b). The asymmetrical morphology of the rod-shaped nanorods resulted in a greater magnetic torque, leading to more intense physical oscillation in the AMF. This mechanical oscillation caused cell death specifically under the influence of the oscillating magnetic field.

Similar to 1D elongated nanoparticles, 2D nanodiscs morphology could induce cell death through magneto-mechanical effects. For example, For example, nanodiscs composed of a 20:80 % iron-nickel (permalloy) alloy, with a diameter of 1 μm and a thickness of 60 nm, coated with a 5-nm-thick layer of gold, were able to exert mechanical forces on cells under a low-frequency alternating magnetic field (10 and 20 Hz, 90 Oe) and induce apoptosis in N10 glioma cells (Fig. 23c).[375] The mechanism of cell death can be regulated by the magnitude of the magnetic field. When a low-frequency alternating magnetic field is applied, it causes a shift in the vortex structure of the nanodiscs, creating an oscillation and transmitting a mechanical force to the cells.

7. Concluding remarks and perspectives

The recent advancements in the synthesis and surface modification of non-spherical magnetic iron oxide particles (MIPs) have opened up new possibilities for their application in various bio-related fields. These non-spherical MIPs can be engineered to possess specific magnetic properties, allowing for fine-tuning and enhanced performance in bio-applications. One significant advantage of non-spherical MIPs with uniform shape and size is their high magnetic anisotropy, which can be finely controlled by carefully designing their shape and structure. This magnetic anisotropy is crucial for their bio-applications such as MRI, MPI and hyperthermia (-mediated drug delivery). Additionally, non-spherical MIPs offer large surface area-to-volume ratios. This characteristic, along with their magnetic anisotropy, contributes to the abovementioned applications and provides additional benefits. The increased surface area facilitates a higher number of binding sites, enhancing the capacity of the MIPs to interact with target molecules, such as drugs or specific biomarkers, which is particularly important for drug delivery applications. The larger surface area also improves the cellular uptake efficiency of the MIPs, allowing for enhanced interaction with target cells and improved therapeutic efficacy.

This review provides a comprehensive summary of recent research on non-spherical MIPs and their biomedical applications. The aim is to offer guidelines for future advancements in this rapidly developing field. The review covers various aspects of non-spherical MIPs, including their mechanisms, synthesis methods, surface modifications, applications, as well as their cytotoxicity and cellular uptake behaviors. One notable observation is the remarkable structural evolution of MIPs in terms of preparation and biomedical application, progressing from 0D to 2D MIPs over the past two decades. These advancements have demonstrated the versatility and potential of MIPs in various fields. However, despite these significant accomplishments, there are still noteworthy challenges that need to be addressed before anisotropic MIPs can be effectively utilized in industrial or biomedical applications. Based on this review, several key conclusions and prospects can be derived.

In summarising the primary colloidal synthetic routes for obtaining 0D, 1D, and 2D MIPs, the synthesis methods and associated key parameters influencing the size and shape of the nanoparticles have been clearly identified. For the synthesis of 0D anisotropic nanoparticles, the focus lies on controlling nucleation and growth. Parameters such as precursor concentration, solvent polarity, reaction temperature, and the use of stabilizing agents or surfactants play critical roles in determining the size and shape of the nanoparticles. By carefully adjusting these parameters, researchers could achieve monodisperse 0D nanoparticles with desired shapes. For 1D nanoparticles, the synthesis methods aim to control the growth along one dimension while restricting growth in other directions. Common approaches include template-assisted synthesis, self-assembly or field-induced assembly, and directing agent-assisted anisotropic growth. Parameters such as the choice of template, field strength and homogeneity, size and shape of the building blocks, and the selection of directing agent significantly impact the formation of 1D morphologies, like nanorods or nanowires. In the case of 2D MIPs nanoparticles, the synthesis routes involve the nucleation and controlled growth of nanoparticles on specific crystallographic planes. Techniques such as thermal decomposition and hydrothermal methods show great potential in producing well-defined 2D structures. Parameters including precursor choice, solvent composition, temperature, and the presence of surfactants or ligands affect the synthesis process. However, liquid-phase exfoliation, while effective for scalable production of 2D materials, presents challenges in preparing 2D iron oxide-based materials. Overall, despite the significant progress and promising results reported in the field, scaling up the production of anisotropic magnetic iron oxide nanoparticles remains a major challenge. Many anisotropic nanomaterials have only been realized at the laboratory scale thus far. Addressing the scale-up challenge and further refining synthesis techniques are crucial for the successful utilization of anisotropic magnetic iron oxide nanoparticles in industrial applications. Additionally, exploring novel approaches and overcoming limitations in synthesizing 2D iron oxide materials will contribute to advancing this field.

In addition to the size and morphology, the surface chemistry of MIPs significantly influences their performance. Surface

modification of MIPs is essential for improving their stability in aqueous environments, enhancing compatibility with target molecules or cells, and enabling functionalization for specific applications. Surface modification can indeed regulate the interaction between MIPs and water molecules, which directly affects the relaxation of water protons and, consequently, their performance in MRI. By modifying the surface chemistry of MIPs, the affinity and interaction with water molecules can be fine-tuned, leading to improved MRI performance, as well as enhanced sensitivity and specificity of MIP-based MRI contrast agents. The surface chemistry of MIPs can be tailored to achieve specific properties, such as hydrophilicity or hydrophobicity, charge, or the presence of functional groups. These modifications impact the interactions between MIPs and their surroundings, including water molecules, target analytes, or biological entities. By carefully designing the surface chemistry, MIPs can exhibit selective binding and recognition capabilities, making them valuable tools in various applications, such as sensing, separation, and drug delivery. Given the importance of surface modification, although the choice of modification strategy is typically determined by the original ligand, regardless of the MIP's shape, we have described the most important and widely used modification strategies. Due to the broad range of materials that can be utilized for surface coating, it is critical to carry out a comprehensive investigation on the safety issues of modified MIPs on a case by case basis prior to their clinical application.

In the context of bio-applications, non-spherical MIPs, particularly 1D and 2D nanoparticles, have exhibited favorable attributes compared to their spherical counterparts. It is worth noting that when comparing experimental data, meticulous attention should be given to ensure that the particle pairs or groupings being examined possess similar surface area or volumetric values, equivalent magnetic properties, and are synthesized using identical synthetic approaches. By ensuring these factors are controlled, potential variations arising from other parameters can be minimized. The isolation of the specific impact of nanoparticle shape on bio-application performance, independent of other influential factors like particle size, polydispersity, stability (or clustering), and surface coating, presents an ongoing challenge. In the realm of MIPs-biological interactions, the comprehensive understanding of the shape-dependent performance is still incomplete, and the outcomes can sometimes be subject to controversy. Therefore, further comprehensive and fundamental studies are necessary to elucidate the precise role of nanoparticle shape and its impact on bio-applications. Currently, the lack of standardized protocols for analyzing certain properties presents a significant challenge in comparing results across different research groups in the field. Consequently, a major task for the scientific community involved in magnetic nanoparticles for biomedical applications should aim to collectively dedicate substantial efforts toward the development of standardized protocols. Such protocols would not only enable more meaningful comparisons of data but also play a pivotal role in facilitating the translation of MIPs from the bench side into the clinic.

This comprehensive and up-to-date review aims to provide researchers with an updated and comprehensive evaluation of anisotropic MIPs, focusing on their shape-dependent characteristic properties and bio-applications. By critically assessing the current state of knowledge, this review intends to stimulate and encourage rigorous interdisciplinary research at the interface of anisotropic MIP synthesis and biomedicine. The ultimate objective is to unlock the full potential of anisotropic MIPs in the realm of theranostics, where they can seamlessly integrate diagnostic and therapeutic functionalities to advance personalized medicine and improve patient outcomes. It is clear that substantial advances have been made in materials and their fundamental properties, but much more collaborative and standardization work is needed to calibrate the field and cement the ultimate aims of clinical application.

CRediT authorship contribution statement

Fuqiang Chang: Writing – review & editing, Writing – original draft, Visualization, Investigation, Conceptualization. **Gemma-Louise Davies:** Writing – review & editing, Supervision, Funding acquisition, Conceptualization.

Declaration of competing interest

The authors declare that they have no known competing financial interests or personal relationships that could have appeared to influence the work reported in this paper.

Data availability

No data was used for the research described in the article.

Acknowledgments

This work was supported by the Enginering and Physical Sciences Research Council [grant number EP/T026014/1].

References

[1] Wang W, Gaus K, Tilley RD, Gooding JJ. The impact of nanoparticle shape on cellular internalisation and transport: what do the different analysis methods tell us? Mater Horizons 2019;6:1538–47. https://doi.org/10.1039/C9MH00664H.
[2] Decuzzi P, Godin B, Tanaka T, Lee S-Y, Chiappini C, Liu X, et al. Size and shape effects in the biodistribution of intravascularly injected particles. J Control Release 2010;141:320–7. https://doi.org/10.1016/j.jconrel.2009.10.014.
[3] Meyer RA, Green JJ. Shaping the future of nanomedicine: anisotropy in polymeric nanoparticle design. WIREs Nanomed Nanobiotechnol 2016;8:191–207. https://doi.org/10.1002/wnan.1348.

[4] Williams DS, Pijpers IAB, Ridolfo R, van Hest JCM. Controlling the morphology of copolymeric vectors for next generation nanomedicine. J Control Release 2017;259:29–39. https://doi.org/10.1016/j.jconrel.2017.02.030.
[5] Yu Q, Roberts MG, Houdaihed L, Liu Y, Ho K, Walker G, et al. Investigating the influence of block copolymer micelle length on cellular uptake and penetration in a multicellular tumor spheroid model. Nanoscale 2021;13:280–91. https://doi.org/10.1039/D0NR08076D.
[6] Pokropivny VV, Skorokhod VV. Classification of nanostructures by dimensionality and concept of surface forms engineering in nanomaterial science. Mater Sci Eng C 2007;27:990–3. https://doi.org/10.1016/j.msec.2006.09.023.
[7] Nguyen MD, Tran H-V, Xu S, Lee TR. Fe3O4 nanoparticles: Structures, synthesis, magnetic properties, surface functionalization, and emerging applications. Appl Sci 2021;11:11301. https://doi.org/10.3390/app112311301.
[8] Bullivant J, Zhao S, Willenberg B, Kozissnik B, Batich C, Dobson J. Materials characterization of feraheme/ferumoxytol and preliminary evaluation of its potential for magnetic fluid hyperthermia. Int J Mol Sci 2013;14:17501–10. https://doi.org/10.3390/ijms140917501.
[9] Maldonado-Camargo L, Unni M, Rinaldi C. Magnetic characterization of iron oxide nanoparticles for biomedical applications. Biomed Nanotechnol Methods Protoc 2017:47–71.
[10] Zahn D, Landers J, Buchwald J, Diegel M, Salamon S, Müller R, et al. Ferrimagnetic large single domain iron oxide nanoparticles for hyperthermia applications. Nanomaterials 2022;12:343. https://doi.org/10.3390/nano12030343.
[11] Leslie-Pelecky DL, Rieke RD. Magnetic properties of nanostructured materials. Chem Mater 1996;8:1770–83. https://doi.org/10.1021/cm960077f.
[12] Shi D, Sadat ME, Dunn AW, Mast DB. Photo-fluorescent and magnetic properties of iron oxide nanoparticles for biomedical applications. Nanoscale 2015;7:8209–32. https://doi.org/10.1039/C5NR01538C.
[13] Xia Y, Chen Q, Banin U. Introduction: Anisotropic nanomaterials. Chem Rev 2023;123:3325–8. https://doi.org/10.1021/acs.chemrev.3c00092.
[14] Noh S, Na W, Jang J, Lee J-H, Lee EJ, Moon SH, et al. Nanoscale magnetism control via surface and exchange anisotropy for optimized ferrimagnetic hysteresis. Nano Lett 2012;12:3716–21. https://doi.org/10.1021/nl301499u.
[15] Lisjak D, Mertelj A. Anisotropic magnetic nanoparticles: A review of their properties, syntheses and potential applications. Prog Mater Sci 2018;95:286–328. https://doi.org/10.1016/j.pmatsci.2018.03.003.
[16] Ma Z, Mohapatra J, Wei K, Liu JP, Sun S. Magnetic nanoparticles: Synthesis, anisotropy, and applications. Chem Rev 2021. https://doi.org/10.1021/acs.chemrev.1c00860.
[17] Gupta MK, Kulkarni DD, Geryak R, Naik S, Tsukruk VV. A Robust and facile approach to assembling mobile and highly-open unfrustrated triangular lattices from ferromagnetic nanorods. Nano Lett 2013;13:36–42. https://doi.org/10.1021/nl303268s.
[18] Kalaiselvan CR, Laha SS, Somvanshi SB, Tabish TA, Thorat ND, Sahu NK. Manganese ferrite (MnFe2O4) nanostructures for cancer theranostics. Coord Chem Rev 2022;473:214809. https://doi.org/10.1016/j.ccr.2022.214809.
[19] Batley JT, Nguyen M, Kamboj I, Korostynski C, Aydil ES, Leighton C. Quantitative understanding of superparamagnetic blocking in thoroughly characterized ni nanoparticle assemblies. Chem Mater 2020;32:6494–506. https://doi.org/10.1021/acs.chemmater.0c01758.
[20] Yanes R, Chubykalo-Fesenko O, Kachkachi H, Garanin DA, Evans R, Chantrell RW. Effective anisotropies and energy barriers of magnetic nanoparticles with Néel surface anisotropy. Phys Rev B 2007;76:064416. https://doi.org/10.1103/PhysRevB.76.064416.
[21] Mahmoud WE, Al-Hazmi F, Al-Noaiser F, Al-Ghamdi AA, Bronstein LM. A facile method to syntheses monodisperse γ-Fe2O3 nanocubes with high magnetic anisotropy density. Superlattices Microstruct 2014;68:1–5. https://doi.org/10.1016/j.spmi.2014.01.009.
[22] Chalasani R, Vasudevan S. Form, content, and magnetism in iron oxide nanocrystals. J Phys Chem C 2011;115:18088–93.
[23] Vereda F, de Vicente J, Hidalgo-Álvarez R. Physical properties of elongated magnetic particles: Magnetization and friction coefficient anisotropies. ChemPhysChem 2009;10:1165–79. https://doi.org/10.1002/cphc.200900091.
[24] Mohapatra J, Xing M, Beatty J, Elkins J, Seda T, Mishra SR, et al. Enhancing the magnetic and inductive heating properties of Fe3O4 nanoparticles via morphology control. Nanotechnology 2020;31:275706. https://doi.org/10.1088/1361-6528/ab84a3.
[25] Mohapatra J, Mitra A, Tyagi H, Bahadur D, Aslam M. Iron oxide nanorods as high-performance magnetic resonance imaging contrast agents. Nanoscale 2015;7:9174–84. https://doi.org/10.1039/C5NR00055F.
[26] Carroll MRJ, Woodward RC, House MJ, Teoh WY, Amal R, Hanley TL, et al. Experimental validation of proton transverse relaxivity models for superparamagnetic nanoparticle MRI contrast agents. Nanotechnology 2010;21:035103. https://doi.org/10.1088/0957-4484/21/3/035103.
[27] Zheng X-Y, Sun L-D, Zheng T, Dong H, Li Y, Wang Y-F, et al. PAA-capped GdF3 nanoplates as dual-mode MRI and CT contrast agents. Sci Bull 2015;60:1092–100. https://doi.org/10.1007/s11434-015-0802-3.
[28] Jeon M, Halbert MV, Stephen ZR, Zhang M. Iron oxide nanoparticles as T1 contrast agents for magnetic resonance imaging: fundamentals, challenges, applications, and prospectives. Adv Mater 2021;33:1906539. https://doi.org/10.1002/adma.201906539.
[29] Roca AG, Gutiérrez L, Gavilán H, Fortes Brollo ME, Veintemillas-Verdaguer S, Morales Mdel P. Design strategies for shape-controlled magnetic iron oxide nanoparticles. Adv Drug Deliv Rev 2019;138:68–104. https://doi.org/10.1016/j.addr.2018.12.008.
[30] Elsayed WEM, Al-Hazmi FS, Memesh LS, Bronstein LM. A novel approach for rapid green synthesis of nearly mono-disperse iron oxide magnetic nanocubes with remarkable surface magnetic anisotropy density for enhancing hyperthermia performance. Colloids Surfaces A Physicochem Eng Asp 2017;529:239–45. https://doi.org/10.1016/j.colsurfa.2017.06.008.
[31] Castellanos-Rubio I, Arriortua O, Iglesias-Rojas D, Barón A, Rodrigo I, Marcano L, et al. A milestone in the chemical synthesis of Fe 3 O 4 nanoparticles: Unreported bulklike properties lead to a remarkable magnetic hyperthermia. Chem Mater 2021;33:8693–704. https://doi.org/10.1021/acs.chemmater.1c02654.
[32] Das R, Alonso J, Nemati Porshokouh Z, Kalappattil V, Torres D, Phan M-H, et al. Tunable high aspect ratio iron oxide nanorods for enhanced hyperthermia. J Phys Chem C 2016;120:10086–93. https://doi.org/10.1021/acs.jpcc.6b02006.
[33] Martinez-Boubeta C, Simeonidis K, Makridis A, Angelakeris M, Iglesias O, Guardia P, et al. Learning from nature to improve the heat generation of iron-oxide nanoparticles for magnetic hyperthermia applications. Sci Rep 2013;3:1652. https://doi.org/10.1038/srep01652.
[34] Nemati Z, Alonso J, Rodrigo I, Das R, Garaio E, García JÁ, et al. Improving the heating efficiency of iron oxide nanoparticles by tuning their shape and size. J Phys Chem C 2018;122:2367–81. https://doi.org/10.1021/acs.jpcc.7b10528.
[35] Mukhtar A, Cao X-M, Mehmood T, Wang D, Wu K. Structural characterization of self-assembled chain like Fe-FeOx Core shell nanostructure. Nanoscale Res Lett 2019;14:308. https://doi.org/10.1186/s11671-019-3128-2.
[36] Simeonidis K, Morales MP, Marciello M, Angelakeris M, de la Presa P, Lazaro-Carrillo A, et al. In-situ particles reorientation during magnetic hyperthermia application: Shape matters twice. Sci Rep 2016;6:38382. https://doi.org/10.1038/srep38382.
[37] Xu T, Yu J, Yan X, Choi H, Zhang L. Magnetic actuation based motion control for microrobots: An overview. Micromachines 2015;6:1346–64. https://doi.org/10.3390/mi6091346.
[38] Mannix RJ, Kumar S, Cassiola F, Montoya-Zavala M, Feinstein E, Prentiss M, et al. Nanomagnetic actuation of receptor-mediated signal transduction. Nat Nanotechnol 2008;3:36–40. https://doi.org/10.1038/nnano.2007.418.
[39] Lee SH, Kim BH, Park CG, Lee C, Lim BY, Bin Choy Y. Implantable small device enabled with magnetic actuation for on-demand and pulsatile drug delivery. J Control Release 2018;286:224–30. https://doi.org/10.1016/j.jconrel.2018.07.037.
[40] Golovin YI, Gribanovsky SL, Golovin DY, Klyachko NL, Majouga AG, Master AM, et al. Towards nanomedicines of the future: Remote magneto-mechanical actuation of nanomedicines by alternating magnetic fields. J Control Release 2015;219:43–60. https://doi.org/10.1016/j.jconrel.2015.09.038.
[41] Wang Y, Kohane DS. External triggering and triggered targeting strategies for drug delivery. Nat Rev Mater 2017;2:17020. https://doi.org/10.1038/natrevmats.2017.20.
[42] Naud C, Thébault C, Carrière M, Hou Y, Morel R, Berger F, et al. Cancer treatment by magneto-mechanical effect of particles, a review. Nanoscale Adv 2020;2:3632–55. https://doi.org/10.1039/D0NA00187B.
[43] Goiriena-Goikoetxea M, Muñoz D, Orue I, Fernández-Gubieda ML, Bokor J, Muela A, et al. Disk-shaped magnetic particles for cancer therapy. Appl Phys Rev 2020;7. https://doi.org/10.1063/1.5123716.

[44] Chen M, Wu J, Ning P, Wang J, Ma Z, Huang L, et al. Remote control of mechanical forces via mitochondrial-targeted magnetic nanospinners for efficient cancer treatment. Small 2020;16:1–14. https://doi.org/10.1002/smll.201905424.
[45] Golovin YI, Klyachko NL, Gribanovskii SL, Golovin DY, Samodurov AA, Majouga AG, et al. Nanomechanical control of properties of biological membranes achieved by rodlike magnetic nanoparticles in a superlow-frequency magnetic field. Tech Phys Lett 2015;41:455–7. https://doi.org/10.1134/S1063785015050065.
[46] Mishra SR, Tracy JB. Sequential actuation of shape-memory polymers through wavelength-selective photothermal heating of gold nanospheres and nanorods. ACS Appl Nano Mater 2018;1:3063–7. https://doi.org/10.1021/acsanm.8b00394.
[47] Rozanova N, Zhang J. Photothermal ablation therapy for cancer based on metal nanostructures. Sci China Ser B Chem 2009;52:1559–75. https://doi.org/10.1007/s11426-009-0247-0.
[48] Wang M, He L, Xu W, Wang X, Yin Y. Magnetic assembly and field-tuning of ellipsoidal-nanoparticle-based colloidal photonic crystals. Angew Chemie - Int Ed 2015;54:7077–81. https://doi.org/10.1002/anie.201501782.
[49] Dai Q, Bertleff-Zieschang N, Braunger JA, Björnmalm M, Cortez-Jugo C, Caruso F. Particle targeting in complex biological media. Adv Healthc Mater 2018;7:1700575. https://doi.org/10.1002/adhm.201700575.
[50] Zhu X, Vo C, Taylor M, Smith BR. Non-spherical micro- and nanoparticles in nanomedicine. Mater Horizons 2019;6:1094–121. https://doi.org/10.1039/C8MH01527A.
[51] Wanger G, Onstott TC, Southam G. Stars of the terrestrial deep subsurface: A novel 'star-shaped'bacterial morphotype from a South African platinum mine. Geobiology 2008;6:325–30.
[52] Young KD. Bacterial morphology: why have different shapes? Curr Opin Microbiol 2007;10:596–600.
[53] Young KD. The selective value of bacterial shape. Microbiol Mol Biol Rev 2006;70:660–703. https://doi.org/10.1128/MMBR.00001-06.
[54] Tao L, Hu W, Liu Y, Huang G, Sumer BD, Gao J. Shape-specific polymeric nanomedicine: emerging opportunities and challenges. Exp Biol Med 2011;236:20–9. https://doi.org/10.1258/ebm.2010.010243.
[55] Chan WCW. Nanomedicine 2.0. Acc Chem Res 2017;50:627–32. https://doi.org/10.1021/acs.accounts.6b00629.
[56] Yang L, Zhou Z, Song J, Chen X. Anisotropic nanomaterials for shape-dependent physicochemical and biomedical applications. Chem Soc Rev 2019;48:5140–76. https://doi.org/10.1039/C9CS00011A.
[57] Kaittanis C, Santra S, Perez JM. Role of nanoparticle valency in the nondestructive magnetic-relaxation-mediated detection and magnetic isolation of cells in complex media. J Am Chem Soc 2009;131:12780–91. https://doi.org/10.1021/ja9041077.
[58] Akhtar MJ, Ahamed M, Alhadlaq HA. Challenges facing nanotoxicology and nanomedicine due to cellular diversity. Clin Chim Acta 2018;487:186–96. https://doi.org/10.1016/j.cca.2018.10.004.
[59] Duan X, Li Y. Physicochemical characteristics of nanoparticles affect circulation, biodistribution, cellular internalization, and trafficking. Small 2013;9:1521–32. https://doi.org/10.1002/smll.201201390.
[60] Geng Y, Dalhaimer P, Cai S, Tsai R, Tewari M, Minko T, et al. Shape effects of filaments versus spherical particles in flow and drug delivery. Nat Nanotechnol 2007;2:249–55. https://doi.org/10.1038/nnano.2007.70.
[61] Zhao Y, Wang Y, Ran F, Cui Y, Liu C, Zhao Q, et al. A comparison between sphere and rod nanoparticles regarding their in vivo biological behavior and pharmacokinetics. Sci Rep 2017;7:4131. https://doi.org/10.1038/s41598-017-03834-2.
[62] Erol O, Uyan I, Hatip M, Yilmaz C, Tekinay AB, Guler MO. Recent advances in bioactive 1D and 2D carbon nanomaterials for biomedical applications. Nanomedicine Nanotechnology Biol Med 2018;14:2433–54.
[63] Nguyen EP, Silva Cde CC, Merkoçi A. Recent advancement in biomedical applications on the surface of two-dimensional materials: From biosensing to tissue engineering. Nanoscale 2020;12:19043–67.
[64] Wang X, Han X, Li C, Chen Z, Huang H, Chen J, et al. 2D materials for bone therapy. Adv Drug Deliv Rev 2021;178:113970.
[65] Chen S, Li R, Li X, Xie J. Electrospinning: An enabling nanotechnology platform for drug delivery and regenerative medicine. Adv Drug Deliv Rev 2018;132:188–213.
[66] de Carvalho JF, de Medeiros SN, Morales MA, Dantas AL, Carriço AS. Synthesis of magnetite nanoparticles by high energy ball milling. Appl Surf Sci 2013;275:84–7. https://doi.org/10.1016/j.apsusc.2013.01.118.
[67] Agarwal P, Bora DK. Fast sonochemical exfoliation of Hematene type sheets and flakes from hematite nanoarchitectures shows enhanced photocurrent density. J Mater Res 2022;37:3428–44. https://doi.org/10.1557/s43578-022-00651-w.
[68] Huang J, Liu X, Chen G, Zhang N, Ma R, Qiu G. Selective fabrication of porous iron oxides hollow spheres and nanofibers by electrospinning for photocatalytic water purification. Solid State Sci 2018;82:24–8. https://doi.org/10.1016/j.solidstatesciences.2018.05.014.
[69] Zhang Z, Wells CJR, King AM, Bear JC, Davies GL, Williams GR. PH-Responsive nanocomposite fibres allowing MRI monitoring of drug release. J Mater Chem B 2020;8:7264–74. https://doi.org/10.1039/d0tb01033b.
[70] King AM, Bray C, Hall SCL, Bear JC, Bogart LK, Perrier S, et al. Exploring precision polymers to fine-tune magnetic resonance imaging properties of iron oxide nanoparticles. J Colloid Interface Sci 2020;579:401–11. https://doi.org/10.1016/j.jcis.2020.06.036.
[71] Ternent L, Mayoh DA, Lees MR, Davies G-L. Heparin-stabilised iron oxide for MR applications: a relaxometric study. J Mater Chem B 2016;4:3065–74. https://doi.org/10.1039/C6TB00832A.
[72] Baig N, Kammakakam I, Falath W. Nanomaterials: a review of synthesis methods, properties, recent progress, and challenges. Mater Adv 2021;2:1821–71. https://doi.org/10.1039/D0MA00807A.
[73] Nikam AV, Prasad BLV, Kulkarni AA. Wet chemical synthesis of metal oxide nanoparticles: a review. CrstEngComm 2018;20:5091–107. https://doi.org/10.1039/C8CE00487K.
[74] Lu S, Li X, Zhang J, Peng C, Shen M, Shi X. Dendrimer-stabilized gold nanoflowers embedded with ultrasmall iron oxide nanoparticles for multimode imaging-guided combination therapy of tumors. Adv Sci 2018;5:1801612. https://doi.org/10.1002/advs.201801612.
[75] Ling D, Lee N, Hyeon T. Chemical synthesis and assembly of uniformly sized iron oxide nanoparticles for medical applications. Acc Chem Res 2015;48:1276–85. https://doi.org/10.1021/acs.accounts.5b00038.
[76] Wang M, He L, Yin Y. Magnetic field guided colloidal assembly. Mater Today 2013;16:110–6. https://doi.org/10.1016/j.mattod.2013.04.008.
[77] Lai J, Niu W, Luque R, Xu G. Solvothermal synthesis of metal nanocrystals and their applications. Nano Today 2015;10:240–67. https://doi.org/10.1016/j.nantod.2015.03.001.
[78] Hu Y, Mignani S, Majoral J-P, Shen M, Shi X. Construction of iron oxide nanoparticle-based hybrid platforms for tumor imaging and therapy. Chem Soc Rev 2018;47:1874–900. https://doi.org/10.1039/C7CS00657H.
[79] Hufschmid R, Arami H, Ferguson RM, Gonzales M, Teeman E, Brush LN, et al. Synthesis of phase-pure and monodisperse iron oxide nanoparticles by thermal decomposition. Nanoscale 2015;7:11142–54.
[80] Abebe B, Tsegaye D, Ananda Murthy HC. Insight into nanocrystal synthesis: from precursor decomposition to combustion. RSC Adv 2022;12:24374–89. https://doi.org/10.1039/D2RA05222A.
[81] Ding B, Zheng P, Ma P, Lin J. Manganese oxide nanomaterials: Synthesis, Properties, and theranostic applications. Adv Mater 2020;32:1905823. https://doi.org/10.1002/adma.201905823.
[82] Woo K, Hong J, Choi S, Lee H-W, Ahn J-P, Kim CS, et al. Easy synthesis and magnetic properties of iron oxide nanoparticles. Chem Mater 2004;16:2814–8. https://doi.org/10.1021/cm049552x.
[83] Park J, An K, Hwang Y, Park J-G, Noh H-J, Kim J-Y, et al. Ultra-large-scale syntheses of monodisperse nanocrystals. Nat Mater 2004;3:891–5. https://doi.org/10.1038/nmat1251.
[84] Feld A, Weimer A, Kornowski A, Winckelmans N, Merkl J-P, Kloust H, et al. Chemistry of shape-controlled iron oxide nanocrystal formation. ACS Nano 2019;13:152–62. https://doi.org/10.1021/acsnano.8b05032.

[85] Sun S, Zeng H, Robinson DB, Raoux S, Rice PM, Wang SX, et al. Monodisperse MFe 2 O 4 (M = Fe Co, Mn) nanoparticles. J Am Chem Soc 2004;126:273–9. https://doi.org/10.1021/ja0380852.
[86] Andreu I, Natividad E, Solozábal L, Roubeau O. Nano-objects for addressing the control of nanoparticle arrangement and performance in magnetic hyperthermia. ACS Nano 2015;9:1408–19. https://doi.org/10.1021/nn505781f.
[87] Urbach ZJ, Park SS, Weigand SL, Rix JE, Lee B, Mirkin CA. Probing the consequences of cubic particle shape and applied field on colloidal crystal engineering with DNA. Angew Chemie 2021;133:4111–5. https://doi.org/10.1002/ange.202012907.
[88] Reguera J, Jiménez de Aberasturi D, Henriksen-Lacey M, Langer J, Espinosa A, Szczupak B, et al. Janus plasmonic–magnetic gold–iron oxide nanoparticles as contrast agents for multimodal imaging. Nanoscale 2017;9:9467–80. https://doi.org/10.1039/C7NR01406F.
[89] Bronstein LM, Huang X, Retrum J, Schmucker A, Pink M, Stein BD, et al. Influence of iron oleate complex structure on iron oxide nanoparticle formation. Chem Mater 2007;19:3624–32.
[90] Kwon SG, Piao Y, Park J, Angappane S, Jo Y, Hwang N-M, et al. Kinetics of monodisperse iron oxide nanocrystal formation by "heating-up" process. J Am Chem Soc 2007;129:12571–84.
[91] Guardia P, Di Corato R, Lartigue L, Wilhelm C, Espinosa A, Garcia-Hernandez M, et al. Water-soluble iron oxide nanocubes with high values of specific absorption rate for cancer cell hyperthermia treatment. ACS Nano 2012;6:3080–91. https://doi.org/10.1021/nn2048137.
[92] Kim BH, Lee N, Kim H, An K, Il Park Y, Choi Y, et al. Large-scale synthesis of uniform and extremely small-sized iron oxide nanoparticles for high-resolution t 1 magnetic resonance imaging contrast agents. J Am Chem Soc 2011;133:12624–31. https://doi.org/10.1021/ja203340u.
[93] Cooper SR, Plummer LK, Cosby AG, Lenox P, Jander A, Dhagat P, et al. Insights into the magnetic properties of sub-10 nm iron oxide nanocrystals through the use of a continuous growth synthesis. Chem Mater 2018;30:6053–62.
[94] Zhao Z, Zhou Z, Bao J, Wang Z, Hu J, Chi X, et al. Octapod iron oxide nanoparticles as high-performance T 2 contrast agents for magnetic resonance imaging. Nat Commun 2013;4. https://doi.org/10.1038/ncomms3266.
[95] Kovalenko MV, Bodnarchuk MI, Lechner RT, Hesser G, Schäffler F, Heiss W. Fatty acid salts as stabilizers in size-and shape-controlled nanocrystal synthesis: the case of inverse spinel iron oxide. J Am Chem Soc 2007;129:6352–3.
[96] Hai HT, Yang HT, Kura H, Hasegawa D, Ogata Y, Takahashi M, et al. Size control and characterization of wustite (core)/spinel (shell) nanocubes obtained by decomposition of iron oleate complex. J Colloid Interface Sci 2010;346:37–42. https://doi.org/10.1016/j.jcis.2010.02.025.
[97] Cotin G, Blanco-Andujar C, Perton F, Asín L, Jesus M, Reichardt W, et al. Unveiling the role of surface, size, shape and defects of iron oxide nanoparticles for theranostic applications. Nanoscale 2021;13:14552–71.
[98] Khurshid H, Li W, Chandra S, Phan M-H, Hadjipanayis GC, Mukherjee P, et al. Mechanism and controlled growth of shape and size variant core/shell FeO/Fe3O4 nanoparticles. Nanoscale 2013;5:7942. https://doi.org/10.1039/c3nr02596a.
[99] Cotin G, Kiefer C, Perton F, Ihiawakrim D, Blanco-Andujar C, Moldovan S, et al. Unravelling the thermal decomposition parameters for the synthesis of anisotropic iron oxide nanoparticles. Nanomaterials 2018;8:881.
[100] Muro-Cruces J, Roca AG, López-Ortega A, Fantechi E, Del-Pozo-Bueno D, Estradé S, et al. Precise size control of the growth of Fe3O4 nanocubes over a wide size range using a rationally designed one-pot synthesis. ACS Nano 2019;13:7716–28. https://doi.org/10.1021/acsnano.9b01281.
[101] Qiao L, Fu Z, Li J, Ghosen J, Zeng M, Stebbins J, et al. Standardizing size- and shape-controlled synthesis of monodisperse magnetite (Fe3O4) nanocrystals by identifying and exploiting effects of organic impurities. ACS Nano 2017;11:6370–81. https://doi.org/10.1021/acsnano.7b02752.
[102] Xie J, Yan C, Zhang Y, Gu N. Shape evolution of "Multibranched" Mn–Zn ferrite nanostructures with high performance: A transformation of nanocrystals into nanoclusters. Chem Mater 2013;25:3702–9. https://doi.org/10.1021/cm402036d.
[103] Singh G, Myasnichenko VS, Glomm WR. New insights into size-controlled reproducible synthesis of anisotropic Fe3O4 nanoparticles: the importance of the reaction environment. Mater Adv 2020;1:1077–82. https://doi.org/10.1039/D0MA00275E.
[104] Pichon BP, Gerber O, Lefevre C, Florea I, Fleutot S, Baaziz W, et al. Microstructural and magnetic investigations of wüstite-spinel core-shell cubic-shaped nanoparticles. Chem Mater 2011;23:2886–900. https://doi.org/10.1021/cm2003319.
[105] Xia Y, Gilroy KD, Peng H, Xia X. Seed-mediated growth of colloidal metal nanocrystals. Angew Chemie Int Ed 2017;56:60–95. https://doi.org/10.1002/anie.201604731.
[106] Salas G, Costo R, del M, Morales P. Synthesis of inorganic nanoparticles. Front Nanosci 2012:35–79. https://doi.org/10.1016/B978-0-12-415769-9.00002-9.
[107] Hodges JM, Morse JR, Fenton JL, Ackerman JD, Alameda LT, Schaak RE. Insights into the seeded-growth synthesis of colloidal hybrid nanoparticles. Chem Mater 2017;29:106–19. https://doi.org/10.1021/acs.chemmater.6b02795.
[108] Hodges JM, Biacchi AJ, Schaak RE. Ternary hybrid nanoparticle isomers: Directing the nucleation of Ag on Pt-Fe3O4 using a solid-state protecting group. ACS Nano 2014;8:1047–55. https://doi.org/10.1021/nn405943z.
[109] Hodges JM, Morse JR, Williams ME, Schaak RE. Microscopic investigation of chemoselectivity in Ag-Pt-Fe3O4 heterotrimer formation: Mechanistic insights and implications for controlling high-order hybrid nanoparticle morphology. J Am Chem Soc 2015;137:15493–500. https://doi.org/10.1021/jacs.5b10254.
[110] Read CG, Gordon TR, Hodges JM, Schaak RE. Colloidal hybrid nanoparticle insertion reaction for transforming heterodimers into heterotrimers. J Am Chem Soc 2015;137:12514–7. https://doi.org/10.1021/jacs.5b08850.
[111] Levy M, Quarta A, Espinosa A, Figuerola A, Wilhelm C, García-Hernández M, et al. Correlating magneto-structural properties to hyperthermia performance of highly monodisperse iron oxide nanoparticles prepared by a seeded-growth route. Chem Mater 2011;23:4170–80. https://doi.org/10.1021/cm201078f.
[112] Zhang Q, Zhang L, Li S, Chen X, Zhang M, Wang T, et al. Designed synthesis of Au/Fe 3 O 4 @C janus nanoparticles for dual-modal imaging and actively targeted chemo-photothermal synergistic therapy of cancer cells. Chem - A Eur J 2017;23:17242–8. https://doi.org/10.1002/chem.201703498.
[113] Deka K, Guleria A, Kumar D, Biswas J, Lodha S, Kaushik SD, et al. Janus nanoparticles for contrast enhancement of T 1 -T 2 dual mode magnetic resonance imaging. Dalt Trans 2019;48:1075–83. https://doi.org/10.1039/c8dt04038a.
[114] Figuerola A, Fiore A, Di Corato R, Falqui A, Giannini C, Micotti E, et al. One-pot synthesis and characterization of size-controlled bimagnetic FePt−Iron oxide heterodimer nanocrystals. J Am Chem Soc 2008;130:1477–87. https://doi.org/10.1021/ja078034v.
[115] Zhang H, Yang Z, Ju Y, Chu X, Ding Y, Huang X, et al. Galvanic displacement synthesis of monodisperse janus- and satellite-like plasmonic-magnetic Ag-Fe@Fe3O4 heterostructures with reduced cytotoxicity. Adv Sci 2018;5:1800271. https://doi.org/10.1002/advs.201800271.
[116] Zeng J, Gong M, Wang D, Li M, Xu W, Li Z, et al. Direct synthesis of water-dispersible magnetic/plasmonic heteronanostructures for multimodality biomedical imaging. Nano Lett 2019;19:3011–8. https://doi.org/10.1021/acs.nanolett.9b00171.
[117] Jiang J, Gu H, Shao H, Devlin E, Papaefthymiou GC, Ying JY. Bifunctional Fe3O4–Ag heterodimer nanoparticles for two-photon fluorescence imaging and magnetic manipulation. Adv Mater 2008;20:4403–7.
[118] Song G, Chen M, Zhang Y, Cui L, Qu H, Zheng X, et al. Janus iron oxides@ semiconducting polymer nanoparticle tracer for cell tracking by magnetic particle imaging. Nano Lett 2018;18:182–9.
[119] Sun H, Chen B, Jiao X, Jiang Z, Qin Z, Chen D. Solvothermal synthesis of tunable electroactive magnetite nanorods by controlling the side reaction. J Phys Chem C 2012;116:5476–81. https://doi.org/10.1021/jp211986a.
[120] Orza A, Wu H, Xu Y, Lu Q, Mao H. One-step facile synthesis of highly magnetic and surface functionalized iron oxide nanorods for biomarker-targeted applications. ACS Appl Mater Interfaces 2017;9:20719–27. https://doi.org/10.1021/acsami.7b02575.
[121] Palchoudhury S, An W, Xu Y, Qin Y, Zhang Z, Chopra N, et al. Synthesis and growth mechanism of iron oxide nanowhiskers. Nano Lett 2011;11:1141–6. https://doi.org/10.1021/nl200136j.
[122] Bao L, Low W-L, Jiang J, Ying JY. Colloidal synthesis of magnetic nanorods with tunable aspect ratios. J Mater Chem 2012;22:7117. https://doi.org/10.1039/c2jm16401a.
[123] Rajan A, Sahu NK. Hydrophobic-to-hydrophilic transition of Fe 3 O 4 nanorods for magnetically induced hyperthermia. ACS Appl Nano Mater 2021;4:4642–53. https://doi.org/10.1021/acsanm.1c00274.
[124] Wan J, Chen X, Wang Z, Yang X, Qian Y. A soft-template-assisted hydrothermal approach to single-crystal Fe 3O4 nanorods. J Cryst Growth 2005;276:571–6. https://doi.org/10.1016/j.jcrysgro.2004.11.423.

[125] Huang Z, Zhang Y, Tang F. Solution-phase synthesis of single-crystalline magnetic nanowires with high aspect ratio and uniformity. Chem Commun 2005: 342–4. https://doi.org/10.1039/b410463c.
[126] Liu L, Kou H-Z, Mo W, Liu H, Wang Y. Surfactant-assisted synthesis of α-Fe2O3 nanotubes and nanorods with shape-dependent magnetic properties. J Phys Chem B 2006;110:15218–23.
[127] Poolakkandy RR, Menamparambath MM. Soft-template-assisted synthesis: a promising approach for the fabrication of transition metal oxides. Nanoscale Adv 2020;2:5015–45. https://doi.org/10.1039/D0NA00599A.
[128] He K, Xu CY, Zhen L, Shao WZ. Hydrothermal synthesis and characterization of single-crystalline Fe3O4 nanowires with high aspect ratio and uniformity. Mater Lett 2007;61:3159–62. https://doi.org/10.1016/j.matlet.2006.11.023.
[129] Kloust H, Zierold R, Merkl J-P, Schmidtke C, Feld A, Pöselt E, et al. Synthesis of iron oxide nanorods using a template mediated approach. Chem Mater 2015; 27:4914–7. https://doi.org/10.1021/acs.chemmater.5b00513.
[130] Yuan J, Xu Y, Müller AHEE. One-dimensional magnetic inorganic–organic hybrid nanomaterials. Chem Soc Rev 2011;40:640. https://doi.org/10.1039/c0cs00087f.
[131] Ma S, Jia W, Tong X, Yang Y, Zhang X, Yao T, et al. A simple approach for synthesis of hollow mesoporous nanotubes loaded with metallic and magnetic nanoparticles: Only one step is required. Appl Organomet Chem 2019;33:e4849. https://doi.org/10.1002/aoc.4849.
[132] Hurst SJ, Payne EK, Qin L, Mirkin CA. Multisegmented one-dimensional nanorods prepared by hard-template synthetic methods. Angew Chemie - Int Ed 2006; 45:2672–92. https://doi.org/10.1002/anie.200504025.
[133] Prina-Mello A, Whelan AM, Atzberger A, McCarthy JE, Byrne F, Davies G-L, et al. Comparative flow cytometric analysis of immunofunctionalized nanowire and nanoparticle signatures. Small 2010;6:247–55. https://doi.org/10.1002/smll.200901014.
[134] Gu L, Cao X, Mukhtar A, Wu K. Structural characterization and magnetic properties of core–shell Fe@Fe3O4 nanowires. Appl Phys A 2020;126:458. https://doi.org/10.1007/s00339-020-03644-w.
[135] Sun Y, Yan C, Xie J, Yan D, Hu K, Huang S, et al. High-performance worm-like Mn-Zn ferrite theranostic nanoagents and the application on tumor theranostics. ACS Appl Mater Interfaces 2019;11:29536–48. https://doi.org/10.1021/acsami.9b08948.
[136] Xiong F, Tian J, Hu K, Zheng X, Sun J, Yan C, et al. Superparamagnetic anisotropic nano-assemblies with longer blood circulation in vivo: a highly efficient drug delivery carrier for leukemia therapy. Nanoscale 2016;8:17085–9.
[137] Zhao N, Yan L, Xue J, Zhang K, Xu F. Degradable one-dimensional dextran-iron oxide nanohybrids for MRI-guided synergistic gene/photothermal/magnetolytic therapy. Nano Today 2021;38:101118. https://doi.org/10.1016/j.nantod.2021.101118.
[138] Chen L, Su B, Jiang L. Recent advances in one-dimensional assembly of nanoparticles. Chem Soc Rev 2019;48:8–21. https://doi.org/10.1039/c8cs00703a.
[139] Zhang W, Si X, Liu B, Bian G, Qi Y, Yang X, et al. Synthesis of 1D Fe3O4/P(MBAAm-co-MAA) nanochains as stabilizers for Ag nanoparticles and templates for hollow mesoporous structure, and their applications in catalytic reaction and drug delivery. J Colloid Interface Sci 2015;456:145–54. https://doi.org/10.1016/j.jcis.2015.06.028.
[140] Wang S, Fu J, Wang K, Gao M, Zhu J, Wang X, et al. Large-scale preparation of Fe@Fe2O3 nanoscale stirring bars with ultrahigh saturation magnetization. Mater Lett 2017;209:576–80. https://doi.org/10.1016/j.matlet.2017.08.103.
[141] King AM, Insinna T, Wells CJR, Raby IA, Gun'ko YK, Davies G. Magnetically driven preparation of 1-D nano-necklaces capable of MRI relaxation enhancement. Nanoscale Adv 2023;5:3209–13. https://doi.org/10.1039/D3NA00137G.
[142] Mehdizadeh Taheri S, Michaelis M, Friedrich T, Förster B, Drechsler M, Römer FM, et al. Self-assembly of smallest magnetic particles. Proc Natl Acad Sci 2015; 112:14484–9. https://doi.org/10.1073/pnas.1511443112.
[143] Singh G, Chan H, Baskin A, Gelman E, Repnin N, Kral P, et al. Self-assembly of magnetite nanocubes into helical superstructures. Science (80-) 2014;345: 1149–53. https://doi.org/10.1126/science.1254132.
[144] Ding X, Bao L, Jiang J, Gu H. Colloidal synthesis of ultrathin γ-Fe2O3 nanoplates. RSC Adv 2014;4:9314. https://doi.org/10.1039/c3ra46728g.
[145] Palchoudhury S, Xu Y, Rushdi A, Holler RA, Bao Y. Controlled synthesis of iron oxide nanoplates and nanoflowers. Chem Commun 2012;48:10499–501.
[146] Wei R, Zhou T, Sun C, Lin H, Yang L, Ren BW, et al. Iron-oxide-based twin nanoplates with strong T 2 relaxation shortening for contrast-enhanced magnetic resonance imaging. Nanoscale 2018;10:18398–406. https://doi.org/10.1039/C8NR04995E.
[147] Wang H, Shrestha TB, Basel MT, Pyle M, Toledo Y, Konecny A, et al. Hexagonal magnetite nanoprisms: preparation, characterization and cellular uptake. J Mater Chem B 2015;3:4647–53.
[148] Li J, Shi X, Shen M. Hydrothermal synthesis and functionalization of iron oxide nanoparticles for MR imaging applications. Part Part Syst Charact 2014;31: 1223–37. https://doi.org/10.1002/ppsc.201400087.
[149] Wang F, Qin XF, Meng YF, Guo ZL, Yang LX, Ming YF. Hydrothermal synthesis and characterization of α-Fe2O3 nanoparticles. Mater Sci Semicond Process 2013;16:802–6. https://doi.org/10.1016/j.mssp.2012.12.029.
[150] Qu J, Yu Y, Cao C-Y, Song W-G. α-Fe 2 O 3 Nanodisks: Layered structure, growth mechanism, and enhanced photocatalytic property. Chem - A Eur J 2013;19: 11172–7. https://doi.org/10.1002/chem.201301295.
[151] Li X, Si Z, Lei Y, Tang J, Wang S, Su S, et al. Direct hydrothermal synthesis of single-crystalline triangular Fe3O4 nanoprisms. CrstEngComm 2010;12:2060. https://doi.org/10.1039/b926780h.
[152] Zhou X, Shi Y, Ren L, Bao S, Han Y, Wu S, et al. Controllable synthesis, magnetic and biocompatible properties of Fe3O4 and α-Fe2O3 nanocrystals. J Solid State Chem 2012;196:138–44. https://doi.org/10.1016/j.jssc.2012.05.025.
[153] Chen L, Yang X, Chen J, Liu J, Wu H, Zhan H, et al. Continuous shape- and spectroscopy-tuning of hematite nanocrystals. Inorg Chem 2010;49:8411–20. https://doi.org/10.1021/ic100919a.
[154] Yang Y, Liu X, Lv Y, Herng TS, Xu X, Xia W, et al. Orientation mediated enhancement on magnetic hyperthermia of Fe3O4 nanodisc. Adv Funct Mater 2015;25: 812–20. https://doi.org/10.1002/adfm.201402764.
[155] Ma M, Zhang Y, Guo Z, Gu N. Facile synthesis of ultrathin magnetic iron oxide nanoplates by Schikorr reaction. Nanoscale Res Lett 2013;8:1–7.
[156] Yi M, Shen Z. A review on mechanical exfoliation for the scalable production of graphene. J Mater Chem A 2015;3:11700–15. https://doi.org/10.1039/C5TA00252D.
[157] Nicolosi V, Chhowalla M, Kanatzidis MG, Strano MS, Coleman JN. Liquid exfoliation of layered materials. Science 2013;340:72–5. https://doi.org/10.1126/science.1226419.
[158] Coleman JN, Lotya M, O'Neill A, Bergin SD, King PJ, Khan U, Young K, Gaucher A, De S, Smith RJ, Shvets IV, Arora SK, Stanton G, Kim H-Y, Lee K, Kim GT, Duesberg GS, Hallam T, Boland JJ, Wang JJ, Donegan JF, Grunlan JC, Moriarty G, Shmeliov A, Nicholls RJ, Perkins JM, Grieveson EM, Theuwissen K, McComb DW, Nellist PD, Nicolosi V. Two-dimensional nanosheets produced by liquid exfoliation of layered materials. Science 2011;331:568–71. https://doi.org/10.1126/science.1194975.
[159] Ambrosi A, Pumera M. Exfoliation of layered materials using electrochemistry. Chem Soc Rev 2018;47:7213–24. https://doi.org/10.1039/C7CS00811B.
[160] Yusuf M, Kumar M, Khan MA, Sillanpää M, Arafat H. A review on exfoliation, characterization, environmental and energy applications of graphene and graphene-based composites. Adv Colloid Interface Sci 2019;273:102036. https://doi.org/10.1016/j.cis.2019.102036.
[161] Dong J, Liu L, Tan C, Xu Q, Zhang J, Qiao Z, et al. Free-standing homochiral 2D monolayers by exfoliation of molecular crystals. Nature 2022;602:606–11. https://doi.org/10.1038/s41586-022-04407-8.
[162] Antwi-Baah R, Wang Y, Chen X, Liu H, Yu K. Hybrid morphologies of paramagnetic manganese-based nanoparticles as theranostics. Chem Eng J 2023;466: 142970. https://doi.org/10.1016/j.cej.2023.142970.
[163] Puthirath Balan A, Radhakrishnan S, Woellner CF, Sinha SK, Deng L, Reyes CDL, et al. Exfoliation of a non-van der Waals material from iron ore hematite. Nat Nanotechnol 2018;13:602–9. https://doi.org/10.1038/s41565-018-0134-y.
[164] Chahal S, Kauzlarich SM, Kumar P. Microwave synthesis of hematene and other two-dimensional oxides. ACS Mater Lett 2021;3:631–40. https://doi.org/10.1021/acsmaterialslett.1c00102.

[165] Mohapatra J, Ramos A, Elkins J, Beatty J, Xing M, Singh D, La Plante EC, Ping Liu J, et al. Ferromagnetism in 2D α-Fe 2 O 3 nanosheets. Appl Phys Lett 2021; 118:183102. https://doi.org/10.1063/5.0045366.
[166] Mohanty B, Wei Y, Ghorbani-Asl M, Krasheninnikov AV, Rajput P, Jena BK. Revealing the defect-dominated oxygen evolution activity of hematene. J Mater Chem A 2020;8:6709–16. https://doi.org/10.1039/D0TA00422G.
[167] Bandyopadhyay A, Frey NC, Jariwala D, Shenoy VB. Engineering magnetic phases in two-dimensional non-van der waals transition-metal oxides. Nano Lett 2019;19:7793–800. https://doi.org/10.1021/acs.nanolett.9b02801.
[168] Jin C, Kou L. Two-dimensional non-van der Waals magnetic layers: functional materials for potential device applications. J Phys D Appl Phys 2021;54:413001. https://doi.org/10.1088/1361-6463/ac08ca.
[169] Gavilán H, Rizzo GMR, Silvestri N, Mai BT, Pellegrino T. Scale-up approach for the preparation of magnetic ferrite nanocubes and other shapes with benchmark performance for magnetic hyperthermia applications. Nat Protoc 2023;18:783–809. https://doi.org/10.1038/s41596-022-00779-3.
[170] Besenhard MO, LaGrow AP, Famiani S, Pucciarelli M, Lettieri P, Thanh NTK, et al. Continuous production of iron oxide nanoparticles via fast and economical high temperature synthesis, React. Chem Eng 2020;5:1474–83. https://doi.org/10.1039/D0RE00078G.
[171] Mahin J, Torrente-Murciano L. Continuous synthesis of monodisperse iron@iron oxide core@shell nanoparticles. Chem Eng J 2020;396:125299. https://doi.org/10.1016/j.cej.2020.125299.
[172] Besenhard MO, Storozhuk L, LaGrow AP, Panariello L, Maney A, Pal S, et al. High temperature flow synthesis of iron oxide nanoparticles: Size tuning via reactor engineering. Chem Eng J 2023;473:144542. https://doi.org/10.1016/j.cej.2023.144542.
[173] McCarthy SA, Davies G-L, Gun'ko YK. Preparation of multifunctional nanoparticles and their assemblies. Nat Protoc 2012;7:1677–93. https://doi.org/10.1038/nprot.2012.082.
[174] Narkhede AA, Sherwood JA, Antone A, Coogan KR, Bolding MS, Deb S, et al. Role of surface chemistry in mediating the uptake of ultrasmall iron oxide nanoparticles by cancer cells. ACS Appl Mater Interfaces 2019;11:17157–66. https://doi.org/10.1021/acsami.9b00606.
[175] Du C, Liu X, Hu H, Li H, Yu L, Geng D, et al. Dual-targeting and excretable ultrasmall SPIONs for T 1 -weighted positive MR imaging of intracranial glioblastoma cells by targeting the lipoprotein receptor-related protein. J Mater Chem B 2020;8:2296–306. https://doi.org/10.1039/C9TB02391G.
[176] Ramos-Guivar JA, López EO, Greneche J-M, Jochen Litterst F, Passamani EC. Effect of EDTA organic coating on the spin canting behavior of maghemite nanoparticles for lead (II) adsorption. Appl Surf Sci 2021;538:148021. https://doi.org/10.1016/j.apsusc.2020.148021.
[177] Sathish S, Balakumar S. Influence of physicochemical interactions of capping agent on magnetic properties of magnetite nanoparticles. Mater Chem Phys 2016; 173:364–71. https://doi.org/10.1016/j.matchemphys.2016.02.024.
[178] Kandasamy G, Maity D. Recent advances in superparamagnetic iron oxide nanoparticles (SPIONs) for in vitro and in vivo cancer nanotheranostics. Int J Pharm 2015;496:191–218. https://doi.org/10.1016/j.ijpharm.2015.10.058.
[179] Roca AG, Niznansky D, Poltierova-Vejpravova J, Bittova B, González-Fernández MA, Serna CJ, et al. Magnetite nanoparticles with no surface spin canting. J Appl Phys 2009;105:114309. https://doi.org/10.1063/1.3133228.
[180] Daou TJ, Grenèche JM, Pourroy G, Buathong S, Derory A, Ulhaq-Bouillet C, et al. Coupling agent effect on magnetic properties of functionalized magnetite-based nanoparticles. Chem Mater 2008;20:5869–75. https://doi.org/10.1021/cm801405n.
[181] Harman CLG, Mac Fhionnlaoich N, King AM, Manning JRH, Lin W, Scholes P, et al. Controlled synthesis of SPION@SiO 2 nanoparticles using design of experiments. Mater Adv 2022;3:6007–18. https://doi.org/10.1039/D2MA00369D.
[182] Veiseh O, Gunn JW, Zhang M. Design and fabrication of magnetic nanoparticles for targeted drug delivery and imaging. Adv Drug Deliv Rev 2010;62:284–304. https://doi.org/10.1016/j.addr.2009.11.002.
[183] Lu C, Han L, Wang J, Wan J, Song G, Rao J. Engineering of magnetic nanoparticles as magnetic particle imaging tracers. Chem Soc Rev 2021;50:8102–46. https://doi.org/10.1039/d0cs00260g.
[184] Lee N, Hyeon T. Designed synthesis of uniformly sized iron oxide nanoparticles for efficient magnetic resonance imaging contrast agents. Chem Soc Rev 2012; 41:2575–89. https://doi.org/10.1039/C1CS15248C.
[185] Zhu N, Ji H, Yu P, Niu J, Farooq M, Akram M, et al. Surface modification of magnetic iron oxide nanoparticles. Nanomaterials 2018;8:810. https://doi.org/10.3390/nano8100810.
[186] Wu W, Jiang CZ, Roy VAL. Designed synthesis and surface engineering strategies of magnetic iron oxide nanoparticles for biomedical applications. Nanoscale 2016;8:19421–74. https://doi.org/10.1039/C6NR07542H.
[187] Heuer-Jungemann A, Feliu N, Bakaimi I, Hamaly M, Alkilany A, Chakraborty I, et al. The role of ligands in the chemical synthesis and applications of inorganic nanoparticles. Chem Rev 2019;119:4819–80. https://doi.org/10.1021/acs.chemrev.8b00733.
[188] Zhou Z, Wu C, Liu H, Zhu X, Zhao Z, Wang L, et al. Surface and interfacial engineering of iron oxide nanoplates for highly efficient magnetic resonance angiography. ACS Nano 2015;9:3012–22. https://doi.org/10.1021/nn507193f.
[189] Lei M, Fu C, Cheng X, Fu B, Wu N, Zhang Q, et al. Activated surface charge-reversal manganese oxide nanocubes with high surface-to-volume ratio for accurate magnetic resonance tumor imaging. Adv Funct Mater 2017;27:1700978. https://doi.org/10.1002/adfm.201700978.
[190] Davis K, Cole B, Ghelardini M, Powell BA, Mefford OT. Quantitative measurement of ligand exchange with small-molecule ligands on iron oxide nanoparticles via radioanalytical techniques. Langmuir 2016;32:13716–27. https://doi.org/10.1021/acs.langmuir.6b03644.
[191] Hofmann A, Thierbach S, Semisch A, Hartwig A, Taupitz M, Rühl E, et al. Highly monodisperse water-dispersable iron oxide nanoparticles for biomedical applications. J Mater Chem 2010;20:7842. https://doi.org/10.1039/c0jm01169j.
[192] Karouta N, Simos YV, Basina G, Spyrou K, Subrati M, Chatzikonstantinou AV, et al. Highly hydrophilic oleylamine-modified superparamagnetic iron oxide nanoparticles for biomedical applications. ACS Appl Nano Mater 2023;6:2770–83. https://doi.org/10.1021/acsanm.2c04006.
[193] Kim C, Lee SS, Ghosh A, Lee J, Fortner JD. Cetyltrimethylammonium bromide – Oleic acid (CTAB-OA) bilayer coated iron oxide nanocrystals for enhanced chromium (VI) photoreduction via ligand-to-metal charge transfer mechanism. Chem Eng J 2022;431:133938. https://doi.org/10.1016/j.cej.2021.133938.
[194] Zeng J, Jing L, Hou Y, Jiao M, Qiao R, Jia Q, et al. Anchoring group effects of surface ligands on magnetic properties of Fe 3 O 4 nanoparticles: Towards high performance MRI contrast agents. Adv Mater 2014;26:2694–8. https://doi.org/10.1002/adma.201304744.
[195] Liu B, Deng X, Xie Z, Cheng Z, Yang P, Lin J. Thiol-ene click reaction as a facile and general approach for surface functionalization of colloidal nanocrystals. Adv Mater 2017;29:1604878. https://doi.org/10.1002/adma.201604878.
[196] Kim J, Kim HS, Lee N, Kim T, Kim H, Yu T, et al. Multifunctional uniform nanoparticles composed of a magnetite nanocrystal core and a mesoporous silica shell for magnetic resonance and fluorescence imaging and for drug delivery. Angew Chemie Int Ed 2008;47:8438–41. https://doi.org/10.1002/anie.200802469.
[197] Prakash A, Zhu H, Jones CJ, Benoit DN, Ellsworth AZ, Bryant EL, et al. Bilayers as phase transfer agents for nanocrystals prepared in nonpolar solvents. ACS Nano 2009;3:2139–46. https://doi.org/10.1021/nn900373b.
[198] Choi Y-W, Lee H, Song Y, Sohn D. Colloidal stability of iron oxide nanoparticles with multivalent polymer surfactants. J Colloid Interface Sci 2015;443:8–12. https://doi.org/10.1016/j.jcis.2014.11.068.
[199] Soares PIP, Laia CAT, Carvalho A, Pereira LCJ, Coutinho JT, Ferreira IMM, et al. Iron oxide nanoparticles stabilized with a bilayer of oleic acid for magnetic hyperthermia and MRI applications. Appl Surf Sci 2016;383:240–7. https://doi.org/10.1016/j.apsusc.2016.04.181.
[200] Li W, Hinton CH, Lee SS, Wu J, Fortner JD. Surface engineering superparamagnetic nanoparticles for aqueous applications: design and characterization of tailored organic bilayers. Environ Sci Nano 2016;3:85–93. https://doi.org/10.1039/C5EN00089K.
[201] Mylkie K, Nowak P, Rybczynski P, Ziegler-Borowska M. Polymer-coated magnetite nanoparticles for protein immobilization. Materials (Basel) 2021;14:248. https://doi.org/10.3390/ma14020248.
[202] Tang Z, He C, Tian H, Ding J, Hsiao BS, Chu B, et al. Polymeric nanostructured materials for biomedical applications. Prog Polym Sci 2016;60:86–128. https://doi.org/10.1016/j.progpolymsci.2016.05.005.
[203] Soares PIP, Romão J, Matos R, Silva JC, Borges JP. Design and engineering of magneto-responsive devices for cancer theranostics: Nano to macro perspective. Prog Mater Sci 2021;116:100742. https://doi.org/10.1016/j.pmatsci.2020.100742.

[204] Liu R, Guo Y, Odusote G, Qu F, Priestley RD. Core-shell Fe3O4 polydopamine nanoparticles serve multipurpose as drug carrier, catalyst support and carbon adsorbent. ACS Appl Mater Interfaces 2013;5:9167–71. https://doi.org/10.1021/am402585y.
[205] Zhang Z, Smith L, Li W, Jiang L, Zhou F, Davies G-L, et al. Polydopamine-coated nanocomposite theranostic implants for localized chemotherapy and MRI imaging. Int J Pharm 2022;615:121493. https://doi.org/10.1016/j.ijpharm.2022.121493.
[206] Barclay TG, Hegab HM, Clarke SR, Ginic-Markovic M. Versatile surface modification using polydopamine and related polycatecholamines: Chemistry, structure, and applications. Adv Mater Interfaces 2017;4:1601192. https://doi.org/10.1002/admi.201601192.
[207] Yu S, Li G, Liu R, Ma D, Xue W. Dendritic Fe3O4 @Poly(dopamine)@PAMAM nanocomposite as controllable NO-releasing material: A synergistic photothermal and NO antibacterial study. Adv Funct Mater 2018;28:1707440. https://doi.org/10.1002/adfm.201707440.
[208] Lin L-S, Cong Z-X, Cao J-B, Ke K-M, Peng Q-L, Gao J, et al. Multifunctional Fe 3 O 4 @polydopamine core-shell nanocomposites for intracellular mRNA detection and imaging-guided photothermal therapy. ACS Nano 2014;8:3876–83. https://doi.org/10.1021/nn500722y.
[209] He J, Liu X, Niu D, Chen J, Qin X, Li Y. Supramolecular-based PEGylated magnetic hybrid vesicles with ultra-high transverse relaxivity. Appl Mater Today 2018;11:238–45. https://doi.org/10.1016/j.apmt.2018.02.009.
[210] Soetaert F, Korangath P, Serantes D, Fiering S, Ivkov R. Cancer therapy with iron oxide nanoparticles: Agents of thermal and immune therapies. Adv Drug Deliv Rev 2020;163–164:65–83. https://doi.org/10.1016/j.addr.2020.06.025.
[211] Shen S, Huang D, Cao J, Chen Y, Zhang X, Guo S, et al. Magnetic liposomes for light-sensitive drug delivery and combined photothermal–chemotherapy of tumors. J Mater Chem B 2019;7:1096–106. https://doi.org/10.1039/C8TB02684J.
[212] Fang RH, Jiang Y, Fang JC, Zhang L. Cell membrane-derived nanomaterials for biomedical applications. Biomaterials 2017;128:69–83. https://doi.org/10.1016/j.biomaterials.2017.02.041.
[213] Wang S, Yin Y, Song W, Zhang Q, Yang Z, Dong Z, et al. Red-blood-cell-membrane-enveloped magnetic nanoclusters as a biomimetic theranostic nanoplatform for bimodal imaging-guided cancer photothermal therapy. J Mater Chem B 2020;8:803–12. https://doi.org/10.1039/C9TB01829H.
[214] Meng Q-F, Rao L, Zan M, Chen M, Yu G-T, Wei X, et al. Macrophage membrane-coated iron oxide nanoparticles for enhanced photothermal tumor therapy. Nanotechnology 2018;29:134004. https://doi.org/10.1088/1361-6528/aaa7c7.
[215] Yu G-T, Rao L, Wu H, Yang L-L, Bu L-L, Deng W-W, et al. Myeloid-derived suppressor cell membrane-coated magnetic nanoparticles for cancer theranostics by inducing macrophage polarization and synergizing immunogenic cell death. Adv Funct Mater 2018;28:1801389. https://doi.org/10.1002/adfm.201801389.
[216] Rao L, Cai B, Bu L-L, Liao Q-Q, Guo S-S, Zhao X-Z, et al. Microfluidic electroporation-facilitated synthesis of erythrocyte membrane-coated magnetic nanoparticles for enhanced imaging-guided cancer therapy. ACS Nano 2017;11:3496–505. https://doi.org/10.1021/acsnano.7b00133.
[217] Fan R, Cheng Y, Wang R, Zhang T, Zhang H, Li J, et al. Thermosensitive hydrogels and advances in their application in disease therapy. Polymers (Basel) 2022;14:2379. https://doi.org/10.3390/polym14122379.
[218] Dreiss CA. Hydrogel design strategies for drug delivery. Curr Opin Colloid Interface Sci 2020;48:1–17. https://doi.org/10.1016/j.cocis.2020.02.001.
[219] Zhang Z-Q, Song S-C. Thermosensitive/superparamagnetic iron oxide nanoparticle-loaded nanocapsule hydrogels for multiple cancer hyperthermia. Biomaterials 2016;106:13–23. https://doi.org/10.1016/j.biomaterials.2016.08.015.
[220] Ribeiro M, Boudoukhani M, Belmonte-Reche E, Genicio N, Sillankorva S, Gallo J, et al. Xanthan-Fe 3 O 4 nanoparticle composite hydrogels for non-invasive magnetic resonance imaging and magnetically assisted drug delivery. ACS Appl Nano Mater 2021;4:7712–29. https://doi.org/10.1021/acsanm.1c00932.
[221] Xiang Z, Qi Y, Lu Y, Hu Z, Wang X, Jia W, et al. MOF-derived novel porous Fe 3 O 4 @C nanocomposites as smart nanomedical platforms for combined cancer therapy: magnetic-triggered synergistic hyperthermia and chemotherapy. J Mater Chem B 2020;8:8671–83. https://doi.org/10.1039/D0TB01021A.
[222] Asif M, Liu H, Aziz A, Wang H, Wang Z, Ajmal M, et al. Core-shell iron oxide-layered double hydroxide: High electrochemical sensing performance of H2O2 biomarker in live cancer cells with plasma therapeutics. Biosens Bioelectron 2017;97:352–9. https://doi.org/10.1016/j.bios.2017.05.057.
[223] Sabale S, Kandesar P, Jadhav V, Komorek R, Motkuri RK, Yu X-Y. Recent developments in the synthesis, properties, and biomedical applications of core/shell superparamagnetic iron oxide nanoparticles with gold. Biomater Sci 2017;5:2212–25. https://doi.org/10.1039/C7BM00723J.
[224] Croissant JG, Fatieiev Y, Almalik A, Khashab NM. Mesoporous silica and organosilica nanoparticles: Physical chemistry, biosafety, delivery strategies, and biomedical applications. Adv Healthc Mater 2018;7:1700831. https://doi.org/10.1002/adhm.201700831.
[225] Chen W-H, Luo G-F, Lei Q, Cao F-Y, Fan J-X, Qiu W-X, et al. Rational design of multifunctional magnetic mesoporous silica nanoparticle for tumor-targeted magnetic resonance imaging and precise therapy. Biomaterials 2016;76:87–101. https://doi.org/10.1016/j.biomaterials.2015.10.053.
[226] Li W-P, Liao P-Y, Su C-H, Yeh C-S. Formation of oligonucleotide-gated silica shell-coated Fe 3 O 4 -Au core-shell nanotrisoctahedra for magnetically targeted and near-infrared light-responsive theranostic platform. J Am Chem Soc 2014;136:10062–75. https://doi.org/10.1021/ja504118q.
[227] Lin L-S, Yang X, Zhou Z, Yang Z, Jacobson O, Liu Y, et al. Yolk-shell nanostructure: An ideal architecture to achieve harmonious integration of magnetic-plasmonic hybrid theranostic platform. Adv Mater 2017;29:1606681. https://doi.org/10.1002/adma.201606681.
[228] Bin Na H, Song IC, Hyeon T. Inorganic nanoparticles for MRI contrast agents. Adv Mater 2009;21:2133–48. https://doi.org/10.1002/adma.200802366.
[229] Cheon J, Lee J-H. Synergistically integrated nanoparticles as multimodal probes for nanobiotechnology. Acc Chem Res 2008;41:1630–40. https://doi.org/10.1021/ar800045c.
[230] Antwi-Baah R, Wang Y, Chen X, Yu K. Metal-based nanoparticle magnetic resonance imaging contrast agents: classifications, issues, and countermeasures toward their clinical translation. Adv Mater Interfaces 2022;9:2101710. https://doi.org/10.1002/admi.202101710.
[231] Xie W, Guo Z, Gao F, Gao Q, Wang D, Liaw B, et al. Shape-, size- and structure-controlled synthesis and biocompatibility of iron oxide nanoparticles for magnetic theranostics. Theranostics 2018;8:3284–307. https://doi.org/10.7150/thno.25220.
[232] Vuong QL, Berret J-F, Fresnais J, Gossuin Y, Sandre O. A universal scaling law to predict the efficiency of magnetic nanoparticles as MRI T2-contrast agents. Adv Healthc Mater 2012;1:502–12. https://doi.org/10.1002/adhm.201200078.
[233] Hwang L, Freed JH. Dynamic effects of pair correlation functions on spin relaxation by translational diffusion in liquids. J Chem Phys 1975;63:4017–25.
[234] Zhou Z, Tian R, Wang Z, Yang Z, Liu Y, Liu G, et al. Artificial local magnetic field inhomogeneity enhances T2 relaxivity. Nat Commun 2017;8:15468. https://doi.org/10.1038/ncomms15468.
[235] Zhou Z, Yang L, Gao J, Chen X. Structure-relaxivity relationships of magnetic nanoparticles for magnetic resonance imaging. Adv Mater 2019;31:1804567. https://doi.org/10.1002/adma.201804567.
[236] Zhao Z, Chi X, Yang L, Yang R, Ren BW, Zhu X, et al. Cation exchange of anisotropic-shaped magnetite nanoparticles generates high-relaxivity contrast agents for liver tumor imaging. Chem Mater 2016;28:3497–506. https://doi.org/10.1021/acs.chemmater.6b01256.
[237] Zhou Z, Zhu X, Wu D, Chen Q, Huang D, Sun C, et al. Anisotropic shaped iron oxide nanostructures: Controlled synthesis and proton relaxation shortening effects. Chem Mater 2015;27:3505–15. https://doi.org/10.1021/acs.chemmater.5b00944.
[238] Yang L, Wang Z, Ma L, Li A, Xin J, Wei R, et al. The roles of morphology on the relaxation rates of magnetic nanoparticles. ACS Nano 2018;12:4605–14. https://doi.org/10.1021/acsnano.8b01048.
[239] Zhou Z, Zhao Z, Zhang H, Wang Z, Chen X, Wang R, et al. Interplay between longitudinal and transverse contrasts in Fe3O4. ACS Nano 2014:7976–85.
[240] Freed JH. Dynamic effects of pair correlation functions on spin relaxation by translational diffusion in liquids. II. Finite jumps and independent T 1 processes. J Chem Phys 1978;68:4034–7. https://doi.org/10.1063/1.436302.
[241] Linderoth S, Hendriksen PV, Bo F, Dker S, Wells S, Davies K, Charles SW, Mo/rup S. On spin-canting in maghemite particles. J Appl Phys 1994;75:6583–5. https://doi.org/10.1063/1.356902.
[242] Jaganathan H, Hugar DL, Ivanisevic A. Examining MRI contrast in three-dimensional cell culture phantoms with DNA-templated nanoparticle chains. ACS Appl Mater Interfaces 2011;3:1282–8. https://doi.org/10.1021/am200086r.
[243] Wang H, Mararenko A, Cao G, Gai Z, Hong K, Banerjee P, et al. Multifunctional 1D magnetic and fluorescent nanoparticle chains for enhanced MRI, fluorescent cell imaging, and combined photothermal/chemotherapy. ACS Appl Mater Interfaces 2014;6:15309–17. https://doi.org/10.1021/am503777k.
[244] Solomon I. Relaxation processes in a system of two spins. Phys Rev 1955;99:559.
[245] Bloembergen N, Morgan LO. Proton relaxation times in paramagnetic solutions. Effects of electron spin relaxation. J Chem Phys 1961;34:842–50.

[246] Bleuzen A, Foglia F, Furet E, Helm L, Merbach AE, Weber J. Second coordination shell water exchange rate and mechanism: experiments and modeling on hexaaquachromium (III). J Am Chem Soc 1996;118:12777–87.
[247] Werner EJ, Datta A, Jocher CJ, Raymond KN. High-relaxivity MRI contrast agents: Where coordination chemistry meets medical imaging. Angew Chemie Int Ed 2008;47:8568–80. https://doi.org/10.1002/anie.200800212.
[248] Caravan P, Ellison JJ, McMurry TJ, Lauffer RB. Gadolinium(III) chelates as MRI contrast agents: Structure, dynamics, and applications. Chem Rev 1999;99:2293–352. https://doi.org/10.1021/cr980440x.
[249] Neuwelt EA, Hamilton BE, Varallyay CG, Rooney WR, Edelman RD, Jacobs PM, et al. Ultrasmall superparamagnetic iron oxides (USPIOs): a future alternative magnetic resonance (MR) contrast agent for patients at risk for nephrogenic systemic fibrosis (NSF)? Kidney Int 2009;75:465–74. https://doi.org/10.1038/ki.2008.496.
[250] Tromsdorf UI, Bruns OT, Salmen SC, Beisiegel U, Weller H. A highly effective, nontoxic T 1 MR contrast agent based on ultrasmall PEGylated iron oxide nanoparticles. Nano Lett 2009;9:4434–40. https://doi.org/10.1021/nl902715v.
[251] Zhou Z, Wang L, Chi X, Bao J, Yang L, Zhao W, et al. Engineered iron-oxide-based nanoparticles as enhanced T 1 contrast agents for efficient tumor imaging. ACS Nano 2013;7:3287–96. https://doi.org/10.1021/nn305991e.
[252] Zhao Z, Bao J, Fu C, Lei M, Cheng J. Controllable synthesis of manganese oxide nanostructures from 0-D to 3-D and mechanistic investigation of internal relation between structure and T 1 relaxivity. Chem Mater 2017;29:10455–68. https://doi.org/10.1021/acs.chemmater.7b04100.
[253] Huang C-C, Khu N-H, Yeh C-S. The characteristics of sub 10 nm manganese oxide T1 contrast agents of different nanostructured morphologies. Biomaterials 2010;31:4073–8. https://doi.org/10.1016/j.biomaterials.2010.01.087.
[254] Stinnett G, Taheri N, Villanova J, Bohloul A, Guo X, Esposito EP, et al. 2D gadolinium oxide nanoplates as T 1 magnetic resonance imaging contrast agents. Adv Healthc Mater 2021;10:2001780. https://doi.org/10.1002/adhm.202001780.
[255] Davies G-L, Kramberger I, Davis JJ. Environmentally responsive MRI contrast agents. Chem Commun 2013;49:9704. https://doi.org/10.1039/c3cc44268c.
[256] Chen R, Ling D, Zhao L, Wang S, Liu Y, Bai R, et al. Parallel comparative studies on mouse toxicity of oxide nanoparticle- and gadolinium-based T1 MRI contrast agents. ACS Nano 2015;9:12425–35. https://doi.org/10.1021/acsnano.5b05783.
[257] Gleich B, Weizenecker J. Tomographic imaging using the nonlinear response of magnetic particles. Nature 2005;435:1214–7. https://doi.org/10.1038/nature03808.
[258] Pablico-Lansigan MH, Situ SF, Samia ACS. Magnetic particle imaging: Advancements and perspectives for real-time in vivo monitoring and image-guided therapy. Nanoscale 2013;5:4040–55. https://doi.org/10.1039/c3nr00544e.
[259] Goodwill PW, Saritas EU, Croft LR, Kim TN, Krishnan KM, Schaffer DV, et al. X-Space MPI: Magnetic nanoparticles for safe medical imaging. Adv Mater 2012;24:3870–7. https://doi.org/10.1002/adma.201200221.
[260] Weizenecker J, Gleich B, Rahmer J, Dahnke H, Borgert J. Three-dimensional real-time in vivo magnetic particle imaging. Phys Med Biol 2009;54:L1.
[261] Rahmer J, Weizenecker J, Gleich B, Borgert J. Signal encoding in magnetic particle imaging: properties of the system function. BMC Med Imaging 2009;9:4. https://doi.org/10.1186/1471-2342-9-4.
[262] Panagiotopoulos N, Duschka RL, Ahlborg M, Bringout G, Debbeler C, Graeser M, et al. Magnetic particle imaging: current developments and future directions. Int J Nanomedicine 2015;10:3097.
[263] Tay ZW, Savliwala S, Hensley DW, Fung KLB, Colson C, Fellows BD, et al. Superferromagnetic nanoparticles enable order-of-magnitude resolution & sensitivity gain in magnetic particle imaging. Small Methods 2021;5:2100796.
[264] Ferguson RM, Minard KR, Krishnan KM. Optimization of nanoparticle core size for magnetic particle imaging. J Magn Magn Mater 2009;321:1548–51.
[265] Bauer LM, Situ SF, Griswold MA, Samia ACS. Magnetic particle imaging tracers: State-of-the-art and future directions. J Phys Chem Lett 2015;6:2509–17. https://doi.org/10.1021/acs.jpclett.5b00610.
[266] Wang Q, Ma X, Liao H, Liang Z, Li F, Tian J, et al. Artificially engineered cubic iron oxide nanoparticle as a high-performance magnetic particle imaging tracer for stem cell tracking. ACS Nano 2020;14:2053–62. https://doi.org/10.1021/acsnano.9b08660.
[267] Lee N, Choi Y, Lee Y, Park M, Moon WK, Choi SH, et al. Water-dispersible ferrimagnetic iron oxide nanocubes with extremely high r 2 relaxivity for highly sensitive in Vivo MRI of tumors. Nano Lett 2012;12:3127–31. https://doi.org/10.1021/nl3010308.
[268] Bauer LM, Situ SF, Griswold MA, Samia ACS. High-performance iron oxide nanoparticles for magnetic particle imaging – guided hyperthermia (hMPI). Nanoscale 2016;8:12162–9. https://doi.org/10.1039/C6NR01877G.
[269] Zhu S, Xu X, Rong R, Li B, Wang X. Evaluation of zinc-doped magnetite nanoparticle toxicity in the liver and kidney of mice after sub-chronic intragastric administration. Toxicol Res (Camb) 2016;5:97–106.
[270] Yang M, Ho C, Ruta S, Chantrell R, Krycka K, Hovorka O, et al. Magnetic interaction of multifunctional core-shell nanoparticles for highly effective theranostics. Adv Mater 2018;30:1802444. https://doi.org/10.1002/adma.201802444.
[271] Avugadda SK, Wickramasinghe S, Niculaes D, Ju M, Lak A, Silvestri N, et al. Uncovering the magnetic particle imaging and magnetic resonance imaging features of iron oxide nanocube clusters. Nanomaterials 2020;11:62.
[272] Espinosa A, Di Corato R, Kolosnjaj-Tabi J, Flaud P, Pellegrino T, Wilhelm C. Duality of iron oxide nanoparticles in cancer therapy: amplification of heating efficiency by magnetic hyperthermia and photothermal bimodal treatment. ACS Nano 2016;10:2436–46.
[273] Guo X, Li W, Luo L, Wang Z, Li Q, Kong F, et al. External magnetic field-enhanced chemo-photothermal combination tumor therapy via iron oxide nanoparticles. ACS Appl Mater Interfaces 2017;9:16581–93.
[274] Guo X, Wu Z, Li W, Wang Z, Li Q, Kong F, et al. Appropriate size of magnetic nanoparticles for various bioapplications in cancer diagnostics and therapy. ACS Appl Mater Interfaces 2016;8:3092–106.
[275] Chen H, Burnett J, Zhang F, Zhang J, Paholak H, Sun D. Highly crystallized iron oxide nanoparticles as effective and biodegradable mediators for photothermal cancer therapy. J Mater Chem B 2014;2:757–65. https://doi.org/10.1039/C3TB21338B.
[276] Liu Y, Ai K, Liu J, Deng M, He Y, Lu L. Dopamine-melanin colloidal nanospheres: An efficient near-infrared photothermal therapeutic agent for in vivo cancer therapy. Adv Mater 2013;25:1353–9. https://doi.org/10.1002/adma.201204683.
[277] Nehl CL, Hafner JH. Shape-dependent plasmon resonances of gold nanoparticles. J Mater Chem 2008;18:2415–9.
[278] Guo L, Jackman JA, Yang H-H, Chen P, Cho N-J, Kim D-H. Strategies for enhancing the sensitivity of plasmonic nanosensors. Nano Today 2015;10:213–39.
[279] Chu M, Shao Y, Peng J, Dai X, Li H, Wu Q, et al. Near-infrared laser light mediated cancer therapy by photothermal effect of Fe3O4 magnetic nanoparticles. Biomaterials 2013;34:4078–88. https://doi.org/10.1016/j.biomaterials.2013.01.086.
[280] Lozano-Pedraza C, Plaza-Mayoral E, Espinosa A, Sot B, Serrano A, Salas G, et al. Assessing the parameters modulating optical losses of iron oxide nanoparticles under near infrared irradiation. Nanoscale Adv 2021;3:6490–502. https://doi.org/10.1039/D1NA00601K.
[281] Espinosa A, Kolosnjaj-Tabi J, Abou-Hassan A, Plan Sangnier A, Curcio A, Silva AKA, et al. Magnetic (Hyper)thermia or photothermia? progressive comparison of iron oxide and gold nanoparticles heating in water, in cells, and in vivo. Adv Funct Mater 2018;28:1803660. https://doi.org/10.1002/adfm.201803660.
[282] Suto M, Hirota Y, Mamiya H, Fujita A, Kasuya R, Tohji K, et al. Heat dissipation mechanism of magnetite nanoparticles in magnetic fluid hyperthermia. J Magn Magn Mater 2009;321:1493–6. https://doi.org/10.1016/j.jmmm.2009.02.070.
[283] Rosensweig RE. Heating magnetic fluid with alternating magnetic field. J Magn Magn Mater 2002;252:370–4. https://doi.org/10.1016/S0304-8853(02)00706-0.
[284] Mohapatra J, Xing M, Liu JP. Inductive thermal effect of ferrite magnetic nanoparticles. Materials (Basel) 2019;12:3208. https://doi.org/10.3390/ma12193208.
[285] Gavilán H, Avugadda SK, Fernández-Cabada T, Soni N, Cassani M, Mai BT, et al. Magnetic nanoparticles and clusters for magnetic hyperthermia: optimizing their heat performance and developing combinatorial therapies to tackle cancer. Chem Soc Rev 2021. https://doi.org/10.1039/D1CS00427A.
[286] Barick KC, Aslam M, Lin Y-P, Bahadur D, Prasad PV, Dravid VP. Novel and efficient MR active aqueous colloidal Fe3O4 nanoassemblies. J Mater Chem 2009;19:7023. https://doi.org/10.1039/b911626e.

[287] Nemati Z, Salili SM, Alonso J, Ataie A, Das R, Phan MH, et al. Superparamagnetic iron oxide nanodiscs for hyperthermia therapy: Does size matter? J Alloys Compd 2017;714:709–14. https://doi.org/10.1016/j.jallcom.2017.04.211.
[288] Khurshid H, Alonso J, Nemati Z, Phan MH, Mukherjee P, Fdez-Gubieda ML, et al. Anisotropy effects in magnetic hyperthermia: A comparison between spherical and cubic exchange-coupled FeO/Fe 3 O 4 nanoparticles. J Appl Phys 2015;117:17A337. https://doi.org/10.1063/1.4919250.
[289] Nemati Z, Alonso J, Martinez LM, Khurshid H, Garaio E, Garcia JA, et al. Enhanced magnetic hyperthermia in iron oxide nano-octopods: Size and anisotropy effects. J Phys Chem C 2016;120:8370–9. https://doi.org/10.1021/acs.jpcc.6b01426.
[290] Mitra A, Mohapatra J, Meena SS, Tomy CV, Aslam M. Verwey transition in ultrasmall-sized octahedral Fe3O4 nanoparticles. J Phys Chem C 2014;118:19356–62. https://doi.org/10.1021/jp501652e.
[291] Yang Y, Liu X, Lv Y, Herng TS, Xu X, Xia W, et al. Orientation mediated enhancement on magnetic hyperthermia of Fe3O4 nanodisc. Adv Funct Mater 2015;25:812–20. https://doi.org/10.1002/adfm.201402764.
[292] Tong S, Quinto CA, Zhang L, Mohindra P, Bao G. Size-dependent heating of magnetic iron oxide nanoparticles. ACS Nano 2017;11:6808–16. https://doi.org/10.1021/acsnano.7b01762.
[293] Guardia P, Labarta A, Batlle X. Tuning the size, the shape, and the magnetic properties of iron oxide nanoparticles. J Phys Chem C 2011;115:390–6.
[294] Mohapatra J, Mitra A, Aslam M, Bahadur D. Octahedral-shaped Fe3O4 nanoparticles with enhanced specific absorption rate and ${R}_{2}$ Relaxivity. IEEE Trans Magn 2015;51:1–3. https://doi.org/10.1109/TMAG.2015.2439213.
[295] Gavilán H, Simeonidis K, Myrovali E, Mazarío E, Chubykalo-Fesenko O, Chantrell R, et al. How size, shape and assembly of magnetic nanoparticles give rise to different hyperthermia scenarios. Nanoscale 2021. https://doi.org/10.1039/d1nr03484g.
[296] Shi G, Takeda R, Trisnanto SB, Yamada T, Ota S, Takemura Y. Enhanced specific loss power from Resovist® achieved by aligning magnetic easy axes of nanoparticles for hyperthermia. J Magn Magn Mater 2019;473:148–54.
[297] Shah SA, Reeves DB, Ferguson RM, Weaver JB, Krishnan KM. Mixed Brownian alignment and Néel rotations in superparamagnetic iron oxide nanoparticle suspensions driven by an ac field. Phys Rev B 2015;92:94438.
[298] Geng S, Yang H, Ren X, Liu Y, He S, Zhou J, et al. Anisotropic magnetite nanorods for enhanced magnetic hyperthermia. Chem - An Asian J 2016;11:2996–3000. https://doi.org/10.1002/asia.201601042.
[299] Munoz-Menendez C, Conde-Leboran I, Baldomir D, Chubykalo-Fesenko O, Serantes D. The role of size polydispersity in magnetic fluid hyperthermia: average vs. local infra/over-heating effects. Phys Chem Chem Phys 2015;17:27812–20.
[300] Muñoz-Menendez C, Serantes D, Chubykalo-Fesenko O, Ruta S, Hovorka O, Nieves P, et al. Disentangling local heat contributions in interacting magnetic nanoparticles. Phys Rev B 2020;102:214412.
[301] Munoz-Menendez C, Serantes D, Ruso JM, Baldomir D. Towards improved magnetic fluid hyperthermia: major-loops to diminish variations in local heating. Phys Chem Chem Phys 2017;19:14527–32. https://doi.org/10.1039/C7CP01442B.
[302] Luther DC, Huang R, Jeon T, Zhang X, Lee Y-W, Nagaraj H, et al. Delivery of drugs, proteins, and nucleic acids using inorganic nanoparticles. Adv Drug Deliv Rev 2020;156:188–213. https://doi.org/10.1016/j.addr.2020.06.020.
[303] Ulbrich K, Hola K, Subr V, Bakandritsos A, Tucek J, Zboril R. Targeted drug delivery with polymers and magnetic nanoparticles: covalent and noncovalent approaches, release control, and clinical studies. Chem Rev 2016;116:5338–431.
[304] Qiu Y, Tong S, Zhang L, Sakurai Y, Myers DR, Hong L, et al. Magnetic forces enable controlled drug delivery by disrupting endothelial cell-cell junctions. Nat Commun 2017;8:1–10.
[305] Paul W, Sharma CP. Inorganic nanoparticles for targeted drug delivery. Biointegration Med Implant Mater 2020:333–73.
[306] Fuller EG, Scheutz GM, Jimenez A, Lewis P, Savliwala S, Liu S, et al. Theranostic nanocarriers combining high drug loading and magnetic particle imaging. Int J Pharm 2019;572:118796.
[307] Jeon H, Kim J, Lee YM, Kim J, Choi HW, Lee J, et al. Poly-paclitaxel/cyclodextrin-SPION nano-assembly for magnetically guided drug delivery system. J Control Release 2016;231:68–76. https://doi.org/10.1016/j.jconrel.2016.01.006.
[308] Clauson RM, Chen M, Scheetz LM, Berg B, Chertok B. Size-controlled iron oxide nanoplatforms with lipidoid-stabilized shells for efficient magnetic resonance imaging-trackable lymph node targeting and high-capacity biomolecule display. ACS Appl Mater Interfaces 2018;10:20281–95.
[309] Albarqi HA, Wong LH, Schumann C, Sabei FY, Korzun T, Li X, et al. Biocompatible nanoclusters with high heating efficiency for systemically delivered magnetic hyperthermia. ACS Nano 2019;13:6383–95.
[310] Lanier OL, Monsalve AG, McFetridge PS, Dobson J. Magnetically triggered release of biologics. Int Mater Rev 2019;64:63–90.
[311] Moros M, Idiago-López J, Asín L, Moreno-Antolín E, Beola L, Grazú V, et al. Triggering antitumoural drug release and gene expression by magnetic hyperthermia. Adv Drug Deliv Rev 2019;138:326–43.
[312] Carregal-Romero S, Guardia P, Yu X, Hartmann R, Pellegrino T, Parak WJ. Magnetically triggered release of molecular cargo from iron oxide nanoparticle loaded microcapsules. Nanoscale 2015;7:570–6. https://doi.org/10.1039/C4NR04055D.
[313] Martinez-Boubeta C, Simeonidis K, Serantes D, Conde-Leborán I, Kazakis I, Stefanou G, et al. Adjustable hyperthermia response of self-assembled ferromagnetic Fe-MgO core-shell nanoparticles by tuning dipole-dipole interactions. Adv Funct Mater 2012;22:3737–44. https://doi.org/10.1002/adfm.201200307.
[314] Haase C, Nowak U. Role of dipole-dipole interactions for hyperthermia heating of magnetic nanoparticle ensembles. Phys Rev B 2012;85:045435. https://doi.org/10.1103/PhysRevB.85.045435.
[315] Zhu D, Roy S, Liu Z, Weller H, Parak WJ, Feliu N. Remotely controlled opening of delivery vehicles and release of cargo by external triggers. Adv Drug Deliv Rev 2019;138:117–32. https://doi.org/10.1016/j.addr.2018.10.003.
[316] Mertz D, Sandre O, Begin-Colin S. Drug releasing nanoplatforms activated by alternating magnetic fields. Biochim Biophys Acta (BBA)-General Subj 2017;1861:1617–41.
[317] Ding X, Shi X, He X, Yu F, Xue C, Liu M, et al. Sol-gel system functionalized magnetic nanocubes as remote controlled drug carriers for cooperative tumor-targeted therapy. Mater Lett 2016;175:236–40.
[318] Mai BT, Balakrishnan PB, Barthel MJ, Piccardi F, Niculaes D, Marinaro F, et al. Thermoresponsive iron oxide nanocubes for an effective clinical translation of magnetic hyperthermia and heat-mediated chemotherapy. ACS Appl Mater Interfaces 2019;11:5727–39. https://doi.org/10.1021/acsami.8b16226.
[319] Moreno-Mateos MA, Gonzalez-Rico J, Nunez-Sardinha E, Gomez-Cruz C, Lopez-Donaire ML, Lucarini S, et al. Magneto-mechanical system to reproduce and quantify complex strain patterns in biological materials. Appl Mater Today 2022;27:101437. https://doi.org/10.1016/j.apmt.2022.101437.
[320] Tomás AR, Gonçalves AI, Paz E, Freitas P, Domingues RMA, Gomes ME. Magneto-mechanical actuation of magnetic responsive fibrous scaffolds boosts tenogenesis of human adipose stem cells. Nanoscale 2019;11:18255–71. https://doi.org/10.1039/C9NR04355A.
[321] Sun M, Liu Q, Fan X, Wang Y, Chen W, Tian C, et al. Autonomous biohybrid urchin-like microperforator for intracellular payload delivery. Small 2020;16:1–12. https://doi.org/10.1002/smll.201906701.
[322] Vlasova KY, Piroyan A, Le-Deygen IM, Vishwasrao HM, Ramsey JD, Klyachko NL, et al. Magnetic liposome design for drug release systems responsive to super-low frequency alternating current magnetic field (AC MF). J Colloid Interface Sci 2019;552:689–700. https://doi.org/10.1016/j.jcis.2019.05.071.
[323] Gregurec D, Senko AW, Chuvilin A, Reddy PD, Sankararaman A, Rosenfeld D, et al. Magnetic vortex nanodiscs enable remote magnetomechanical neural stimulation. ACS Nano 2020;14:8036–45. https://doi.org/10.1021/acsnano.0c00562.
[324] Xue L, Ye Q, Wu L, Li D, Bao S, Lu Q, et al. Magneto-mechanical effect of magnetic microhydrogel for improvement of magnetic neuro-stimulation. Nano Res 2023;16:7393–404. https://doi.org/10.1007/s12274-023-5464-x.
[325] Adedoyin AA, Ekenseair AK. Biomedical applications of magneto-responsive scaffolds. Nano Res 2018;11:5049–64. https://doi.org/10.1007/s12274-018-2198-2.
[326] He Y, Wang L, Yang K, Wang X, Rong W, Sun L. Cooperative self-assembled magnetic micropaddles at liquid surfaces. ACS Appl Mater Interfaces 2021;13:46180–91. https://doi.org/10.1021/acsami.1c13551.
[327] Wang Z, Fu D, Xie D, Fu S, Wu J, Wang S, et al. Magnetic helical hydrogel motor for directing T cell chemotaxis. Adv Funct Mater 2021;31:1–8. https://doi.org/10.1002/adfm.202101648.

[328] Golovin YI, Golovin DY, Vlasova KY, Veselov MM, Usvaliev AD, Kabanov AV, et al. Non-heating alternating magnetic field nanomechanical stimulation of biomolecule structures via magnetic nanoparticles as the basis for future low-toxic biomedical applications. Nanomaterials 2021;11:2255. https://doi.org/10.3390/nano11092255.
[329] Wang P, Chen C, Wang Q, Chen H, Chen C, Xu J, et al. Tumor inhibition via magneto-mechanical oscillation by magnetotactic bacteria under a swing MF. J Control Release 2022;351:941–53. https://doi.org/10.1016/j.jconrel.2022.09.059.
[330] Nikitin AA, Prishchepa AV, Rytov RA, Chekhonin VP, Abakumov MA. Unveiling the role of the properties of magnetic nanoparticles for highly efficient low-frequency magneto-mechanical actuation of biomolecules. J Phys Chem Lett 2023;14:9112–7. https://doi.org/10.1021/acs.jpclett.3c01944.
[331] Zhang E, Kircher MF, Koch M, Eliasson L, Goldberg SN, Renström E. Dynamic magnetic fields remote-control apoptosis via nanoparticle rotation. ACS Nano 2014;8:3192–201. https://doi.org/10.1021/nn406302j.
[332] Wong DW, Gan WL, Teo YK, Lew WS. Interplay of cell death signaling pathways mediated by alternating magnetic field gradient. Cell Death Discov 2018;4:49. https://doi.org/10.1038/s41420-018-0052-7.
[333] Lopez S, Hallali N, Lalatonne Y, Hillion A, Antunes JC, Serhan N, et al. Magneto-mechanical destruction of cancer-associated fibroblasts using ultra-small iron oxide nanoparticles and low frequency rotating magnetic fields. Nanoscale Adv 2022;4:421–36. https://doi.org/10.1039/D1NA00474C.
[334] Maniotis N, Makridis A, Myrovali E, Theopoulos A, Samaras T, Angelakeris M. Magneto-mechanical action of multimodal field configurations on magnetic nanoparticle environments. J Magn Magn Mater 2019;470:6–11. https://doi.org/10.1016/j.jmmm.2017.12.024.
[335] Zhao P, Han Y, Nguyen H, Corey E, Gao X. Magneto-endosomalytic therapy for cancer. Adv Healthc Mater 2022;11. https://doi.org/10.1002/adhm.202101010.
[336] Golovin YI, Zhigachev AO, Klyachko NL, Golovin DY. Controlled localization of magnetic nanoparticle mechanical activation in suspension exposed to alternating magnetic field using gradient magnetic field. J Nanoparticle Res 2022;24:167. https://doi.org/10.1007/s11051-022-05501-8.
[337] Nabavinia M, Beltran-Huarac J. Recent progress in iron oxide nanoparticles as therapeutic magnetic agents for cancer treatment and tissue engineering. ACS Appl Bio Mater 2020;3:8172–87. https://doi.org/10.1021/acsabm.0c00947.
[338] An J, Hong H, Won M, Rha H, Ding Q, Kang N, et al. Mechanical stimuli-driven cancer therapeutics. Chem Soc Rev 2023;52:30–46. https://doi.org/10.1039/D2CS00546H.
[339] Nikitin AA, Ivanova AV, Semkina AS, Lazareva PA, Abakumov MA. Magneto-mechanical approach in biomedicine: Benefits, challenges, and future perspectives. Int J Mol Sci 2022;23:11134. https://doi.org/10.3390/ijms231911134.
[340] Orel VB, Papazoglou AS, Tsagkaris C, Moysidis DV, Papadakos S, Galkin OY, et al. Nanotherapy based on magneto-mechanochemical modulation of tumor redox state. WIREs Nanomed Nanobiotechnol 2023;15:1–21. https://doi.org/10.1002/wnan.1868.
[341] Beltran-Huarac J, Yamaleyeva DN, Dotti G, Hingtgen S, Sokolsky-Papkov M, Kabanov AV. Magnetic control of protein expression via magneto-mechanical actuation of ND-PEGylated iron oxide nanocubes for cell therapy. ACS Appl Mater Interfaces 2023;15:19877–91. https://doi.org/10.1021/acsami.3c00179.
[342] Martínez-Banderas AI, Aires A, Teran FJ, Perez JE, Cadenas JF, Alsharif N, et al. Functionalized magnetic nanowires for chemical and magneto-mechanical induction of cancer cell death. Sci Rep 2016;6:35786. https://doi.org/10.1038/srep35786.
[343] Serantes D, Chantrell R, Gavilán H, Morales MDP, Chubykalo-Fesenko O, Baldomir D, et al. Anisotropic magnetic nanoparticles for biomedicine: bridging frequency separated AC-field controlled domains of actuation. Phys Chem Chem Phys 2018;20:30445–54. https://doi.org/10.1039/C8CP02768D.
[344] Cheng Y, Muroski ME, Petit DCMC, Mansell R, Vemulkar T, Morshed RA, et al. Rotating magnetic field induced oscillation of magnetic particles for in vivo mechanical destruction of malignant glioma. J Control Release 2016;223:75–84. https://doi.org/10.1016/j.jconrel.2015.12.028.
[345] Zhao Z, Ukidve A, Krishnan V, Mitragotri S. Effect of physicochemical and surface properties on in vivo fate of drug nanocarriers. Adv Drug Deliv Rev 2019;143:3–21. https://doi.org/10.1016/j.addr.2019.01.002.
[346] Kinnear C, Moore TL, Rodriguez-Lorenzo L, Rothen-Rutishauser B, Petri-Fink A. Form follows function: Nanoparticle shape and its implications for nanomedicine. Chem Rev 2017;117:11476–521. https://doi.org/10.1021/acs.chemrev.7b00194.
[347] Sousa De Almeida M, Susnik E, Drasler B, Taladriz-Blanco P, Petri-Fink A, Rothen-Rutishauser B. Understanding nanoparticle endocytosis to improve targeting strategies in nanomedicine. Chem Soc Rev 2021;50:5397–434. https://doi.org/10.1039/d0cs01127d.
[348] Xie X, Liao J, Shao X, Li Q, Lin Y. The effect of shape on cellular uptake of gold nanoparticles in the forms of stars, rods, and triangles. Sci Rep 2017;7:3827. https://doi.org/10.1038/s41598-017-04229-z.
[349] Qiu L, Chen T, Öçsoy I, Yasun E, Wu C, Zhu G, et al. A cell-targeted, size-photocontrollable, nuclear-uptake nanodrug delivery system for drug-resistant cancer therapy. Nano Lett 2015;15:457–63.
[350] Yang Y, Nie D, Liu Y, Yu M, Gan Y. Advances in particle shape engineering for improved drug delivery. Drug Discov Today 2019;24:575–83. https://doi.org/10.1016/j.drudis.2018.10.006.
[351] Shen Z, Ye H, Yi X, Li Y. Membrane wrapping efficiency of elastic nanoparticles during endocytosis: Size and shape matter. ACS Nano 2019;13:215–28. https://doi.org/10.1021/acsnano.8b05340.
[352] Meng H, Yang S, Li Z, Xia T, Chen J, Ji Z, et al. Aspect ratio determines the quantity of mesoporous silica nanoparticle uptake by a small gtpase-dependent macropinocytosis mechanism. ACS Nano 2011;5:4434–47. https://doi.org/10.1021/nn103344k.
[353] Gratton SEA, Ropp PA, Pohlhaus PD, Luft JC, Madden VJ, Napier ME, et al. The effect of particle design on cellular internalization pathways. Proc Natl Acad Sci 2008;105:11613–8. https://doi.org/10.1073/pnas.0801763105.
[354] Tan J, Shah S, Thomas A, Ou-Yang HD, Liu Y. The influence of size, shape and vessel geometry on nanoparticle distribution. Microfluid Nanofluidics 2013;14:77–87. https://doi.org/10.1007/s10404-012-1024-5.
[355] Potrč T, Kralj S, Nemec S, Kocbek P, Erdani Kreft M. The shape anisotropy of magnetic nanoparticles: an approach to cell-type selective and enhanced internalization. Nanoscale 2023;15:8611–8. https://doi.org/10.1039/D2NR06965B.
[356] Van de Walle A, Kolosnjaj-Tabi J, Lalatonne Y, Wilhelm C. Ever-evolving identity of magnetic nanoparticles within human cells: The interplay of endosomal confinement, degradation, storage, and neocrystallization. Acc Chem Res 2020;53:2212–24. https://doi.org/10.1021/acs.accounts.0c00355.
[357] Agarwal R, Singh V, Jurney P, Shi L, Sreenivasan SV, Roy K. Mammalian cells preferentially internalize hydrogel nanodiscs over nanorods and use shape-specific uptake mechanisms. Proc Natl Acad Sci 2013;110:17247–52. https://doi.org/10.1073/pnas.1305000110.
[358] Champion JA, Mitragotri S. Role of target geometry in phagocytosis. Proc Natl Acad Sci 2006;103:4930–4. https://doi.org/10.1073/pnas.0600997103.
[359] Sharma G, Valenta DT, Altman Y, Harvey S, Xie H, Mitragotri S, et al. Polymer particle shape independently influences binding and internalization by macrophages. J Control Release 2010;147:408–12. https://doi.org/10.1016/j.jconrel.2010.07.116.
[360] Cotin G, Blanco-Andujar C, Nguyen D-V, Affolter C, Boutry S, Boos A, et al. Dendron based antifouling, MRI and magnetic hyperthermia properties of different shaped iron oxide nanoparticles. Nanotechnology 2019;30:374002. https://doi.org/10.1088/1361-6528/ab2998.
[361] Cai X, Dong J, Liu J, Zheng H, Kaweeteerawat C, Wang F, et al. Multi-hierarchical profiling the structure-activity relationships of engineered nanomaterials at nano-bio interfaces. Nat Commun 2018;9:4416. https://doi.org/10.1038/s41467-018-06869-9.
[362] Liu Y, Balachandran YL, Li D, Shao Y, Jiang X. Polyvinylpyrrolidone–poly (ethylene glycol) modified silver nanorods can be a safe, noncarrier adjuvant for HIV vaccine. ACS Nano 2016;10:3589–96.
[363] Alkilany AM, Nagaria PK, Hexel CR, Shaw TJ, Murphy CJ, Wyatt MD. Cellular uptake and cytotoxicity of gold nanorods: molecular origin of cytotoxicity and surface effects. Small 2009;5:701–8.
[364] Zhang T, Xu Q, Huang T, Ling D, Gao J. New insights into biocompatible iron oxide nanoparticles: A potential booster of gene delivery to stem cells. Small 2020;16:2001588. https://doi.org/10.1002/smll.202001588.
[365] Patil RM, Thorat ND, Shete PB, Bedge PA, Gavde S, Joshi MG, et al. Comprehensive cytotoxicity studies of superparamagnetic iron oxide nanoparticles. Biochem Biophys Reports 2018;13:63–72.
[366] Samrot AV, Sahithya CS, Selvarani J, Purayil SK, Ponnaiah P. A review on synthesis, characterization and potential biological applications of superparamagnetic iron oxide nanoparticles. Curr Res Green Sustain Chem 2021;4:100042.

[367] Mahmoudi M, Hofmann H, Rothen-Rutishauser B, Petri-Fink A. Assessing the in vitro and in vivo toxicity of superparamagnetic iron oxide nanoparticles. Chem Rev 2012;112:2323–38.
[368] Schwenk MH. Ferumoxytol: A new intravenous iron preparation for the treatment of iron deficiency anemia in patients with chronic kidney disease. Pharmacotherapy 2010;30:70–9. https://doi.org/10.1592/phco.30.1.70.
[369] Hetzel D, Strauss W, Bernard K, Li Z, Urboniene A, Allen LF, et al. randomized, open-label trial of ferumoxytol compared with iron sucrose for the treatment of iron deficiency anemia in patients with a history of unsatisfactory oral iron therapy. Am J Hematol 2014;89:646–50. https://doi.org/10.1002/ajh.23712.
[370] Zhu L, Zhou Z, Mao H, Yang L. Magnetic nanoparticles for precision oncology: theranostic magnetic iron oxide nanoparticles for image-guided and targeted cancer therapy. Nanomedicine 2017;12:73–87. https://doi.org/10.2217/nnm-2016-0316.
[371] Xu Y, Wu H, Xiong Q, Ji B, Yi H, Duan H, et al. Size-controllable magnetic iron oxide nanorods for biomarker targeting and improving microfluidic mixing. ACS Appl Bio Mater 2019;2:3362–71. https://doi.org/10.1021/acsabm.9b00359.
[372] Li X, Bao M, Weng Y, Yang K, Zhang W, Chen G. Glycopolymer-coated iron oxide nanoparticles: shape-controlled synthesis and cellular uptake. J Mater Chem B 2014;2:5569–75. https://doi.org/10.1039/C4TB00852A.
[373] Yao X, Sabyrov K, Klein T, Penn RL, Wiedmann TS. Evaluation of magnetic heating of asymmetric magnetite particles. J Magn Magn Mater 2015;381:21–7.
[374] Cheng D, Li X, Zhang G, Shi H. Morphological effect of oscillating magnetic nanoparticles in killing tumor cells. Nanoscale Res Lett 2014;9:195. https://doi.org/10.1186/1556-276X-9-195.
[375] Kim D-H, Rozhkova EA, Ulasov IV, Bader SD, Rajh T, Lesniak MS, et al. Biofunctionalized magnetic-vortex microdiscs for targeted cancer-cell destruction. Nat Mater 2010;9:165–71. https://doi.org/10.1038/nmat2591.